Self-Consistent Anisotropic Kinetic Effects of Photoelectrons on the Polar Wind

by

Wing Yee Sunny Tam

Submitted to the Department of Physics
in partial fulfillment of the requirements for the degree of

Doctor of Philosophy in Physics

at the

MASSACHUSETTS INSTITUTE OF TECHNOLOGY

February 1996

Author .....
Department of Physics
February 1, 1996

Certified by .....
Tom T. S. Chang
Director, Center for Theoretical Geo/Cosmo Plasma Physics
Thesis Supervisor

Accepted by .....
George F. Koster
Chairman, Graduate Committee
Department of Physics

Self-Consistent Anisotropic Kinetic Effects of Photoelectrons on the Polar Wind

by

Wing Yee Sunny Tam

Submitted to the Department of Physics
on February 1, 1996, in partial fulfillment of the
requirements for the degree of
Doctor of Philosophy in Physics

Abstract

Experimental evidence in the polar region (field-aligned electron heat fluxes in the photoelectron energy range and day-night asymmetries in ion outflow velocities) indicates that photoelectrons may affect polar wind dynamics.

Such non-thermal fluxes can be explained by a mechanism relying on the divergent geomagnetic field and the energy dependence of Coulomb collisional cross-sections. The description of this mechanism requires a global kinetic approach. Preliminary results of a kinetic test-particle simulation of this mechanism agreed well with measured suprathermal fluxes. However, the effects of these fluxes on the polar wind itself would require a self-consistent description.

In this thesis, we introduce a self-consistent hybrid approach, in which the thermal electron features of the polar wind are described by fluid calculations, while the suprathermal electron features, as well as H^+ and O^+ ions are described using a kinetic model in a global environment. Coulomb collisions among species are taken into account, and the ambipolar electric field is deduced self-consistently. This approach therefore retains the expediency of fluid theory while extending its applicability by including important kinetic effects. The model itself represents a breakthrough in polar wind research, in that it is the first to incorporate the global kinetic collisional physics of photoelectrons into a self-consistent description. The model is also the first to generate a global steady-state polar wind solution that varies continuously from a subsonic collisional regime to a supersonic collisionless regime.

Results generated from the model reveal the importance of the kinetic effects which then lead to the intrinsic complexity of the polar wind dynamics. In general, the impact of the electric field on various polar wind outflow properties is very apparent. In the simplest case considered, the photoelectron energy flux enhances the electric field, thereby increasing the ion outflow velocities. Photoelectrons, therefore, can significantly affect the polar wind dynamics through their impact on the self-consistent electric field.

Our self-consistent treatment of kinetic physics is quite general. Thus, our model is readily applicable to other plasma outflows. These possible extensions are discussed,

and a study of the solar wind is given to illustrate the model's versatility.

Thesis Supervisor: Tom T. S. Chang
Title: Director, Center for Theoretical Geo/Cosmo Plasma Physics

Acknowledgments

I would like to express my deepest gratitude to Tom Chang, my thesis supervisor, for his precious advice, research guidance, and financial assistance over the years. I would specially like to thank Fareed Yasseen for initiating me on the subject of the polar wind, and for his careful reading of the manuscript.

I have enjoyed the interactions that I have had with Jay Johnson, John Retterer, and the personnel and visiting scientists at Center for Theoretical Geo/Cosmo Plasma Physics. I would also like to express my appreciation to Andrew Yau, Takumi Abe, and Supriya Ganguli for their discussions on the polar wind.

I am also thankful to Geoff Crew and Steve Jones for letting me share their Sparc 10 workstations.

I would like to express my deepest gratitude to my parents and, especially, my grandmother for their love and encouragement that have motivated me to reach for this milestone.

This work is supported by NASA Grants NAG5-225 and NAGW-1532, AFOSR Grant F49620-93-1-0287, and Phillips Laboratory Contract F19628-91-K-0043.

Contents

List of Figures

List of Tables

Chapter 1

Introduction

Plasma flows along magnetic field lines are a very common occurrence in space plasmas; they are also found in certain types of laboratory magnetic confinement devices. Examples include galactic jets and stellar winds, the solar wind in particular, and magnetospheric outflows originating from the polar regions of planetary ionospheres, or polar winds.

The existence of an outflow of plasma along the open magnetic field lines emanating from the polar region of the ionosphere was first proposed by *Axford* [1968] and *Banks and Holzer* [1968]. This outflow was termed "polar wind" in analogy with the solar wind, which had been recently observed [*Parker*, 1958]. These early studies included the ambipolar electric field among the mechanisms governing the plasma outflow. This electric field arises due to the anisotropy of the particle distributions in an inhomogeneous magnetic field. Because the polar cap, in general, is a relatively quiescent region, the ambipolar effect is a major contribution to the electric field in the "classical" polar wind, the steady-state, quasi-neutral, current-free outflow of plasma.

The ambipolar field itself is determined self-consistently by the background plasma. It is therefore influenced by other mechanisms that need to be included in the dynamics of the particles. For example, the geomagnetic field, which decreases with altitude, gives rise to the mirror force that changes the particles' pitch angles. Coulomb interactions among all the species lead to energy exchange and pitch angle

diffusion. These effects are essential to the dynamics of the particles, and therefore, can affect the polar wind electric field. Recent experimental evidence has shown that another effect — photoelectron populations generated in the sunlit ionosphere — can alter the polar wind significantly. In this study, we have developed a new model that enables one to determine the ambipolar electric field self-consistently, taking the above effects (including the photoelectrons) into account. This model successfully describes the recent observations, and demonstrates that the photoelectrons influence the polar wind by means of their impact on the ambipolar electric field.

1.1 Motivation: Evidence of Photoelectrons and of Their Impact on the Polar Wind

1.1.1 Photoelectron Signatures in the Polar Wind

Our study is motivated by increasingly convincing experimental evidence that photoelectrons play a significant role in the dynamics of the polar wind. Early polar cap measurements obtained by the ISIS-1 satellite showed evidence of "anomalous" field-aligned photoelectron fluxes in both upward and downward directions, where the downgoing (return) fluxes were considerably smaller than the outgoing fluxes above a certain energy [*Winningham and Heikkila*, 1974]. Such non-thermal features were confirmed by the DE-1 and -2 satellites [*Winningham and Gurgiolo*, 1982], whose measured electron distributions are shown in Fig. 1-1: outgoing field-aligned electron fluxes in the photoelectron energy range were observed by the HAPI (High Altitude Plasma Instrument) on DE-1 and the LAPI (Low Altitude Plasma Instrument) on DE-2; evidence of downstreaming electron fluxes was also found in the low-altitude distribution measured by the LAPI. These fluxes are considered anomalous because their existence cannot be related to the idea of thermal conductivity and temperature gradient in classical fluid theories. Similar to the ISIS-1 measurements, the return fluxes observed by DE-2 were comparable to the outgoing fluxes below some truncation energy, but considerably smaller above that. As suggested by *Winningham and*

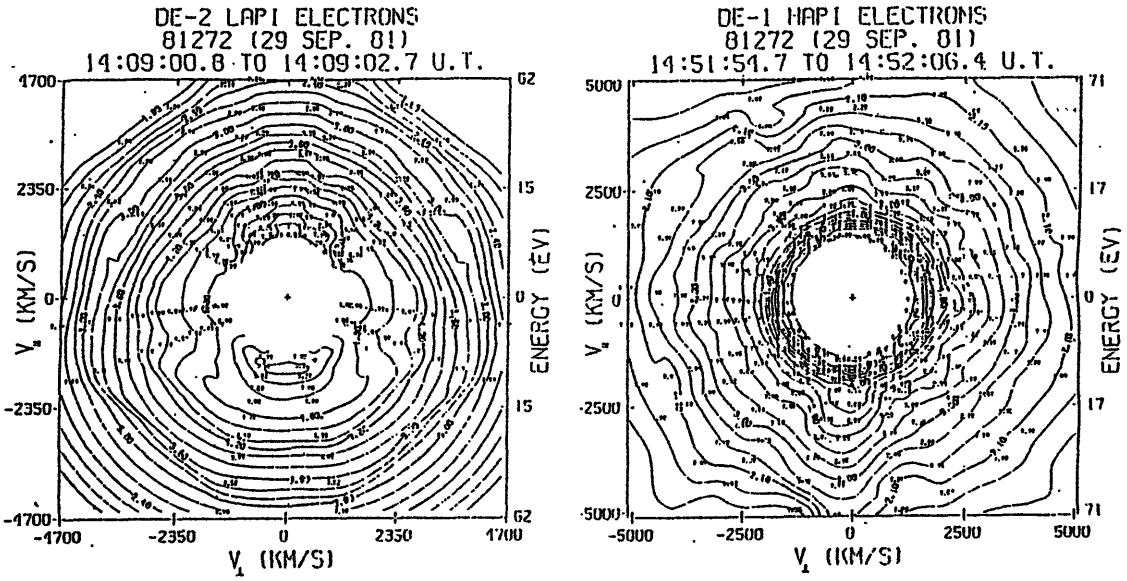

Figure 1-1: Electron distributions measured by the DE-1 (right) and DE-2 (left) satellites. These measurements were made at typical altitudes: $\geq$ 500 km for DE-2, and $\sim$ 4 earth radii for DE-1. By convention, $v_{||} > 0$ represents a downward velocity and $v_{||} < 0$ represents an upward velocity. Both satellites show evidence of outgoing field-aligned electron fluxes in the photoelectron energy range. Downstreaming electron fluxes are also present in the distribution measured by DE-2. The holes in the low-energy range of the measurements are due to the limitations of the instruments. Courtesy of Winningham and Gurgiolo.

Gurgiolo [1982], the existence of such downstreaming fluxes may be due to reflection of electrons by the ambipolar electric field along the geomagnetic field line above the satellite. The truncation energy, obtained by comparing the outgoing and the return electron fluxes, would thus provide an estimate for the potential drop due to the electric field. These authors observed that this truncation energy ranged from 5 to 60 eV, and thus were able to deduce the magnitude of the potential drop above the altitude of the satellite. Unfortunately, existing polar wind theories can only account for a much smaller potential drop [*Ganguli*, 1996, and references therein]. *Winningham and Gurgiolo* [1982] also pointed out that variation of the truncation energy was due to changes in the solar zenith angle at the production layer below the satellite. The solar zenith angle is related to the photoionization rate, which itself is related to the local ionospheric photoelectron density [*Jasperse*, 1981]. These observations therefore imply a relationship between the local photoelectron density below the satellite and the potential drop along the field line above it, and are consistent with the idea that the photoelectrons may significantly affect the ambipolar electric field.

1.1.2 Photoelectron Impact on Polar Wind Characteristics

While the observations discussed in the previous sub-section have implied that photoelectrons may contribute to the dynamics of the polar wind, more recent evidence indicates that the polar wind characteristics themselves are affected by the photoelectrons. *In-situ* measurements by the Akebono satellite revealed novel features in the polar wind — day-night asymmetries in the ion and electron features. The most dramatic are asymmetries in ion outflow velocities [*Abe et al.*, 1993b]: Satellite data between 5000 and 9000 km altitude indicate remarkably higher outflow velocities for the major ion species, H^+ and O^+, in the sunlit region than on the nightside. For example, H^+ velocity (u_h) was found to be about 12 km/s on the dayside, but only about 5 km/s on the nightside. Similarly, O^+ velocity (u_o) in the sunlit region ($\sim$ 7 km/s) is about twice that in the midnight sector ($\sim$ 3 km/s). A day-night asymmetry is also observed in the electron behavior. Electrons are distinguished according to their velocities along the geomagnetic field line. On the dayside, it was found that the

	Day	Night
u_h	12 – 13 km/s	4 – 5 km/s
u_o	6 – 7 km/s	2 – 3 km/s
$T_{e,up}/T_{e,down}$	1.5 – 2	≈ 1

Table 1.1: A summary of the polar wind day-night asymmetries observed by the Akebono satellite. The average ion outflow velocities were measured between 5000 and 9000 km altitude, and the electron temperature ratios were obtained at about 1700 km altitude.

temperature of the upstreaming population is greater than that of downstreaming population, *i.e.*, $T_{e,up} > T_{e,down}$, indicative of an upwardly directed heat flux [*Yau et al.*, 1995]. On the nightside, in contrast, no such up-down anisotropy is observed [*Abe et al.*, 1996]. The observed polar wind day-night asymmetries are summarized in Table 1.1. Besides the day-night asymmetries, Akebono measurements between 5000 and 9000 km altitude have also revealed other sometimes unexpected ion transport properties in the polar region [*Abe et al.*, 1993b]. For example, O^+ was most often found to be dominant over H^+ as the major ion species, contrary to the traditional belief that very few O^+ ions are able to overcome the gravitational force and escape to such high altitudes due to their heavier mass. The measured outflow velocities for both H^+ and O^+ ions in general increase monotonically with altitude, and the flows for both species are supersonic at high altitudes. In fact, the measured O^+ outflow velocities (see above) are much larger than the values expected by classical polar wind models [e.g. *Schunk and Watkins*, 1981, 1982; *Blelly and Schunk*, 1993]. Akebono data also seem to indicate an absence of downwardly moving ions between 5000 and 9000 km altitude. All these ion outflow characteristics, particularly the enhanced ion outflow velocities and the lack of downstreaming ions, suggest a higher ambipolar electric field than that predicted by classical polar wind models [*Ganguli*, 1996, and references therein], and are consistent with the values of the field-aligned potential drop deduced by *Winningham and Gurgiolo* [1982] based on the DE-2 measurements.

Because of the marked day-night asymmetries observed in several characteristics of the polar wind, and the fact that photoelectrons occur primarily in the sunlit ionosphere, they are *the* natural candidate to account for the day-night asymmetries.

Indeed, collisionless kinetic calculations by *Lemaire* [1972] showed that escaping photoelectrons may enhance the electric field and increase the ion outflow velocities in the polar wind. Photoelectrons, therefore, may provide a possible explanation for the observations of both sets of satellites — the magnitude of the ambipolar electric field deduced from DE-2 measurements, and the day-night asymmetries and enhanced ion outflow velocities observed by the Akebono satellite. Because Coulomb collisions may also influence the dynamics of photoelectrons, for example, by transferring their energy to other particle components in the polar wind, and thereby reducing the escaping photoelectron flux, collisional effects should also be taken into account in determining the impact of photoelectrons on the electric field. Our goal, therefore, is to address these observations by incorporating the complete photoelectron physics into a self-consistent, global description of the classical polar wind.

1.2 Traditional Approaches in Polar Wind Modeling

Let us begin by stating some criteria that will enable us to define the problem more precisely. First, we will consider the polar wind only at altitudes above 500 km (which corresponds roughly to the polar orbits of DE-2). At such altitudes, neutral densities are low enough to justify neglecting "chemical" reactions such as photoionization, recombination, *etc.* Second, the magnitude of the geomagnetic field is such that the gyration period and Larmor radius, for all particle species, are much smaller than any relevant time scale or scale length. We can therefore use the guiding center approximation. Third, the gradients of the geomagnetic field are such that only transport *along* the geomagnetic field line is important. The time-dependent distribution function $f(t, s, v_{\|}, v_{\perp})$ for a given particle species is therefore governed by the following collisional gyrokinetic equation:

$$\left[\frac{\partial}{\partial t} + v_{\|}\frac{\partial}{\partial s} - \left(g - \frac{q_c}{m}E_{\|}\right)\frac{\partial}{\partial v_{\|}} - {v_{\perp}}^2\frac{B'}{2B}\left(\frac{\partial}{\partial v_{\|}} - \frac{v_{\|}}{v_{\perp}}\frac{\partial}{\partial v_{\perp}}\right)\right] f = \frac{\delta f}{\delta t} = Cf, \quad (1.1)$$

where s is the distance along the magnetic field line B, q_c and m are the algebraic electric charge and mass of the species respectively, $E_{||}$ is the field-aligned electric field, g is the gravitational acceleration, $B' \equiv dB/ds$, $\delta f/\delta t$ represents the rate of change of the distribution function due to collisions, and C is a collisional operator for Coulomb interaction, which is the dominant type of collision above 300 km altitude. Equation (1.1) includes the major forces a particle experiences as it travels along the geomagnetic field line: gravitational force, field-aligned electric force, mirror force, and forces that are due to Coulomb collisions.

Obviously, solutions based on Eq. (1.1), even with additional simplifications (*i.e.*, a steady-state, quasi-neutral, current-free outflow of electrons and O^+ and H^+ ions — conditions satisfied by the "classical" polar wind), are difficult to obtain. Further approximations thus seem necessary. Traditionally, there have been two schools of thought in polar wind modeling — moment equations [*Banks and Holzer*, 1968; *Schunk*, 1977] and collisionless kinetic calculations [*Lemaire*, 1972] — each based on a different type of approximation to the kinetic, collisional approach embodied in Eq. (1.1).

1.2.1 Collisionless Kinetic Approach

Formulation

In *collisionless* kinetic calculations, one neglects the Coulomb collisional term in Eq. (1.1), leading to the well-known Vlasov equation. In the steady-state, the solution to the resulting collisionless equation is a function of the constants of motion, which are determined by the boundary conditions. For example, let $\mathbf{v}$ and $\mathbf{v_0}$ denote the velocity of a particle along the same trajectory at geocentric distances s and s_0 respectively. The solution is then given by

$$f(s, v_{||}, v_{\perp}) = f(s_0, v_{||0}, v_{\perp 0}), \tag{1.2}$$

The velocities are related through the constants of motion:
the total energy

$$\mathcal{E} = \frac{1}{2}m({v_\parallel}^2+{v_\perp}^2)+q_c\Phi_E(s)+m\Phi_G(s) = \frac{1}{2}m({v_{\parallel 0}}^2+{v_{\perp 0}}^2)+q_c\Phi_E(s_0)+m\Phi_G(s_0) \quad (1.3)$$

and the magnetic moment

$$\mu = \frac{1}{2}m{v_\perp}^2/B = \frac{1}{2}m{v_{\perp 0}}^2/B_0 \quad (1.4)$$

where B and B_0 are the magnetic field at s and s_0 respectively, Φ_E is the electric potential, related to the field-aligned electric field by $E_\parallel = -d\Phi_E/ds$, and $\Phi_G(s) = -G\mathcal{M}/s$ is the gravitational potential, with G and $\mathcal{M}$ being the gravitational constant and the mass of the earth respectively. The resulting distribution function (1.2) for each species is a function of $\Phi_E(s)$. Expressions for the density $n(s)$ and velocity $u(s)$ of the species are then given by

$$n(s) = \int d\mathbf{v}\, f(s, v_\parallel, v_\perp), \quad (1.5)$$

and

$$u(s) = \frac{1}{n(s)}\int d\mathbf{v}\, v_\parallel\, f(s, v_\parallel, v_\perp), \quad (1.6)$$

which also depend on $\Phi_E(s)$. To determine the electric potential, the local quasi-neutrality and current-free flow conditions can be used. Note that the escape fluxes $n(s)\,u(s)$ are inversely proportional to the local cross-sectional area of the flux tube, or in other words, proportional to the local magnetic field (see Eq. (2.1)). The zero-current condition needs to be imposed at one altitude only, such as s_0, and it will be maintained due to the property of the escape fluxes.

Drawbacks of the Collisionless Kinetic Approach

The collisionless kinetic approach, of course, is only valid at high altitudes where the plasma is collisionless. One should bear in mind, however, that the cumulative effect

of even weak Coulomb collisions may significantly affect the distribution function as the plasma flows over large distances. Upstream of the polar wind, the Coulomb collisional effect is definitely non-negligible. In order to take this effect into account, some investigators thus resort to the moment approach.

1.2.2 Moment Approach

Formulation

Moment-based models describe the particle transport using a few variables of the species, such as density, velocity, temperature and heat fluxes. The equations that describe these variables are obtained by taking velocity moments of Eq. (1.1). Due to the convective term $v_{\parallel} \partial/\partial s$ in Eq. (1.1), each of these equations contains a velocity moment term of the next higher order. Therefore, an approximation needs to be made in order to close the system of equations. Depending on how the closure assumption is made, moment-based models can be divided into two different classes — hydrodynamic and generalized transport. In a hydrodynamic model, the system, whose variables are described by the "standard" transport equations — the continuity, momentum, energy equations *etc.* — is closed by imposition of a relationship between the variables [*Holzer et al.*, 1971; *Schunk and Watkins*, 1979]. The generalized transport approach, on the other hand, is based on the formulation proposed by *Grad* [1949]. In this formulation, the distribution function is represented by an infinite series of the Hermite polynomials, which span a complete set in functional space. Closure of a generalized transport system relies on truncation of the series. By matching with the "standard" transport equations, coefficients for the terms in the truncated series are determined, giving rise to an assumed velocity dependence for the distribution function. Depending on where the series is truncated, the system may consist of a different number of moments. Existing models that have been discussed in the literature consist of five, eight, ten, thirteen, sixteen, and even twenty moments [*Schunk*, 1977; *Demars and Schunk*, 1979; *Barakat and Schunk*, 1982; *Schunk and Watkins*, 1979]. As an example, the system of sixteen-moment equations, which

we will refer to later in this thesis, imposes the following velocity dependence on the distribution function [*Barakat and Schunk*, 1982]:

$$f = f_b\,[1 + \Psi], \tag{1.7}$$

where

$$f_b = n\left(\frac{m^{3/2}}{(2\pi)^{3/2}T_\perp\sqrt{T_\parallel}}\right)\exp\left[-\frac{m(\mathbf{v}-\mathbf{u})_\perp{}^2}{2T_\perp} - \frac{m(\mathbf{v}-\mathbf{u})_\parallel{}^2}{2T_\parallel}\right] \tag{1.8}$$

is the zeroth-order bi-Maxwellian distribution function, and n, $\mathbf{u}$, $T_\parallel$, $T_\perp$ are parameters that are interpreted as the density, velocity, parallel and perpendicular temperatures of the species respectively. The distribution function f is assumed to be the zeroth-order bi-Maxwellian distribution, slightly modified by the term Ψ (see the Appendix for definitions), which contains parameters that are related to the heat fluxes in addition to those above. Because all velocity moments higher than the heat flux are absent in the assumption (1.7), closure of the system is achieved when no new variable is introduced in the heat flux equations. Notice that because of the gyrotropic nature of polar wind transport, the sixteen-moment system reduces to only six parameters: n, u (the field-aligned component of $\mathbf{u}$), $T_\parallel$, $T_\perp$, $q_\parallel$ and $q_\perp$. (The last two parameters are interpreted as the heat fluxes of parallel and perpendicular energies per particle.) The interpretation of these parameters is dictated by the fact that they correspond to the definitions of the following physical quantities:

$$n = \int d\mathbf{v}\, f, \tag{1.9}$$

$$u = \frac{1}{n}\int d\mathbf{v}\, v_\parallel\, f, \tag{1.10}$$

$$T_\parallel = \frac{1}{n}\int d\mathbf{v}\, m\,(v_\parallel - u)^2\, f, \tag{1.11}$$

$$T_\perp = \frac{1}{n}\int d\mathbf{v}\, \frac{1}{2}\, m\, v_\perp{}^2\, f, \tag{1.12}$$

$$q_\parallel = \frac{1}{n}\int d\mathbf{v}\, (v_\parallel - u)\, m\,(v_\parallel - u)^2\, f, \tag{1.13}$$

$$q_\perp = \frac{1}{n}\int d\mathbf{v}\, (v_\parallel - u)\, \frac{1}{2}\, m\, v_\perp{}^2\, f. \tag{1.14}$$

This correspondence can be verified by direct substitution of Eq. (1.7) into the definitions above. The temperatures and heat fluxes are sometimes combined into single quantities: the average temperature T, and the total heat flux per particle q, defined by

$$T = \frac{1}{3}T_{\|} + \frac{2}{3}T_{\perp}\,, \tag{1.15}$$

$$q = \frac{1}{2}q_{\|} + q_{\perp}\,. \tag{1.16}$$

Equations that describe the transport of these physical quantities are obtained by substituting Eq. (1.7) into Eq. (1.1) and taking velocity moments. For example, the zeroth order gives the continuity equation:

$$\frac{\partial n}{\partial t} + B\frac{\partial}{\partial s}\left(\frac{nu}{B}\right) = 0. \tag{1.17}$$

Higher orders in velocity moment result in:
the momentum equation (1st order)

$$\frac{\partial u}{\partial t} + u\frac{\partial u}{\partial s} + \frac{1}{nm}\frac{\partial (nT_{\|})}{\partial s} + \frac{GM}{s^2} - \frac{eE_{\|}}{m} - \frac{B'}{B}\left(\frac{T_{\|}-T_{\perp}}{m}\right) = \frac{\delta u}{\delta t}, \tag{1.18}$$

the parallel and perpendicular energy equations (2nd order)

$$\frac{\partial T_{\|}}{\partial t} + u\frac{\partial T_{\|}}{\partial s} + \frac{2}{n}\frac{\partial (nq_{\|})}{\partial s} - \frac{2B'}{B}(q_{\|}-q_{\perp}) + 2T_{\|}\frac{\partial u}{\partial s} = \frac{\delta T_{\|}}{\delta t}, \tag{1.19}$$

$$\frac{\partial T_{\perp}}{\partial t} + u\frac{\partial T_{\perp}}{\partial s} + \frac{1}{n}\frac{\partial (nq_{\perp})}{\partial s} - \frac{B'}{B}(2q_{\perp}+uT_{\perp}) = \frac{\delta T_{\perp}}{\delta t}, \tag{1.20}$$

and the heat flux equations for parallel and perpendicular energies (3rd order)

$$\frac{\partial q_{\|}}{\partial t} + u\frac{\partial q_{\|}}{\partial s} + 3q_{\|}\frac{\partial u}{\partial s} + \frac{3T_{\|}}{2m}\frac{\partial T_{\|}}{\partial s} = \frac{\delta q_{\|}}{\delta t}, \tag{1.21}$$

$$\frac{\partial q_{\perp}}{\partial t} + u\frac{\partial q_{\perp}}{\partial s} + q_{\perp}\frac{\partial u}{\partial s} + \frac{T_{\|}}{m}\frac{\partial T_{\perp}}{\partial s} - \frac{B'}{B}(uq_{\perp} + \frac{T_{\perp}}{m}(T_{\|}-T_{\perp})) = \frac{\delta q_{\perp}}{\delta t}, \tag{1.22}$$

where terms with $\delta/\delta t$, whose expressions can be found in the Appendix, represent changes of the moments due to collisional effects. In general, the collisional terms consist of separate components, each arising from collisions with a different particle species. The collisional effects on one species due to another are characterized by a velocity-averaged collisional frequency, which depends on the density, velocity and temperature moments of both species.

Other generalized transport models are based on a similar idea: the closure assumption approximates the distribution function by a slight but usually sophisticated modification of the Maxwellian or bi-Maxwellian distribution. Consequently, like a hydrodynamic model, these models consist of systems of moment equations for all the species. When applied to the classical polar wind, the steady-state moment equations for all the species are coupled by the quasi-neutrality and current-free flow conditions. A variety of these moment-based models has been applied to the classical polar wind to take into account collisional effects [*Banks and Holzer*, 1968; *Raitt et al.*, 1975, 1977; *Schunk and Watkins*, 1981, 1982] and even anisotropies [*Ganguli et al.*, 1987; *Demars and Schunk*, 1989; *Blelly and Schunk*, 1993].

Drawbacks of the Steady-State Moment Models

Because of the complexity and non-linear nature of the system of moment equations, analytic solutions are hard to achieve. Therefore, moment-based models are generally solved numerically. Because of the intrinsically stiff nature of these systems of moment equations (due essentially to the high mass ratios), even numerical solutions are not straightforward to obtain. In addition, these systems exhibit a number of singularities that arise from the truncation or the assumption used to close the system [*Yasseen and Retterer*, 1991]. The presence of these critical points has been known to lead to results contrary to the kinetic representation in the modeling of laboratory plasmas, such as describing tokamak equilibria with flow [*Bondeson and Iacono*, 1989, and references therein]. In the polar wind application, for example, the steady-state sixteen-moment model exhibits singularities near the ion sonic points, *i.e.*, the point at which the ion's thermal speed corresponds to its flow velocity (due to the current-free condition,

the flow velocities are much lower than the electron thermal velocities), and cannot provide transonic solutions easily. However, such transonic solutions are required for the appropriate description of the polar wind because observations indicate that both H^+ and O^+ outflows are supersonic at high altitudes [*Abe et al.*, 1993b]. In order to circumvent this difficulty, some investigators seek the steady-state solution by solving a time-dependent problem until a steady state is reached [*Blelly and Schunk*, 1993].

1.2.3 Transition Region

Implicit in the two complementary approaches outlined above is the assumption of the existence of a transition region separating a low-altitude collisional region where the flow is subsonic and a high-altitude collisionless region where the flow is supersonic. The simplest way to combine these two approaches is to introduce the concept of a baropause, the altitude at which the average collisional mean free path corresponds to the scale length of the outflow. The moment equations are then solved from a low-altitude boundary condition up to the baropause. The resulting moments at the baropause thus provide the boundary conditions for the collisionless kinetic calculations that will be applied to higher altitudes [*Barakat and Schunk*, 1983, 1984].

However, generalized transport models suffer from an intrinsic limitation that is incompatible with the inherent nature of Coulomb collisions. As discussed earlier, generalized transport models assume that the distribution functions are close to local thermodynamic equilibrium, thus describing the collisions using a velocity-averaged collisional frequency ν which depends on the local densities, velocities and temperatures of the plasma components. In other words, ν reflects the local properties of the plasma. Consider now a particle (or a group of particles) with a characteristic velocity V traversing a local neighborhood, whose size, L, is the smallest characteristic gradient scale length of the background, *i.e.*

$$L = \min\left(\left|\frac{1}{\alpha}\frac{d\alpha}{ds}\right|^{-1}\right), \tag{1.23}$$

where α represents the background density, velocity, temperature and the magnetic

field. The particles' transit time (*i.e.*, the time spent interacting with the local neighborhood) is $\sim L/V$. For these particles to "thermalize" *i.e.* to become representative of the local background properties, this transit time needs to be much greater than the local relaxation time, $L/V \gg \nu^{-1}$, or

$$\lambda \ll L, \tag{1.24}$$

where λ is the collisional mean free path of the particles. Condition (1.24) needs to be satisfied in order for collisions to be characterized by local collisional frequencies.

The Coulomb collisional cross-section for a charged particle is strongly dependent on its velocity relative to the background [*Ichimaru*, 1986]. In general, the higher the velocity, the smaller the cross-section and the collisional frequency. Energetic particles therefore have a longer collisional mean free path; its velocity dependence is approximately given by

$$\lambda \sim V^4. \tag{1.25}$$

Thus, the presence of energetic particles characterized by mean free paths longer than the scale length (such as the photoelectrons in the polar wind) can invalidate condition (1.24), limiting the applicability of generalized moment equations and, by the same token, invalidating the concept of a baropause. We can clearly see now why a generalized moment approach cannot be adequately used to include the collisional physics of the photoelectrons in a unified description of the polar wind. Instead, a global, kinetic approach is necessary. Here, by "global kinetic" we mean that we can resolve the mesoscale evolution of the particle distribution function resulting from microscale interactions.

1.3 Summary of Results

In this thesis, we shall introduce a self-consistent hybrid model that provides a global kinetic collisional description for the physics of polar wind photoelectrons. This model represents the first successful, fully self-consistent incorporation of such a photoelec-

tron description into the entire polar wind picture. Because of its global kinetic treatment of the ions, the model is also the first global polar wind calculation that generates a continuous solution which varies from a low-altitude collisional subsonic regime to a high-altitude collisionless supersonic regime. Results from the calculations represent an important step toward theory-observation closure as they are quantitatively consistent with experimental data in a variety of aspects.

Impact of photoelectrons on the polar wind dynamics is examined based on this self-consistent model. Specifically, we perform a comparative study by varying the relative photoelectron density in our boundary condition. Our results reveal the importance of kinetic effects and the intrinsic complexity of the polar wind dynamics, and demonstrate the necessity of a self-consistent description for the study. Indeed, some polar wind outflow properties are governed by *competing* effects, which are affected by these outflow properties themselves to different extents — only a self-consistent description can take all these inter-relations into account. Nevertheless, we find that increase in the relative photoelectron density enhances the self-consistent ambipolar electric field in the polar wind. The enhancement of the field often dictates the variation of other polar wind quantities, *e.g.* enhancement of the escaping ion flux, increase in the ion outflow velocities. The electric field enhancement due to increase in the relative photoelectron density also leads to variation in the ion densities. One would expect the ion density at high altitudes to increase with the electric field, because of the latter pushing more ions to escape. In fact, this is only half true. Acceleration of the *escaping* ions will deplete the density of the species due to particle conservation. Hence, the electric field itself may create competing effects on the ion densities. We find that in general, when the relative photoelectron density is sufficiently low, (and hence the electric field is also sufficiently low), an increase in the quantity (which causes the electric field also to increase) leads to an increase in the ion densities. But this is only true up to a certain limit. Beyond that, the density responds in an opposite way as the depletion effect takes over.

Coulomb collisions also play an important role in the polar wind dynamics. For example, the H^+-O^+ collisions give rise to a slowing-down effect on the H^+ ions.

This collisional effect competes against the acceleration by the electric field in governing the H^+ outflow velocity. Our results show that the relative importance of the slowing-down effect is related to the O^+ density, due to the density dependence of the collisional rates. When the relative photoelectron density is sufficiently low such that an increase in the quantity will cause the ion densities to increase (see above), the slowing-down effect on H^+ may be enhanced to a greater extent than the acceleration effect due to the electric field.

We also investigate the effects of other ionospheric quantities on the polar wind dynamics. Our results indicate that ionospheric quantities influence the polar wind mainly through their impact on the self-consistent electric field, which responds primarily to the ambipolar effect. Hence, for example, a larger electron flux (such as that associated with the photoelectrons) or a smaller ion flux in the ionospheric conditions will give rise to a larger self-consistent electric field. Other polar wind outflow properties are generally influenced most apparently by the electric field.

1.4 Structure of the Thesis

The aim of this study is to demonstrate that photoelectron dynamics in the classical polar wind can be responsible for the DE-1, 2 and Akebono observations — a potential drop of the order of 10 V, day-night asymmetries in ion outflow velocities, electron anisotropy and an upwardly directed electron heat flux. In Chapter 2, we will discuss the energy flux mechanism by which photoelectrons can enhance the ambipolar electric field, thereby increasing the ion outflow velocities, and present our preliminary results to support this idea. The calculations take into account the global kinetic collisional physics of photoelectrons in a background generated by the 16-moment model, and estimate the zeroth-order photoelectron effects on the background.

However, in order to study the overall photoelectron impact on the polar wind itself, shown by the Akebono observations, a self-consistent description is required. In Chapter 3, we will introduce a self-consistent hybrid model. The word "hybrid" indicates that the model consists of a fluid part for the thermal electrons and a

kinetic collisional part, and should be distinguished from other hybrid schemes where, *e.g.*, the electrons are treated as a massless neutralizing fluid. Specifically, in this model, photoelectrons (which are treated as test particles because of their low relative density) as well as all the ion species (H^+, O^+) are described by a global kinetic collisional approach, while thermal electron properties and the ambipolar electric field are determined by a fluid calculation.

In Chapter 4, we will show results of a polar wind parametric study based on the self-consistent hybrid model. In particular, we will discuss the effects due to variation of the relative photoelectron density. The influence of other relevant parameters, such as the ionospheric ion temperatures, will also be discussed.

The self-consistent hybrid technique is not only a very powerful tool for the study of steady-state problems. It is also quite versatile. Its modular treatment of the kinetic physics makes it easily applicable to steady-state plasma outflows in other magnetic geometries and subject to additional kinetic effects, such as quasi-linear wave-particle interactions. In Chapter 5, we provide a brief comparison between the solar and polar winds and, to illustrate the versatility of our model, apply it to the low-speed solar wind. Finally, in the Conclusion, we provide a quick overview of the results obtained in this thesis, and discuss possible extensions or refinements of our model.

Chapter 2

Photoelectrons, Energy Fluxes and Electric Field

2.1 Photoelectrons and Formation of Anomalous Energy Fluxes

The impact of photoelectrons on the polar wind was postulated in the early literature. *Axford* [1968] proposed that the charge separation enhanced by escaping polar wind photoelectron flux might increase the ambipolar electric field which, in turn, might accelerate the ions. As we have pointed out in Section 1.2.3, these photoelectrons require a global kinetic collisional description.

The global kinetic collisional physics of suprathermal electrons in a steady-state space plasma outflow was first considered by *Scudder and Olbert* [1979] in their study of solar wind halo electrons. These authors related the anomalous field-aligned electron heat fluxes observed in the solar wind to the non-local nature of the electron distributions, and demonstrated the formation of such non-thermal features using a simplified collisional operator. They also suggested that these suprathermal electrons, through their anomalous contribution to the energy flux, may significantly increase the ambipolar electric field along the magnetic field lines, thereby "driving" the solar wind [*Olbert*, 1982].

Applying Scudder and Olbert's arguments to the classical polar wind, *Yasseen et al.* [1989] demonstrated a correlation between photoelectrons and the observed anomalous energy fluxes. They performed a global kinetic collisional test-particle simulation using a photoelectron distribution that is consistent with the observed data at low altitude, a background electron density profile based on a fluid simulation and an assumed power-law electric field consistent with the values deduced by *Winningham and Gurgiolo* [1982]. The results of their steady-state calculations indicated that photoelectrons not only can give rise to the anomalous field-aligned energy fluxes observed at high altitude, but also can be responsible for the downstreaming electron distribution observed in the low-altitude polar wind [*Winningham and Gurgiolo*, 1982].

The non-local nature of the anomalous electron energy fluxes in both the solar and polar winds can be understood in terms of the combined action of the divergent magnetic field and the velocity-dependent Coulomb collisional frequencies. Let us consider, for example, a steady-state, low-altitude Maxwellian particle distribution, and see how Coulomb interactions among the particles change the distribution at a higher altitude. Because the collisional mean free path of a particle increases with its velocity relative to the background plasma (see Eq. (1.25)), the smaller this velocity, the more collisions the particle experiences and, consequently, the greater the slowing-down as it moves along the magnetic field line. This velocity-dependent slowing-down amplifies the velocity differential within the species, allowing the divergent magnetic field to fold the distribution at high energies into a field-aligned tail. In the solar wind, the halo represents the energetic component of the electron distributions, shown to be associated with the observed anomalous energy flux [*Scudder and Olbert*, 1979]. In the polar wind, the photoelectrons are the energetic particle population that is responsible for the non-thermal features at high altitude [*Yasseen et al.*, 1989].

2.2 Energy Flux Mechanism

In a space plasma outflow, such as the polar wind, the energy fluxes of the particles are related to the field-aligned electric field. Their relationship in the high-altitude (collisionless) "classical" (steady-state) polar wind can be readily derived from Eq. (1.1). By taking its zeroth-order moment, and neglecting the time-derivative and collisional terms, one obtains the mass conservation of the species:

$$\frac{\partial}{\partial s}\left(\frac{nu}{B}\right) = 0. \tag{2.1}$$

Similarly, the second-order moment gives the relationship for energy conservation:

$$\frac{\partial}{\partial s}\left\{\frac{1}{B}\left[Q_w + nu\left(m\Phi_G + q_c\Phi_E\right)\right]\right\} = 0. \tag{2.2}$$

where $Q_w = \int d\mathbf{v}\frac{1}{2}mv^2 v_{||} f(s, v_{||}, v_\perp)$ is the energy flux of the species. Equation (2.2) must be satisfied by every particle species. It illustrates a direct relation between the particle energy flux and the electric potential. The equations for different species are coupled through the ambipolar electric potential terms and the two classical polar wind constraints — quasi-neutrality and current-free flow. However, one can show from the electron equation that in an outflowing plasma, a larger outward (or upward, in the case of the polar wind) electron energy flux generally leads to a larger electric potential drop.

As discussed in Section 2.1, photoelectrons carry a large amount of upward energy flux in the polar outflow. Their presence, primarily in the sunlit ionosphere, thus enhances the dayside ambipolar electric field, thereby increasing the ion outflow velocities on the dayside. Photoelectrons, with their associated energy fluxes, can therefore provide not only a mechanism for the enhanced ion outflow velocities observed by the Akebono satellite [*Abe et al.*, 1993a, 1993b], but also the explanation for the observed day-night asymmetric ion and electron features in the polar wind [*Abe et al.*, 1993b, 1996; *Yau et al.*, 1995].

Energetic suprathermal electrons in the polar wind or in other ionospheric/mag-

netospheric settings have been considered by various authors. For example, kinetic collisional calculations by *Khazanov et al.* [1993] have examined the role of photoelectrons on plasmaspheric refilling. Collisionless kinetic calculations by *Lemaire* [1972] have shown that escaping photoelectrons may increase the ion outflow velocities in the polar wind. Collisionless kinetic calculations by *Barakat and Schunk* [1984] and generalized semi-kinetic (GSK) calculations by *Ho et al.* [1992] have examined the impact of hot magnetospheric electrons, and concluded that such particles may also increase the ion outflow velocities.

We should add that other mechanism besides suprathermal electron effects may also be proposed as alternative explanations for the enhanced ion velocities. Parallel ion acceleration driven by $\mathbf{E} \times \mathbf{B}$ convection was considered by *Cladis* [1986], and shown to significantly energize O^+ ions escaping to the polar magnetosphere. This force can also be seen as a centrifugal force in the convecting frame of reference, and was included in this form in the time-dependent, GSK model developed by *Horwitz et al.* [1994]. These mechanisms, including the suprathermal electron effects, have recently been reviewed by *Ganguli* [1996].

2.3 Preliminary Calculations

2.3.1 Global Kinetic Collisional Test-Particle Model

The relationship among photoelectrons, their associated suprathermal heat flux and the ambipolar electric field as discussed in the previous sections has been demonstrated in our preliminary calculations [*Tam et al.*, 1995a], which treat the photoelectrons as a test, suprathermal population. At this point, the author would like to point out that the work in *Tam et al.* [1995a] is a very important stepping stone leading to the final results in this thesis, for two reasons. First, this model revealed important elements that needed to be included in the photoelectron physics in the polar wind. Second, the global kinetic collisional test-particle model on which these calculations were based provides the cornerstones of the self-consistent hybrid model,

which has allowed us to obtain the more comprehensive results presented later in this thesis.

Formulation

As in the collisionless kinetic approach, the global kinetic collisional test-particle model describes the dynamics of a particle species by its steady-state distribution function, but obviously, takes into account the Coulomb collisions. However, as suggested by the word "test-particle," the model assumes that the species has a low relative density compared to the background [*Yasseen et al.*, 1989; *Tam et al.*, 1995a]. This assumption allows the collisional operator to be simplified. For example, let us describe Coulomb collisions in Eq. (1.1) using a Fokker-Planck collisional operator [*Nicholson*, 1983]:

$$C_{FP} f_\alpha(t,s,\mathbf{v}) = \sum_\beta \left\{ -\frac{\partial}{\partial \mathbf{v}} \cdot (\mathbf{A}_{\alpha\beta} f_\alpha(t,s,\mathbf{v})) + \frac{1}{2}\frac{\partial^2}{\partial \mathbf{v}\partial \mathbf{v}} : (\mathbf{B}_{\alpha\beta} f_\alpha(t,s,\mathbf{v})) \right\}, \quad (2.3)$$

where the subscript α indicates the particle species whose Coulomb collisional interactions are described by (2.3), and β represents the background particle species, which may include species α itself, and the dynamic friction coefficient $\mathbf{A}_{\alpha\beta}$ and diffusion coefficient $\mathbf{B}_{\alpha\beta}$ are defined as

$$\mathbf{A}_{\alpha\beta} \equiv \frac{4\pi {q_{c\alpha}}^2 {q_{c\beta}}^2 \ln\Lambda^{\alpha/\beta}}{{m_\alpha}^2} \left(1 + \frac{m_\alpha}{m_\beta}\right) \frac{\partial}{\partial \mathbf{v}} \int d\mathbf{v}' \frac{f_\beta(t,s,\mathbf{v}')}{|\mathbf{v}-\mathbf{v}'|}, \quad (2.4)$$

$$\mathbf{B}_{\alpha\beta} \equiv \frac{4\pi {q_{c\alpha}}^2 {q_{c\beta}}^2 \ln\Lambda^{\alpha/\beta}}{{m_\alpha}^2} \frac{\partial^2}{\partial \mathbf{v}\partial \mathbf{v}} \int d\mathbf{v}' |\mathbf{v}-\mathbf{v}'| \, f_\beta(t,s,\mathbf{v}'), \quad (2.5)$$

where $\ln\Lambda^{\alpha/\beta}$ is the Coulomb logarithm for species α colliding with species β. Notice that due to Coulomb collisions among particles of species α ("self-collisions:" corresponding to the case $\beta = \alpha$), the collisional terms in the governing equation, Eq. (1.1) with collisional operator (2.3), is non-linear in f_α. However, because the collisional rates are proportional to the density of the background species, collisions among species α itself are negligible, provided that the species has a low relative density compared to other background species. This approximation, *i.e.* neglecting

self-collisions, allows us to linearize the collisional operator. If we further assume the background species to be described by drifting Maxwellian distributions, *i.e.*,

$$f_\beta(t,s,\mathbf{v}') \;=\; n_\beta\left(\frac{m_\beta}{2\pi T_\beta}\right)^{3/2}\exp\left[-\frac{m(\mathbf{v}-\mathbf{u}_\beta)^2}{2T_\beta}\right], \tag{2.6}$$

then the governing equation reduces to [*Book*, 1989]:

$$\frac{\partial f_\alpha}{\partial t}+v_\parallel\frac{\partial f_\alpha}{\partial s}-\left(g-\frac{q_{c\alpha}}{m_\alpha}E_\parallel\right)\frac{\partial f_\alpha}{\partial v_\parallel}-{v_\perp}^2\frac{B'}{2B}\left(\frac{\partial f_\alpha}{\partial v_\parallel}-\frac{v_\parallel}{v_\perp}\frac{\partial f_\alpha}{\partial v_\perp}\right) \;=\; \sum_{\beta\neq\alpha}\frac{\partial}{\partial\mathbf{v}}\cdot$$
$$\left\{\frac{m_\alpha}{m_\alpha+m_\beta}{\nu_s}^{\alpha/\beta}\mathbf{w}_\beta f_\alpha+\frac{1}{2}{\nu_\parallel}^{\alpha/\beta}\mathbf{w}_\beta\mathbf{w}_\beta\cdot\frac{\partial f_\alpha}{\partial\mathbf{v}}+\frac{1}{4}{\nu_\perp}^{\alpha/\beta}\left({w_\beta}^2\mathbf{I}-\mathbf{w}_\beta\mathbf{w}_\beta\right)\cdot\frac{\partial f_\alpha}{\partial\mathbf{v}}\right\}, \tag{2.7}$$

where $\mathbf{w}_\beta\equiv\mathbf{v}-\mathbf{u}_\beta$, and ${\nu_s}^{\alpha/\beta}$, ${\nu_\parallel}^{\alpha/\beta}$ and ${\nu_\perp}^{\alpha/\beta}$ are frequencies characterizing the slowing-down, and the parallel and perpendicular diffusion rates respectively, and are given by:

$${\nu_s}^{\alpha/\beta} \;\equiv\; \left(1+\frac{m_\alpha}{m_\beta}\right)\psi(x^{\alpha/\beta})\,{\nu_0}^{\alpha/\beta}, \tag{2.8}$$

$${\nu_\parallel}^{\alpha/\beta} \;\equiv\; \frac{\psi(x^{\alpha/\beta})}{x^{\alpha/\beta}}\,{\nu_0}^{\alpha/\beta}, \tag{2.9}$$

$${\nu_\perp}^{\alpha/\beta} \;\equiv\; 2\left[\left(1-\frac{1}{2x^{\alpha/\beta}}\right)\psi(x^{\alpha/\beta})+\psi'(x^{\alpha/\beta})\right]{\nu_0}^{\alpha/\beta}, \tag{2.10}$$

where

$${\nu_0}^{\alpha/\beta}=4\pi\,n_\beta\,{q_{c\alpha}}^2\,{q_{c\beta}}^2\,\ln\Lambda^{\alpha/\beta}/{m_\alpha}^2{w_\beta}^3, \tag{2.11}$$

$$x^{\alpha/\beta}={m_\beta}{w_\beta}^2/2kT_\beta,$$

$$\psi(x)=\frac{2}{\sqrt{\pi}}\int_0^x dt\sqrt{t}\;e^{-t},$$

$$\psi'(x)=\frac{d\psi}{dx}.$$

Given an initial test-particle distribution function, we may solve Eq. (2.7) for its time-evolution. In principle, the resulting distribution function $f_\alpha(t,s,\mathbf{v})$ should be temporally continuous; however, the solution can be obtained numerically by a finite difference scheme. The idea of this scheme is to obtain the time-dependence of the

distribution function by following the trajectories of its phase space elements as the temporal variable is incremented. Each increment, Δt, should be much smaller than any time scale found in Eq. (2.7). In particular, a necessary condition for the size of Δt is:

$$\Delta t \ll \min_{\beta} \left\{ \left(\nu_s{}^{\alpha/\beta}\right)^{-1}, \left(\nu_{\|}{}^{\alpha/\beta}\right)^{-1}, \left(\nu_{\perp}{}^{\alpha/\beta}\right)^{-1} \right\}. \tag{2.12}$$

Once an appropriate time step is chosen, the trajectories of the phase space elements of the distribution function can be obtained from the associated Langevin equations [see *Nicholson*, 1983, for example]:

$$\begin{aligned} t &\rightarrow t + \Delta t, \\ s &\rightarrow s + \Delta s, \\ \mathbf{v} &\rightarrow \mathbf{v} + \Delta \mathbf{v}. \end{aligned} \tag{2.13}$$

where the changes Δs and $\Delta \mathbf{v}$ associated with Eq. (2.7) are:

$$\Delta s = v_{\|} \Delta t, \tag{2.14}$$

and

$$\begin{aligned} \Delta \mathbf{v} = & \left(\frac{q_{c\alpha}}{m_\alpha} E_{\|} - g \right) (\Delta t) \hat{b} - \frac{B'}{2B} \left(\frac{v_\perp{}^2}{v_{\|}} \hat{b} - \mathbf{v}_\perp \right) (\Delta s) - \sum_{\beta \neq \alpha} \nu_s{}^{\alpha/\beta} \, \mathbf{w}_\beta \, (\Delta t) \\ & + \sum_{\beta \neq \alpha} \left\{ \sqrt{\frac{1}{2} \nu_\perp{}^{\alpha/\beta} (\Delta t)} \, w_\beta \, (\xi_{\beta 1} \hat{e}_1 + \xi_{\beta 2} \hat{e}_2) + \sqrt{\nu_{\|}{}^{\alpha/\beta} (\Delta t)} \, \mathbf{w}_\beta \, \xi_{\beta 3} \right\}, \end{aligned} \tag{2.15}$$

where $\hat{b}$ is the unit vector parallel to $\mathbf{B}$, $\hat{e_1}$ and $\hat{e_2}$ are two unit vectors that are orthogonal to each other, and to $\mathbf{w}_\beta$, and the ξ's represent random numbers generated from a Gaussian distribution such that for each ξ,

$$< \xi > = 0, \; < \xi^2 > = 1.$$

Note that all the physics described in Eq. (2.7) is translated into Eq. (2.13 - 2.15)

by the finite difference scheme. Gravitational acceleration and that due to the field-aligned ambipolar electric field lead to the first two terms in Eq. (2.15). The third and fourth terms reflect the mirror force arising from the non-uniform geomagnetic field. Effects of the Coulomb interaction are described by the remaining terms in the equation. For example, the term with ${\nu_s}^{\alpha/\beta}$ represents the dynamic friction between the particle and the background species, and is thus proportional in magnitude with but opposite in direction to their relative velocity. The effect of pitch angle diffusions, on the other hand, is carried by the last two terms, in which we distinguish between directions perpendicular and parallel to the relative velocity, due to the different diffusion rates.

Monte Carlo method

The finite difference scheme discussed in the previous subsection basically uses a series of discrete values in the temporal variable to represent a continuous spectrum. A similar approach can be applied to the phase space variables, s and $\mathbf{v}$; this Monte Carlo method is based on this idea [*Spitzer*, 1987]. To illustrate the concept behind this Monte Carlo technique, let us consider an initial value problem, Eq. (2.7) with a prescribed test-particle distribution function

$$f_\alpha(t_0, s, \mathbf{v}) \;=\; g(s, \mathbf{v}). \tag{2.16}$$

By using delta functions, we can express the initial condition in form of an integral over the phase space:

$$f_\alpha(t_0, s, \mathbf{v}) \;=\; \int ds' d\mathbf{v}' \delta(s' - s)\, \delta(\mathbf{v}' - \mathbf{v})\, g(s', \mathbf{v}'). \tag{2.17}$$

The basic idea of the Monte Carlo method is to represent the continuous phase space by a finite number (say N) of discrete elements. With this approximation, the integral

is transformed into a summation, and Eq. (2.17) becomes

$$f_\alpha(t_0, s, \mathbf{v}) \;=\; \sum_{i=1}^{N} \delta(s_i - s)\, \delta(\mathbf{v}_i - \mathbf{v})\, g(s_i, \mathbf{v}_i), \tag{2.18}$$

where $(s_i, \mathbf{v}_i)$ is the phase space coordinates of the i-th element. Now let us write

$$f_\alpha(t, s, \mathbf{v}) \;=\; \sum_{i=1}^{N} f_{\alpha i}(t, s, \mathbf{v}). \tag{2.19}$$

and impose the following initial conditions for $f_{\alpha i}$:

$$f_{\alpha i}(t_0, s, \mathbf{v}) \;=\; \delta(s_i - s)\, \delta(\mathbf{v}_i - \mathbf{v})\, g(s_i, \mathbf{v}_i). \tag{2.20}$$

Due to the linearity of Eq. (2.7) in f_α, it suffices to solve the equation for $f_{\alpha i}(t, s, \mathbf{v})$ with initial conditions (2.20) for $i = 1, \ldots, N$; the sum of the N solutions yields the solution for $f_\alpha(t, s, \mathbf{v})$.

Recall that Eq. (2.7) is equivalent to Eq. (2.13 - 2.15) as a result of the finite difference scheme. The concept of the Monte Carlo method is to solve for $f_{\alpha i}$ with these finite difference equations. This technique assigns a large number of "particles" to act the role of the singular initial conditions (2.20) in phase space. In other words, these "particles" form a finite but representative sample of phase space elements of the test-particle distribution function. Because of the singular nature of the "particles," the finite difference scheme can be readily applied to follow their trajectories, and, therefore, those of the phase space elements as time evolves. The overall distribution function, as Eq. (2.19) suggests, is obtained from an aggregation of the phase space elements.

The Monte Carlo method described above allows one to find the time-dependence of the distribution function. However, because the "classical" polar wind is a steady-state phenomenon, we are in fact more interested in the steady-state distribution function. To obtain such a distribution function, we may consider the initial condition as the distribution function of the source. Then, of course, in principle one may continuously introduce particles at the source as time goes on, and wait until the

overall distribution function comes to a steady state. This brute-force approach is inefficient.

However, there is an alternative, and more efficient, way to apply the Monte Carlo technique. This method was developed by *Retterer et al.* [1987], and applied to wave-particle interactions in the magnetosphere. The reasoning for this technique is the following. In a steady-state flow with a continuous source, let us consider what is meant by the phase space coordinates of a particle (labeled a) at some time t_2. Besides the obvious interpretation — where particle a sits in phase space at t_2 — the coordinates also indicate the phase space location at an earlier time t_1 of another particle that was generated from the source before particle a. By the same token, the phase space coordinates would be occupied at a later time t_3 by another particle generated after particle a. This argument leads to the conclusion that the complete phase space trajectories of all the particles generated from the source at the same instance is equivalent to the overall steady-state distribution. Therefore, it suffices to apply the Monte Carlo technique to only one set of particles that represent the source distribution function. Because it is usually the case that one is interested in the particles' dynamics only in a particular spatial range, one may cease to follow a particle once it exits the range.

To calculate the steady-state distribution function, observation points are set up along the simulation range. This situation is analogous to a spacecraft observation at the point where its orbit intersects the geomagnetic field line. Whenever a particle passes an observation point, the phase space element it represents is recorded, and will later be aggregated to obtained the total steady-state distribution function. The weight carried by the phase space element at different observation points is calculated consistently with Eq. (2.1), the steady-state continuity equation. When the steady-state distribution function is obtained, various velocity-moment profiles of the test-particle species, such as density, velocity and temperature, can be calculated by phase space averaging over the distribution function. Because the collisional impact on the test particles due to each background species is calculated (see Eq. (2.15)), this technique also enables us to find the energy and momentum transfers between the

test-particle species and each of the background species.

Initial Distribution and Background

To apply the Monte Carlo technique to photoelectrons in the polar wind, we must treat them as test particles and assign them to an initial distribution. Such a distribution in our calculations is based on measured photoelectron spectra [*Lee et al.*, 1980]. We associate the initial distribution with a modified Maxwellian distribution function:

$$f(\mathbf{v}) = \frac{n_0}{(2\pi)^{3/2}}\sqrt{\frac{m}{T_*}}\,\frac{e^{-mv^2/2T_*}}{v^2}, \tag{2.21}$$

where n_0 is the photoelectron density at the initial altitude, and to be determined later in the calculation, and T_* is a temperature parameter for the distribution function. A comparison between this distribution function and the Maxwellian distribution, both normalized to the same constant, is shown in Fig. 2-1. In our calculation, the suprathermal electrons are initially situated at 1500 km altitude, and represented by the upper-half of a truncated distribution function that is in the form of Eq. (2.21), with $T_* = 21.6$ eV, and energy ranging from 2 to 62 eV. This distribution is an empirical fit based on the photoelectron spectra measured by *Lee et al.* [1980]. The main difference in using an initial distribution in such a form, as compared to a Maxwellian distribution, is that more particles are now in the low energy range, giving a lower initial energy (and heat) flux for the suprathermal electrons. One thus would expect the associated electric field to be smaller than that in the case of a Maxwellian distribution.

In order for the global kinetic collisional test-particle model to be applicable to the polar wind, an electric field profile is required to simulate the ambipolar field, and density, velocity and temperature profiles of the background species must be imposed to determine the Coulomb collisional operator. For example, *Yasseen et al.* [1989] have used this model with a simplified background. This background consisted of an empirical fit of the electron density profile produced by a fluid simulation and an assumed power-law electric field whose overall potential drop was consistent

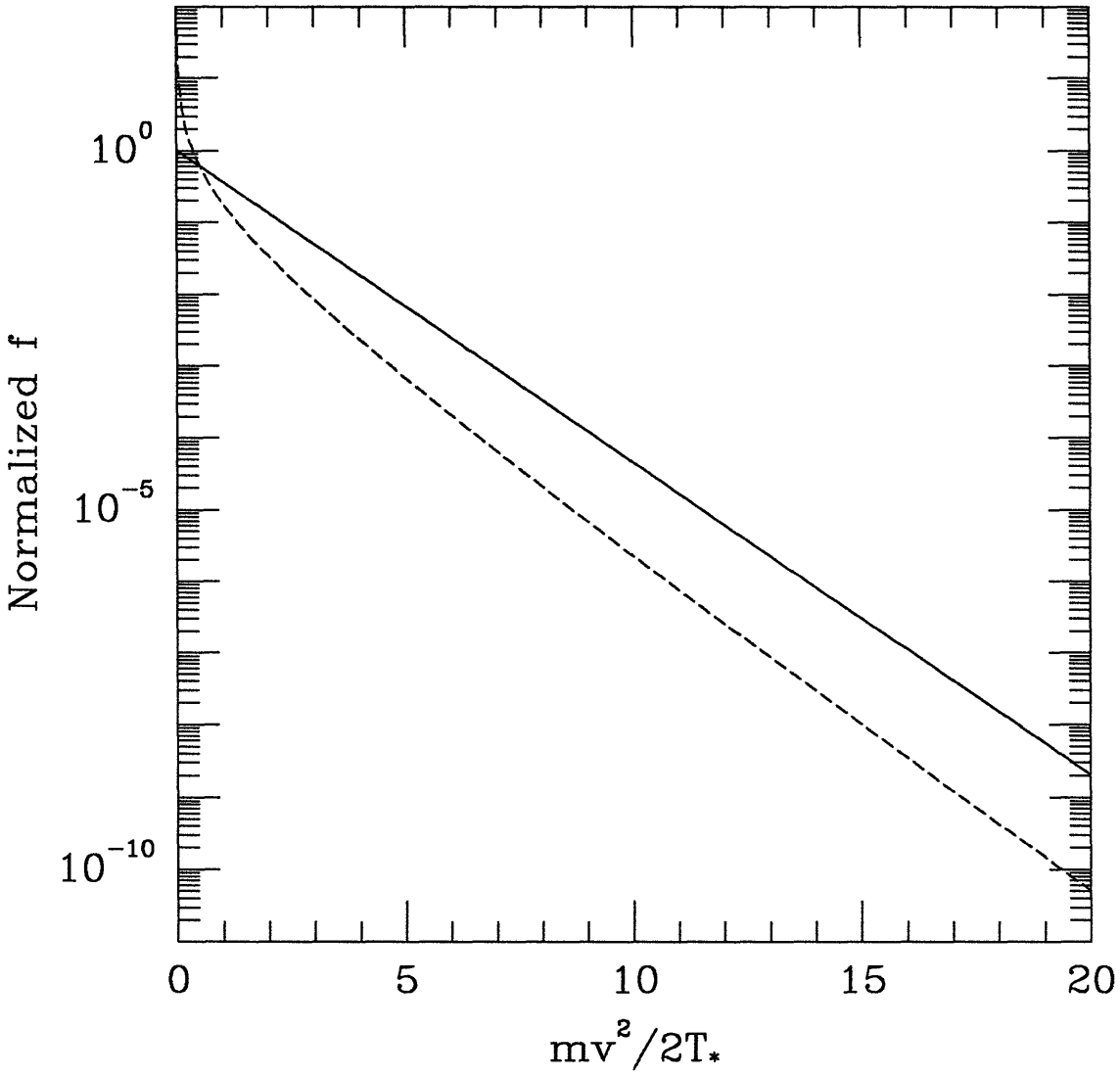

Figure 2-1: Comparison between the Maxwellian distribution function (solid) and the distribution function in Eq. (2.21) (dashed).

with the values deduced by *Winningham and Gurgiolo* [1982]. Background ions were ignored in their collisional operator for simplicity as Coulomb interaction between the test particles (suprathermal electrons) and the ions would not affect their results qualitatively.

However, in order to establish the significance of photoelectrons, we should be able to compare their suprathermal contributions to the polar transport with those due to the background thermal electrons. It is thus necessary to use a background in which the density, velocity and temperature profiles of the thermal species are consistent with the electric field. An ideal choice of background would be actual *in situ* experimental data collected by polar-orbiting satellites, *e.g.*, Akebono [*Abe et al.*, 1993a, 1993b; *Yau et al.*, 1995], DE-2 [*Winningham and Gurgiolo*, 1982], and ISIS-1,2 [*Winningham and Heikkila*, 1974; *Johnstone and Winningham*, 1982]. However, the available data are unfortunately not detailed enough for our purpose. *Tam et al.* [1995a] therefore used a polar wind background based on the solution of a steady-state sixteen-moment transport model (Eq. (1.17 – 1.22)). Such a moment-based background, generated by a code developed by S. Ganguli, allows comparison of the suprathermal with the thermal contributions to various transport quantities, including the heat fluxes. (For consistency, the boundary conditions used in *Ganguli et al.* [1987] are applied). The code calculates transport of H^+ and thermal electron species in a stationary background of O^+ ions, which are assumed to be bound by the terrestrial gravitational field because of their heavier mass. Figure 2-2(a) shows the polar wind background profiles of the electric field and the density of the species, obtained from the moment calculations. Note that the electric field only amounts to a potential drop of less than 1 V, which is much smaller than the value deduced by *Winningham and Gurgiolo* [1982]. Associated with these profiles in the solution are the H^+ and thermal electron velocities and temperatures, shown in Fig. 2-2(b) and (c).

The background used in *Tam et al.* [1995a] consists of the electric field profile, and the thermal electron profiles of density, velocity, and temperature, while, like the background in *Yasseen et al.* [1989], Coulomb collisions between the suprathermal

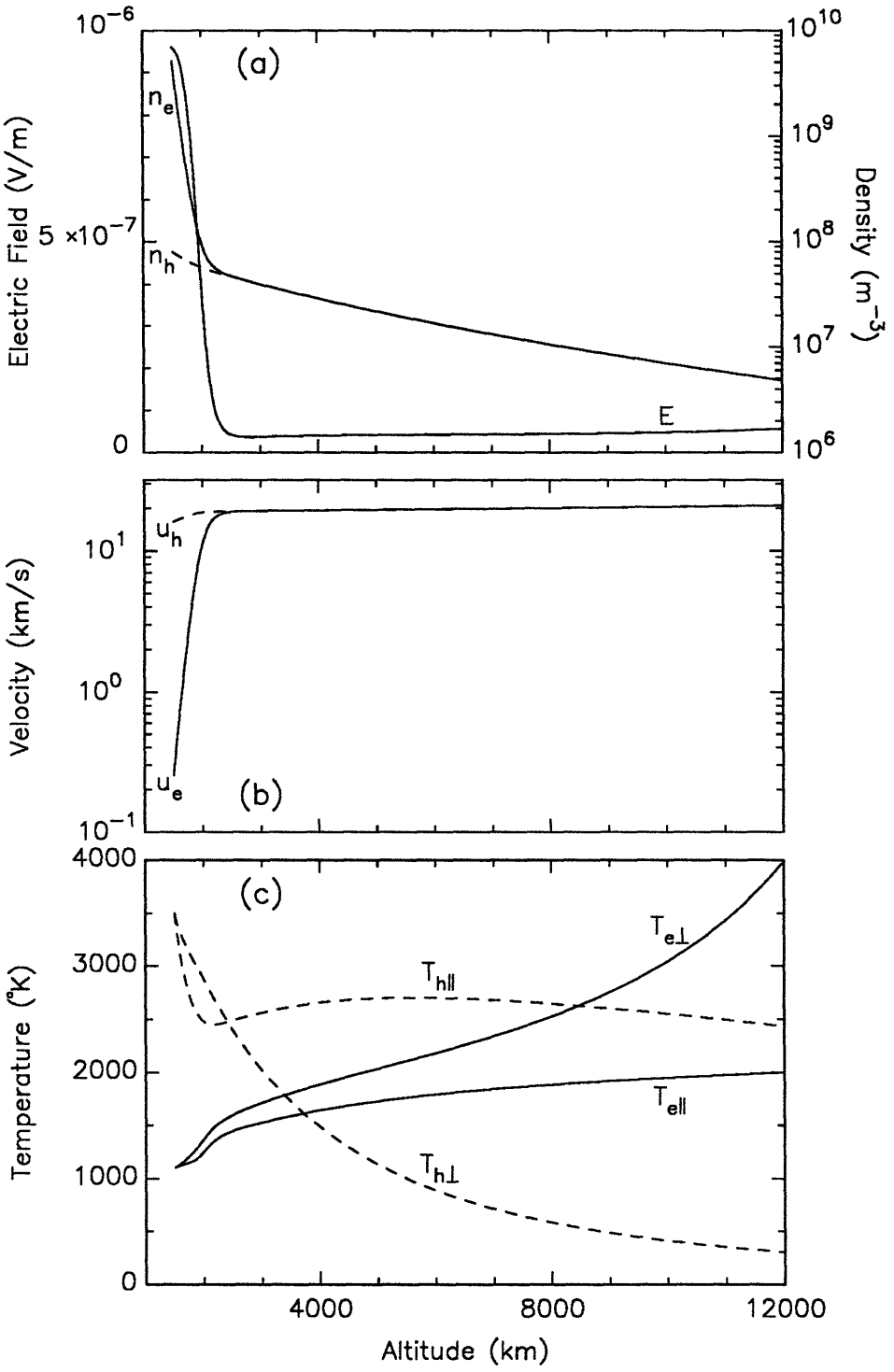

Figure 2-2: Solution to the steady-state 16-moment equations as background for the global kinetic collisional test-particle calculation: (a) Electric field, and H^+ and thermal electron densities. O^+ density is $n_e - n_h$; (b) particle velocities; (c) particle temperatures. O^+ is assumed to be isothermal at 1200 K.

Test e^- energy (eV)	$\nu^{e/e}{}_{\max}$	$\nu^{e/h}{}_{\max}$	$\nu^{e/o}{}_{\max}$	$t^{-1}{}_{\text{momentum}}$	$t^{-1}{}_{\text{energy}}$
1.0	0.6027	0.0103	0.5926	0.2849	0.5697
2.0	0.2130	0.0036	0.2095	0.2014	0.4029
3.0	0.1159	0.0019	0.1140	0.1645	0.3289
4.0	0.0753	0.0012	0.0741	0.1424	0.2849
5.0	0.0539	0.0009	0.0530	0.1274	0.2548
10.0	0.0191	0.0003	0.0187	0.0901	0.1802
15.0	0.0104	0.0002	0.0102	0.0736	0.1471
20.0	0.0067	0.0001	0.0066	0.0637	0.1274

Table 2.1: Typical Coulomb collisional rates and momentum and energy transfer rates for test electrons at 1500 km altitude. The superscripts e, h and o stand for the electron, H^+ and O^+ species respectively. $\nu^{e/i}{}_{\max}$ represents the maximum of slowing-down, parallel and perpendicular diffusion rates for the test electrons, due to collisions with species i.

Test e^- energy (eV)	$\nu^{e/e}{}_{\max}$	$\nu^{e/h}{}_{\max}$	$\nu^{e/o}{}_{\max}$	$t^{-1}{}_{\text{momentum}}$	$t^{-1}{}_{\text{energy}}$
1.0	0.0133	0.0086	0.0047	0.1059	0.2119
2.0	0.0045	0.0030	0.0017	0.0149	0.1498
3.0	0.0025	0.0016	0.0009	0.0612	0.1223
4.0	0.0016	0.0010	0.0006	0.0530	0.1059
5.0	0.0012	0.0007	0.0004	0.0473	0.0947
10.0	0.0004	0.0003	0.0001	0.0335	0.0670
15.0	0.0002	0.0001	0.0001	0.0274	0.0547

Table 2.2: Typical Coulomb collisional rates and momentum and energy transfer rates for test electrons at 2000 km altitude. Notations are the same as in Table 2.1.

electron test particles and the background ions are ignored. Table 2.1 and 2.2 shows some typical collisional rates of suprathermal electrons for their Coulomb interaction with various background species, as well as their rates of momentum and energy transfers due to the electric field, all based on the sixteen-moment solution profiles. By comparing the tables, we can see that the collisional rates in general decrease with the energy of the suprathermal electron as we have discussed in Section 1.2.3, and also with altitude as the densities of the thermal background decrease. Specifically, the collisional rates are much smaller than the momentum and energy transfer rates at 1500 km altitude for electrons with energy above 10 eV (Table 2.1). Such particles are therefore collisionless. At 2000 km altitude, virtually the whole photoelectron energy range is in the collisionless regime. Because of the generally collisionless nature of the photoelectrons, their Coulomb interaction with the background ions can be neglected

to simplify the calculations. The thermal electron background, on the other hand, provides a baseline with which the contributions to various transport quantities by the suprathermal test-particle population can be compared.

We note that the sixteen-moment equations form a set of stiff equations that are highly sensitive to the boundary conditions of higher moments, such as heat fluxes. A slight variation in the heat flux boundary conditions will change the solutions quantitatively, perhaps even qualitatively. This sensitivity, besides the direct relationship between the electric field and the energy flux (and thus the heat flux), provides an additional reason why it is essential to compare the heat fluxes of the photoelectrons with those carried by the thermal electrons.

2.3.2 Calculated Heat Fluxes

Because the kinetic simulation described uses a test-particle approximation, the photoelectron density at some reference altitude must be determined in order to assess the suprathermal contribution to the total heat flux. Recent measurements by the Akebono satellite provide an estimate for the suprathermal to thermal electron density ratio [*Yau et al.*, 1995]. Because of the limitations inherent to the instruments, there are uncertainties in the determination of the electron density. For example, *Yau et al.* [1995] use 10 eV (the low-energy cutoff of their high-energy instrument) as the threshold to distinguish between thermal and suprathermal electrons. In contrast, calculations by *Tam et al.* [1995a] consider 2 eV (still a large multiple of the electron temperature) to be within the suprathermal limit.

Let us calculate this density ratio at higher altitudes. Assuming a density ratio of 10^{-3} at 1500 km, we can determine the suprathermal and thermal electron densities throughout our simulation range (1500 – 12000 km) from the kinetic simulation and the moment-based background calculation, respectively. Figure 2-3 shows that the density ratio increases by an order of magnitude at higher altitude, *i.e.* $n_{suprathermal}/n_{thermal} \sim 10^{-2}$. The sharp increase in the density ratio up to 2000 km is due to the rapid decrease in the background electron density (see Fig. 2-2(a)), the latter being due to a sharp transition from an O^+-dominated to an H^+-dominated

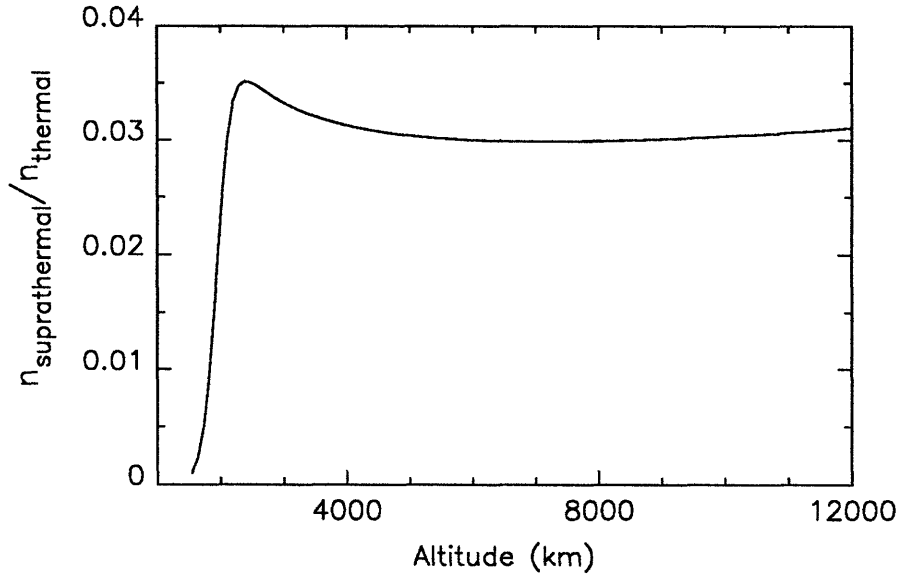

Figure 2-3: Density ratio of suprathermal to thermal electrons.

regime, as the solution to the sixteen-moment equations indicates.

The density ratio profile enables one to determine the mean velocity of the total electron population — thermal and suprathermal combined. With this mean velocity, one may obtain the temperature and heat flux contributions by the suprathermal electrons in the total population. Figure 2-4 shows that the mean electron velocity, and the suprathermal contributions to the temperatures and heat fluxes do not change when we include the ions (H^+, O^+) in the collisional background, thus indicating that photoelectron-ion collisions may be neglected.

Figure 2-5 shows the average parallel and perpendicular heat fluxes per particle (as defined in Eq. (1.13) and (1.14)) carried by the thermal electrons, as part of the solution to the sixteen-moment equations. Notice that the heat fluxes are directed downward (by convention, negative sign), consistent with the idea that the heat flux is in the direction opposite to the temperature gradient (see Fig. 2-2). Their magnitude is to the order of 10^{-15} J-m/s. By comparison, the corresponding contributions by the suprathermal electrons, as shown in Fig. 2-4(c), are on average three orders of magnitude larger (*i.e.* $|q_{suprathermal}/q_{thermal}| \sim 10^3$). The increase in $q_{||}$ and the decrease in $q_{\perp}$ with altitude reflect the transfer of the perpendicular energy into

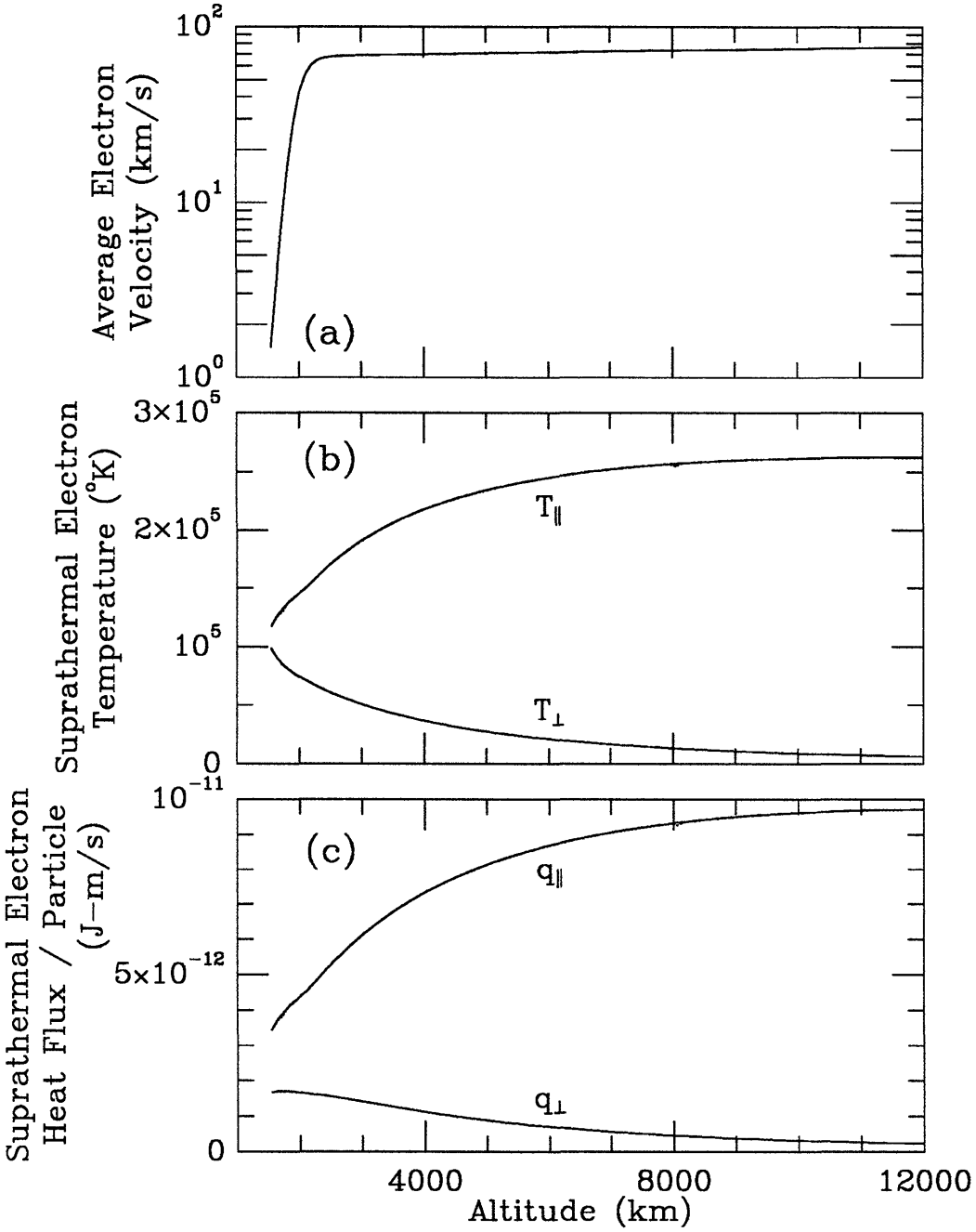

Figure 2-4: Profiles of (a) mean electron velocity for the total electron population, (b) temperature and (c) heat flux contributions by the suprathermal electrons to the total population. Solid lines represent results from the calculation where only thermal electrons are used in the thermal background. Dashed lines represent the case with a full thermal background (H^+, O^+ and electrons). The two sets of lines overlap indicating that photoelectron-ion collisions may be neglected.

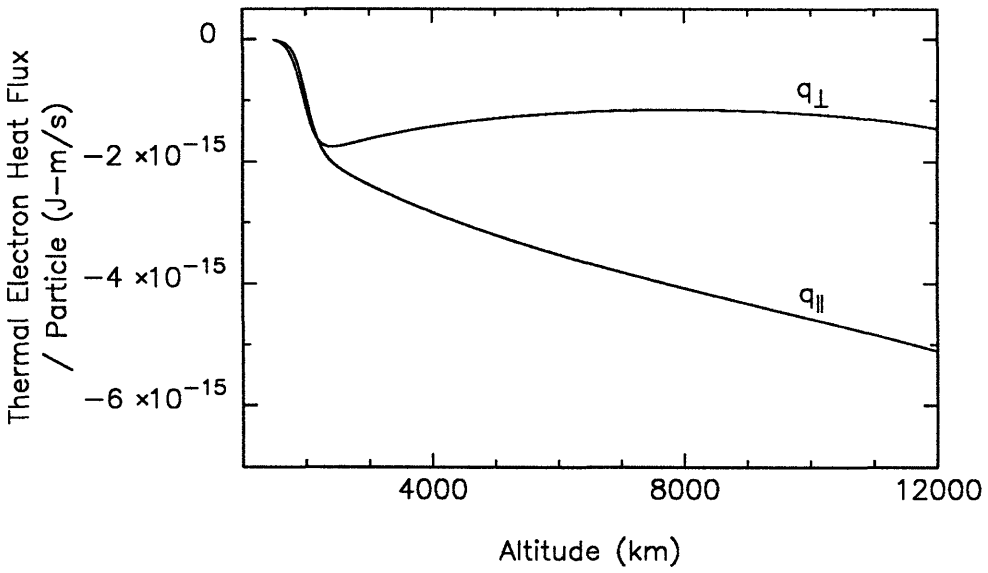

Figure 2-5: Profiles of average parallel and perpendicular heat fluxes per particle carried by the thermal electrons, as calculated from the steady-state 16-moment equations.

parallel energy by the mirror force on the ascending suprathermal electrons. But more importantly, note that the total heat flux contribution carried by the suprathermal electrons is outwardly directed, opposite to the thermal electron heat fluxes.

Knowing the density and the average heat flux contribution of the suprathermal electrons, we can now compare the total heat fluxes modified by the suprathermal electrons with the original moment-generated heat fluxes. The average heat fluxes per particle and the density ratio as calculated above suggest that the heat fluxes, $Q_{\perp,\parallel} = n\, q_{\perp,\parallel}$, carried by the suprathermal electrons are larger than their thermal counterparts by one order of magnitude. In other words, the suprathermal contribution will dominate in the heat fluxes of the total electron population. The total electron heat fluxes ($Q_{\perp,\parallel\ suprathermal} + Q_{\perp,\parallel\ thermal}$) are therefore upward, consistent with *Yau et al.* [1995].

2.3.3 Ambipolar Electric Field

The anisotropy introduced by the suprathermal photoelectrons, characterized by the relatively large amount of upward heat fluxes, is significant in the polar wind transport

because of its influence on the ambipolar field. Let us estimate how this anisotropy modifies the electric field. In the above calculation, introduction of suprathermal electrons to the steady-state moment-based background violates two major assumptions of the classical polar wind — quasi-neutrality and currentless flow. To restore these conditions, a stronger ambipolar field is required. We can estimate the potential that corresponds to this field by modeling the H^+ ion dynamics kinetically. More specifically, we apply the collisionless kinetic approach discussed in Section 1.2.1 to H^+ ions while assuming the transport quantities of other species to be fixed. A bi-Maxwellian distribution whose parameters are based on the moment-generated values is used as the boundary condition at the bottom of the simulation range. The distribution is then allowed to fold along the flux tube, under a potential profile, Φ_E, that is to be determined. By calculating the H^+ density and mean velocity, which now depend on Φ_E, we can find the potential drop and thus the electric field profile that is required to sustain the conditions of quasi-neutrality and currentless flow. As shown in Fig. 2-6, the modified electric field is about an order of magnitude larger than the original, moment-generated field, implying a potential drop of a size comparable to that deduced by *Winningham and Gurgiolo* [1982], and that used in *Yasseen et al.* [1989].

2.4 Discussion

Our preliminary calculations have shown that in the polar wind the bulk of the electron heat flux is carried by the photoelectrons. A heuristic argument based on the quasi-neutral and currentless properties of the flow indicates that this heat flux may induce an order-of-magnitude increase in the ambipolar field. As photoelectrons are primarily generated in the sunlit ionosphere, such a large increase in the electric field due to their presence may account for the recent polar wind observations — day-night asymmetries and enhanced ion outflow velocities — discussed in Section 1.1.2.

Although the calculations above indicate that taking into account the physics of photoelectrons is a step toward theory/data closure, it is necessary to remedy two

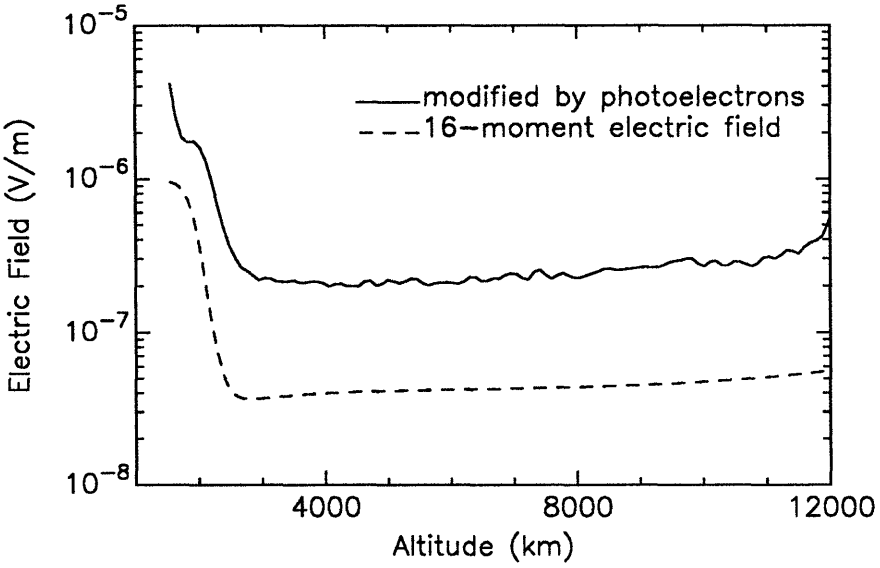

Figure 2-6: Profiles of the moment-generated electric field (dashed) and its modification due to the suprathermal electrons (solid). The new field is about an order of magnitude larger than the original.

shortcomings of the model if the work is to be improved. Specifically, we need to include the O^+ ion dynamics, and more importantly, to deduce the photoelctron effect on the electric field self-consistently.

In the model presented above, O^+ ions are in a stationary barometric equilibrium, as they are assumed to be bound by the terrestrial gravitational force because of their heavier mass. However, this assumption may no longer be valid if we want to include the possibility of an order-of-magnitude enhancement in the polar wind electric field. Indeed, as discussed in Section 1.1.2, data from Akebono [*Abe et al.*, 1993a, 1993b] indicate that polar O^+ ions have larger outflow velocities on the dayside, the sector where photoelectrons are created.

Also, the calculation of the electric field enhancement itself needs to be improved, as it neglects the bulk electron dynamics. While the increase in the electric field enhances the ion outflow, it can also suppress the outward flow of the bulk electrons. Such modifications of the thermal particle transport will have a feedback effect on the polar wind electric field itself. In fact, all the polar wind components (ion species,

thermal electrons, photoelectrons) and the ambipolar electric field all influence each other. To determine the electric field, one must take into account these self-consistent effects. In the next chapter, we shall introduce a self-consistent hybrid model which addresses both issues. The model determines the electric field self-consistently, while removing the restriction imposed by static O^+ ions.

Chapter 3

A New Self-Consistent Approach

The main difficulty in incorporating an accurate theoretical description of photoelectrons into a self-consistent polar wind picture is the global kinetic collisional nature of the flow. Even though photoelectrons represent only a minority species in the polar wind, and thus can be treated as test particles, a self-consistent kinetic description of their collisions is still rather difficult to achieve; the simplified collisional operator, such as the linearized Fokker-Planck collisional operator (Eq. (2.7)), is still rather complicated, and is based on parameters from the background species, whose transport properties are influenced by the photoelectrons themselves directly (via Coulomb collisions) and indirectly (via the electric field).

Traditional self-consistent approaches are seemingly inadequate to describe the entire polar wind picture self-consistently. For example, the collisionless kinetic approach obviously omits the Coulomb interactions between the particles. Collisional moment-based models use velocity-averaged collisional rates, and therefore cannot describe the observed kinetic features of the distribution function.

An alternative approach is to use computer simulations. An ideal model would be the particle-in-cell (PIC) simulation, which closely follows the trajectory of each simulated particle in time while taking into account all the forces acting on the particle, including those due to Coulomb collisions. Although PIC simulation may be a solution to the collisional representation problem, there is a restriction on the time step used in the calculation. Indeed, the time step must be smaller than the shortest

time scale among all the particle species. In the polar wind and most other non-turbulent applications, that would correspond to the collisional time for the thermal electrons due to their relatively high density and low mass (*c.f.* Eq. (2.11)). Because of the large mass difference between the ions and electrons, their time scales are also very different. The effort with PIC simulation in tracing the ions with time steps comparable to the thermal electron time scales therefore seems inefficient. For applications that involve a macroscopic or mesoscopic scale, such as the polar wind, whose spatial scale is thousands of kilometers, the PIC simulation process, being slowed down by the thermal electron time scales, is exceedingly time-consuming and therefore impractical.

To avoid the problem caused by the short time scales of thermal electrons, some investigators resort to a semi-kinetic approach [*Wilson et al.*, 1990; *Ho et al.*, 1992]. This approach provides a kinetic description for the ions as they are simulated based on the PIC technique. Electrons, on the other hand, are treated as a massless neutralizing fluid. Because the only active components in the simulation are the ions, this model may use time steps determined by the shortest ion time scale, which is in general much larger than that of the thermal electrons. However, because of its electron treatment, the semi-kinetic approach obviously does not take into account any effect due to the non-thermal features of the electrons.

3.1 Self-Consistent Hybrid Model

Recently, the author has developed a model to circumvent *all* the difficulties discussed above [*Tam et al.*, 1995b]. The model is called the *self-consistent hybrid* model. It is hybrid in that it consists of a kinetic and a fluid component. Photoelectrons (treated as test particles because of their low relative density) and both H^+ and O^+ ions are described using a global kinetic collisional approach while thermal electron properties are determined from a simpler, fluid approach that also calculates the self-consistent ambipolar electric field. The model is based on an iterative scheme combining the kinetic and fluid calculations, that should converge to physically meaningful solutions.

3.1.1 Fluid Component

The fluid component of the model uses the five-moment assumption for the thermal electrons, *i.e.*, a drifting Maxwellian distribution. This distribution, combined with the photoelectron results obtained from the kinetic component of the model, would form the total electron distribution. One of the purposes of the fluid calculation is to determine the various parameters that constitute the Maxwellian distribution.

The density and drift velocity of the thermal electrons are determined from the quasi-neutral and current-free constraints characterizing the classical polar wind, with input of densities and flow velocities of the other particle components (H^+, O^+ and photoelectrons) obtained from the kinetic part of the model. In particular, the current-free condition is:

$$n_e u_e + n_s u_s = n_h u_h + n_o u_o, \tag{3.1}$$

where the subscripts e, s, h, and o stand for the thermal electron, suprathermal electron (photoelectron), H^+ and O^+ species respectively. Notice that because the profiles of all the particle species (except for thermal electrons) have already satisfied the continuity equation (Eq. (2.1)), by imposing the current-free condition throughout the whole simulation range, the resulting thermal electron density and velocity profiles must also satisfy the continuity equation.

The thermal electron temperature, and the ambipolar electric field, are obtained from the moment equations of the next two higher orders, *i.e.* the momentum and energy transfer equations for the whole electron population:

$$B\frac{\partial}{\partial s}\left(\frac{n_e T_e + n_e m_e {u_e}^2 + n_s T_{s\parallel} + n_s m_e {u_s}^2}{B}\right) + (n_e + n_s)\left(m_e\frac{\partial \Phi_G}{\partial s} - e\frac{\partial \Phi_E}{\partial s}\right) + \frac{B'}{B}(n_e T_e + n_s T_{s\perp}) = \frac{\delta M_e}{\delta t} + \frac{\delta M_s}{\delta t}, \tag{3.2}$$

$$B\frac{\partial}{\partial s}\left[\frac{n_e u_e}{B}\left(\frac{5}{2}T_e + \frac{m_e {u_e}^2}{2}\right) + \frac{Q_{ws}}{B} + \left(\frac{n_e u_e}{B} + \frac{n_s u_s}{B}\right)(m_e \Phi_G - e\Phi_E)\right] = \frac{\delta \mathcal{E}_e}{\delta t} + \frac{\delta \mathcal{E}_s}{\delta t} \tag{3.3}$$

where e is the unit charge, and $\delta M_{e,s}/\delta t$ and $\delta \mathcal{E}_{e,s}/\delta t$ represent the momentum and energy transfers to the thermal and suprathermal electrons due to Coulomb collisions. As will be explained in the next section, these collisional transfer values are supplied by the kinetic component of the model.

3.1.2 Kinetic Component

As mentioned earlier, a self-consistent kinetic collisional description is very difficult to achieve. One reason is the non-linear dependence of the collisional operator. (The operator depends on the distribution function of the species itself.) This non-linearity represents self-collisions, interaction among particles of the same component. Indeed, a proper description of self-collisions is a prerequisite for a self-consistent model. The kinetic part of the self-consistent hybrid model takes into account self-collisions using a simple, but non-trivial technique.

Basically, the kinetic calculation is based on the global kinetic collisional test-particle model originally developed by *Retterer et al.* [1987], and described in Chapter 2. In this self-consistent hybrid technique, kinetic calculations are used to describe the photoelectrons, and all the ions (H^+ and O^+).

Photoelectrons, due to their low relative density, can be treated as test particles. In other words, their dynamics can be described by an equation similar to Eq. (2.7), where the collisional operator does not depend on the photoelectron distribution itself. Therefore, the global kinetic collisional test-particle model will provide a sufficient description of photoelectrons, provided we use a self-consistent background that consists of the thermal electrons, and the ambipolar electric field. In principle, the background should also include H^+ and O^+ ions. However, because the background ion species do not affect the results significantly, but increase the calculation time by a large amount, we ignore their collisions with the photoelectrons.

In principle, each ion species should be described by an equation similar to Eq. (1.1), in which the Coulomb collisional operator depends on the ion distribution function itself because in contrast to photoelectrons, self-collisions for the ions may no longer be neglected. We circumvent this intrinsic non-linearity with an iter-

ative linearization scheme, which will enable us to take such collisions into account. With the global kinetic collisional test-particle model, we perform calculations for both ion species using the same background as that in the photoelectron simulation. The background electric field and thermal electron quantities are obtained from the fluid calculation; the background temperatures, velocities and densities of the ion species are obtained from the *previous* iteration. The new calculations for both ion species then provide updated ion densities, velocities and temperatures which will be used as the background ion profiles in the *next* iteration. This iteration scheme, when it converges, takes into account the non-linear dependence of the collisional operator on the distribution function.

3.1.3 Coupling Between Fluid and Kinetic Calculations

The self-consistent hybrid model is based on an iterative scheme between the fluid and kinetic calculations. Together, they cover the properties of all four particle components — thermal electron, photoelectron, H^+ and O^+ — and the ambipolar electric field in the classical polar wind. A self-consistent solution is obtained when the iterative scheme converges. Because the electric field and the particle components all influence each other, the calculation for each component requires the outputs for all the other components.

As described above, each of the kinetic calculations — for photoelectrons, H^+ or O^+ — requires profiles of the thermal electron density, velocity and temperature from the fluid calculation such that the collisional impact by the bulk electrons can be determined. The fluid calculation also provides the electric field profile that is essential for the dynamics of the polar wind. As for the collisional effect due to the ion species (which includes the species itself), their background density, velocity and temperature profiles come from the *previous* round of kinetic calculations.

For the fluid calculation, the classical polar wind conditions — quasi-neutrality and current-free flow — require the density and velocity profiles from all the kinetically described components. The thermal electron quantities and the electric field, obtained from the coupled equations (Eq. (3.2) and (3.3)), are based on results from

the photoelectron calculation, and the rates of momentum and energy transfer due to collisions. As we shall explain, these rates are also supplied by the kinetic calculations.

Collisional Momentum and Energy Transfer Terms

As mentioned earlier, the kinetic calculation is based on the Monte Carlo technique, which uses a finite but representative sample of phase space elements to represent the distribution function of the test-particle species, and follows the phase space trajectories of these elements. One important aspect about the Monte Carlo technique is that it readily separates the contribution to phase space evolution due to each single physical effect. To determine the rates of collisional momentum and energy transfer, let us focus on the effect of Coulomb interaction with a given background species. Collisions with the background species are represented by velocity perturbations of the phase space elements. By using the same method that calculates the various velocity moments of the test species, we can aggregate such phase space perturbations to determine the changes (or rates of changes) in any velocity moment caused by these collisions. In particular, for a test species α and a background species β, we are interested in the rates of momentum and energy transfer from species β to α, respectively defined as:

$$\left(\frac{\delta M_\alpha}{\delta t}\right)_\beta = \int d\mathbf{v}\, m_\alpha v_\parallel \left(\frac{\delta f_\alpha}{\delta t}\right)_\beta \tag{3.4}$$

and

$$\left(\frac{\delta \mathcal{E}_\alpha}{\delta t}\right)_\beta = \int d\mathbf{v}\, \frac{1}{2} m_\alpha v^2 \left(\frac{\delta f_\alpha}{\delta t}\right)_\beta . \tag{3.5}$$

Because Coulomb collisions are elastic, both momentum and energy must be conserved. In other words, there is no loss of momentum or energy in the collisions between any two given species. Therefore, the following relations must hold true:

$$\left(\frac{\delta M_\alpha}{\delta t}\right)_\beta = -\left(\frac{\delta M_\beta}{\delta t}\right)_\alpha \tag{3.6}$$

and

$$\left(\frac{\delta \mathcal{E}_\alpha}{\delta t}\right)_\beta = -\left(\frac{\delta \mathcal{E}_\beta}{\delta t}\right)_\alpha \tag{3.7}$$

Indeed, these relations can be derived by making use of the asymmetric nature of the Coulomb collisional operator, such as the Fokker-Planck operator in Eq. (2.3). Because of Eq. (3.6) and (3.7), the global kinetic collisional test-particle model can calculate not only the rates of collisional momentum and energy transfer from each background species to the test species, but also *vice versa.*

In particular, in the kinetic calculation for each species, we are interested in their momentum and energy transfer rates associated with the thermal electron background. The collisional transfer rates to the thermal electron species from each of the other particle component (H^+, O^+ and photoelectron) are then found. With the relations

$$\frac{\delta M_e}{\delta t} = \left(\frac{\delta M_e}{\delta t}\right)_h + \left(\frac{\delta M_e}{\delta t}\right)_o + \left(\frac{\delta M_e}{\delta t}\right)_s, \tag{3.8}$$

and

$$\frac{\delta \mathcal{E}_e}{\delta t} = \left(\frac{\delta \mathcal{E}_e}{\delta t}\right)_h + \left(\frac{\delta \mathcal{E}_e}{\delta t}\right)_o + \left(\frac{\delta \mathcal{E}_e}{\delta t}\right)_s, \tag{3.9}$$

the collisional terms in the coupled fluid equations, Eq. (3.2) and (3.3), are thus determined.

3.1.4 Advantages of the Model

The complete scheme of the self-consistent hybrid model is summarized in Fig. 3-1. This new technique retains the expediency of fluid theory while in effect extending its applicability with the combination of kinetic descriptions. One of the advantages of the model is clearly its ability to incorporate the global kinetic collisional physics of photoelectrons into a self-consistent polar wind description. In fact, this is the first polar wind model to achieve that. As fluid calculations alone fail to describe the non-thermal electron features observed in the polar wind, the technique used in this model not only provides a kinetic description of these features, but also takes into account their impact on the polar wind.

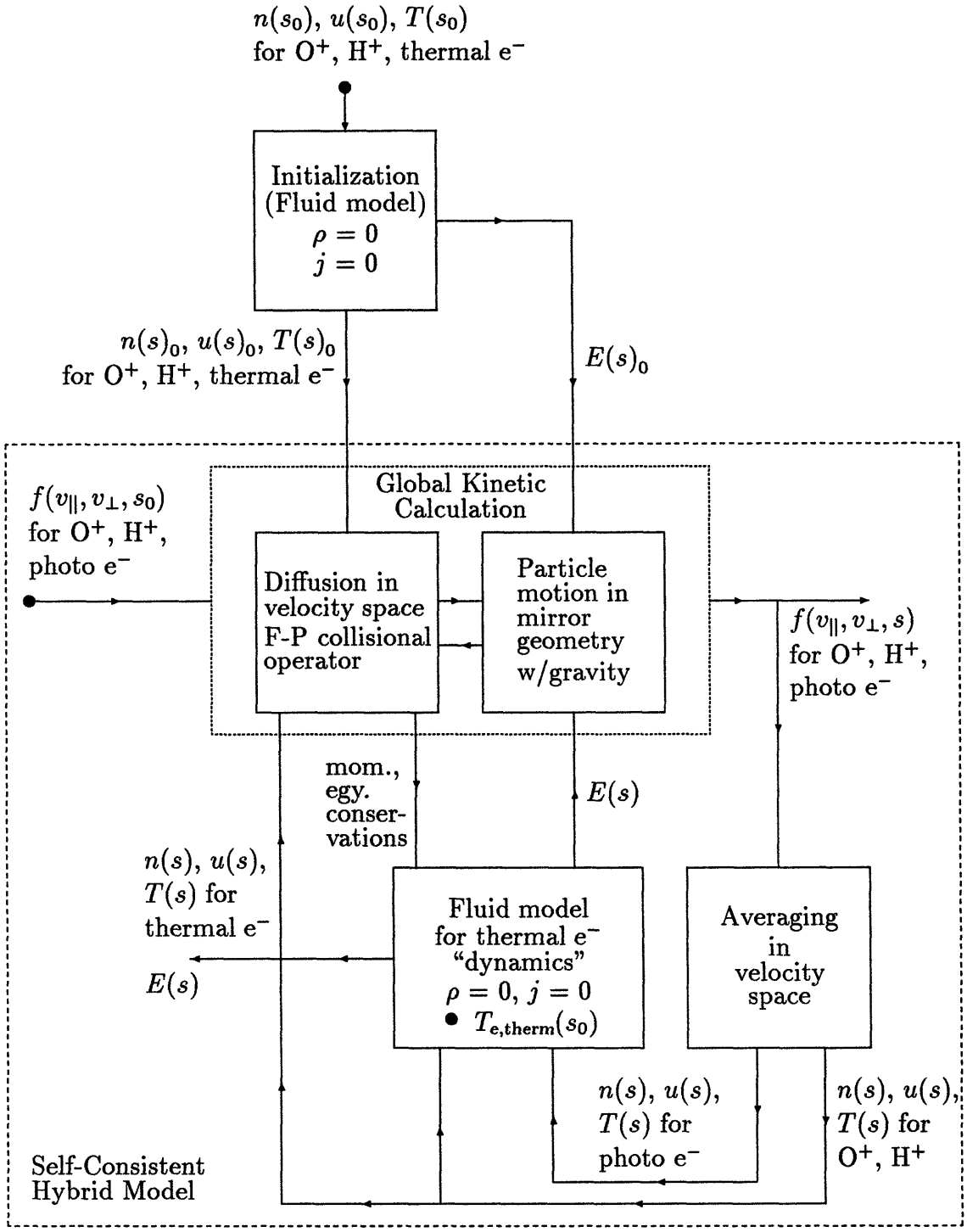

Figure 3-1: A flow chart illustrating the whole scheme of the self-consistent hybrid model.

Another difficulty that the self-consistent hybrid model has circumvented is the treatment of the transonic region, which introduces singularities to most moment-based calculations, as discussed in Section 1.2.2. In the polar wind, the flows of both H^+ and O^+ are observed to be supersonic at high altitude. Thus, there must be a transonic region where the nature of the flows changes from subsonic to supersonic. As discussed in Section 1.2.2, most moment-based models have difficulties describing transonic flows because of the singularities intrinsic to the calculations, specifically, those near the sonic points. In the self-consistent hybrid model, however, the dynamics of the ion species are described based on kinetic calculations. Due to the kinetic treatment of the ions, the difficulty arising from the transonic region of the ions is not an issue to the model. Indeed, the self-consistent hybrid model is the first global polar wind model to obtain a continuous steady-state solution that varies from a subsonic collisional regime at low altitude to a supersonic collisionless regime at high altitude [*Tam et al.*, 1995b].

The model also successfully deals with problems usually encountered by other simulation techniques. For example, simulating the Coulomb collisions among ions of the same species is not trivial, and is usually an obstacle to a self-consistent approach; this model takes into account such self-collisions by means of an iterative scheme. The relatively short time scales of thermal electrons, as compared to those of the ions, would slow down the simulation process considerably. In this model, the thermal electrons are described by a fluid approach, and present in the simulations only as a steady-state background. The kinetically described particle components are separately treated, and may also only appear as a background in the simulations of the other species. In other words, the particle component whose dynamics is being calculated is the *only* active component in a simulation. The motions of the particles can thus be followed based on time steps comparable to their own time scales. This technique, by its fluid treatment of thermal electrons, can evolve using relatively large time steps consistent with ion and suprathermal electron collisional time scales, and is not constrained by the much shorter thermal electron collisional time scale.

3.2 Application to the Classical Polar Wind

The self-consistent hybrid model is developed for the classical polar wind in which the plasma outflow is mainly driven by the photoelectron flux through the field-aligned ambipolar field, a scenario that corresponds to the daytime polar conditions. Application of the model to the sunlit polar region has generated results [*Tam et al.*, 1995b] that are qualitatively consistent with various observed polar wind features [*Abe et al.*, 1993b; *Yau et al.*, 1995]. Here, we shall make another step toward theory/observation closure, emphasizing the quantitative aspect as well with a more recent solution, where the local electric field has converged to within 2% throughout the simulation range (500 km – 2 R_E, where R_E is the radius of the earth). In this calculation, initial distributions for the kinetic part of the model are applied at the lower boundary, and are associated with the upper half of the modified Maxwellian distribution shown in Eq. (2.21). The ions are initially distributed with the temperature parameter T_* being 1.0 eV for H^+ and 2.2 eV for O^+. The initial photoelectron distribution is the same as that used in Section 2.3, except for a lower initial altitude. For the fluid component of the model, boundary conditions are also imposed at the lower end: the H^+ and O^+ densities are 1.5×10^9 and 4×10^{10} m^{-3} respectively; a photoelectron to thermal electron density ratio of 0.1% is assumed, and the thermal electron temperature is taken to be 3000 °K.

The self-consistent electric potential profile for this set of initial and boundary conditions is shown in Fig 3-2. A potential drop of about 5 V is obtained across our simulation range. This value is consistent with the magnitude deduced from reflected photoelectron fluxes [*Winningham and Gurgiolo*, 1982]. The potential difference is expected to increase if the initial low-altitude photoelectron spectrum is more energetic or, as we shall show in the next chapter, if photoelectrons have a higher relative density. Similarly, in night-time conditions, where photoelectrons are essentially absent, the potential difference would be smaller. The effect of the suprathermal to thermal electron density ratio will be discussed in more detail in Chapter 4.

The density profiles for all the species in our calculation are shown in Fig. 3-3.

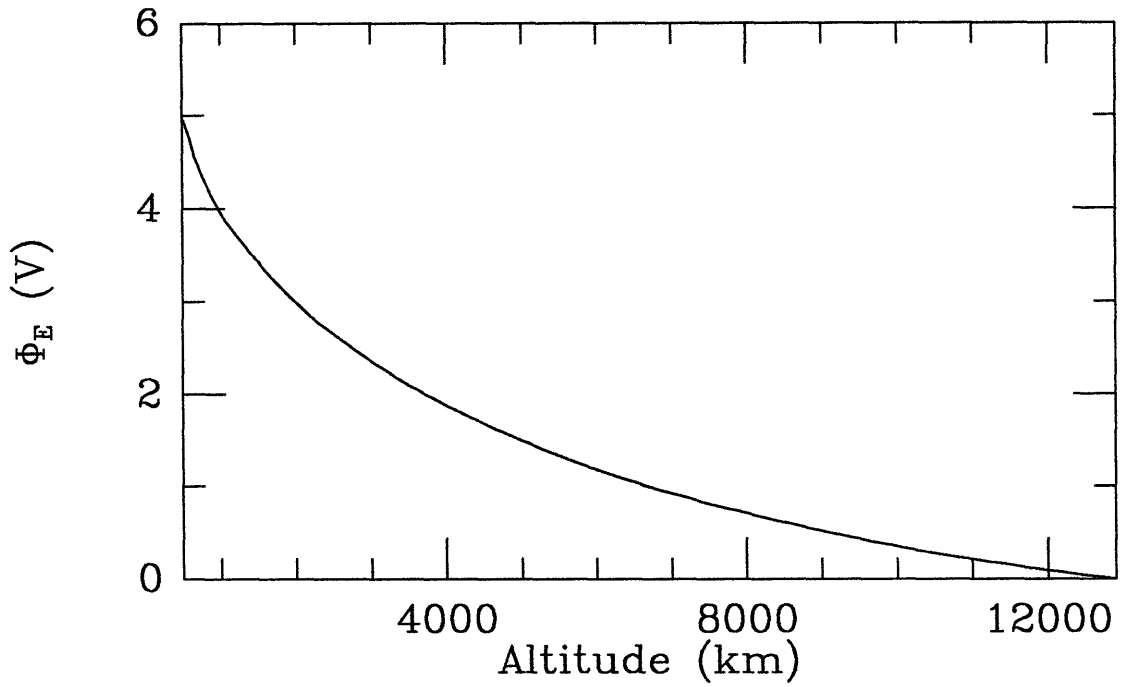

Figure 3-2: Electric potential profile calculated by the self-consistent hybrid model. The magnitude of the potential drop is comparable to value deduced from observations.

First of all, the photoelectron density n_s is small compared with the thermal electron density. Our test-particle approach for photoelectrons is therefore justified. The results also show that O^+ , being driven by the self-consistent ambipolar field, maintains its dominance over H^+ even at high altitudes, in agreement with Akebono observations. From 5000 to 9000 km, the O^+ and H^+ densities are to the orders of 10^9 and a few times 10^7 m^{-3}, consistent with the respective lower limit estimates — 10^8 and 10^7 m^{-3} — obtained from Akebono measurements [*Abe et al.*, 1993b]. Because of the quasi-neutrality condition, the two major particle species, O^+ and thermal electron, have very comparable densities.

Figure 3-4 shows the outflow velocities of the ions. Note that in general the outflow velocities for both ion species increase with altitude. At high altitudes (5000 – 9000 km), downwardly moving ions only constitute less than 2% of the density. This feature is consistent with the supersonic nature of the outflows at these altitudes. (In the results shown in *Tam et al.* [1995b], where the self-consistent electric field was

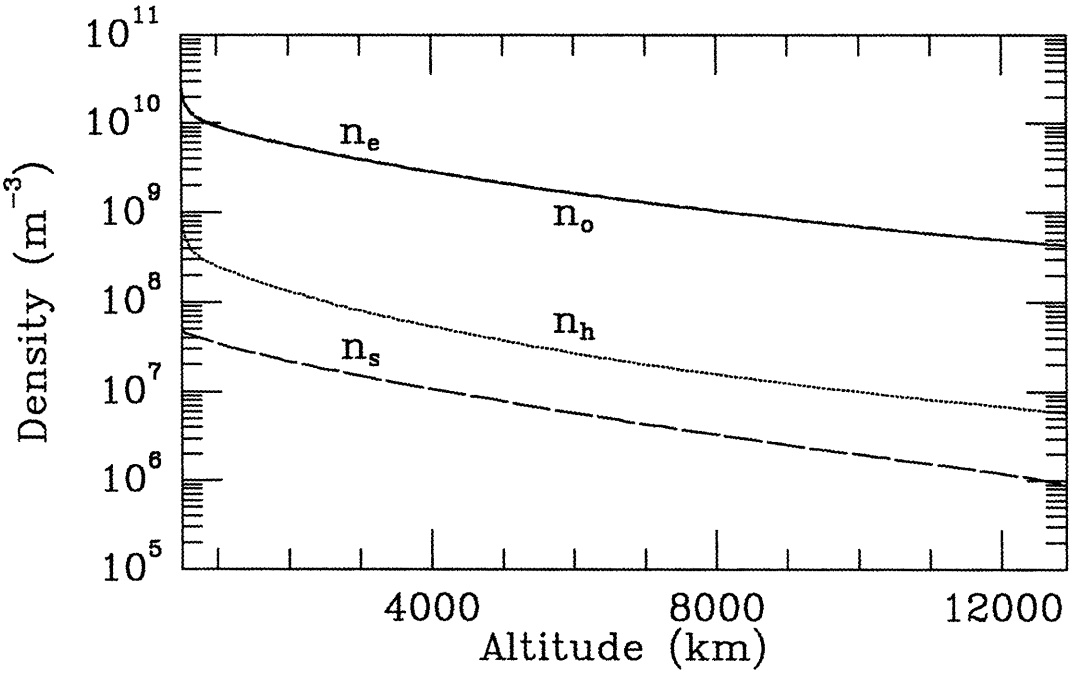

Figure 3-3: Calculated density profiles for O^+ (n_o), H^+ (n_h), thermal electron (n_e), and photoelectron (n_s).

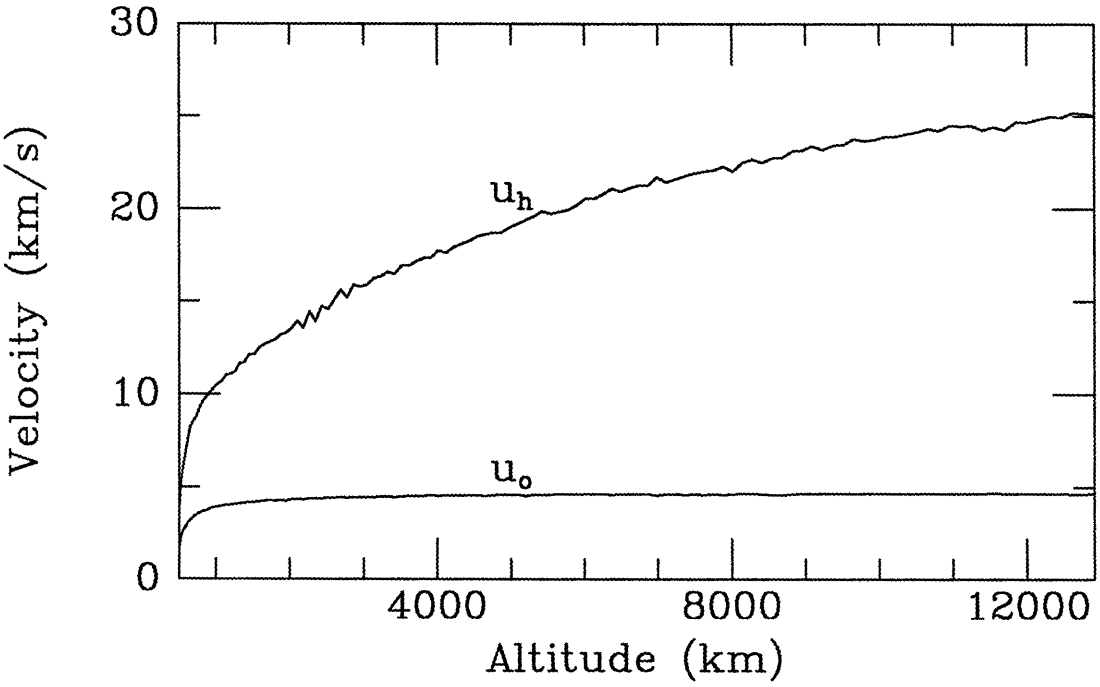

Figure 3-4: Profiles of calculated ion outflow velocities.

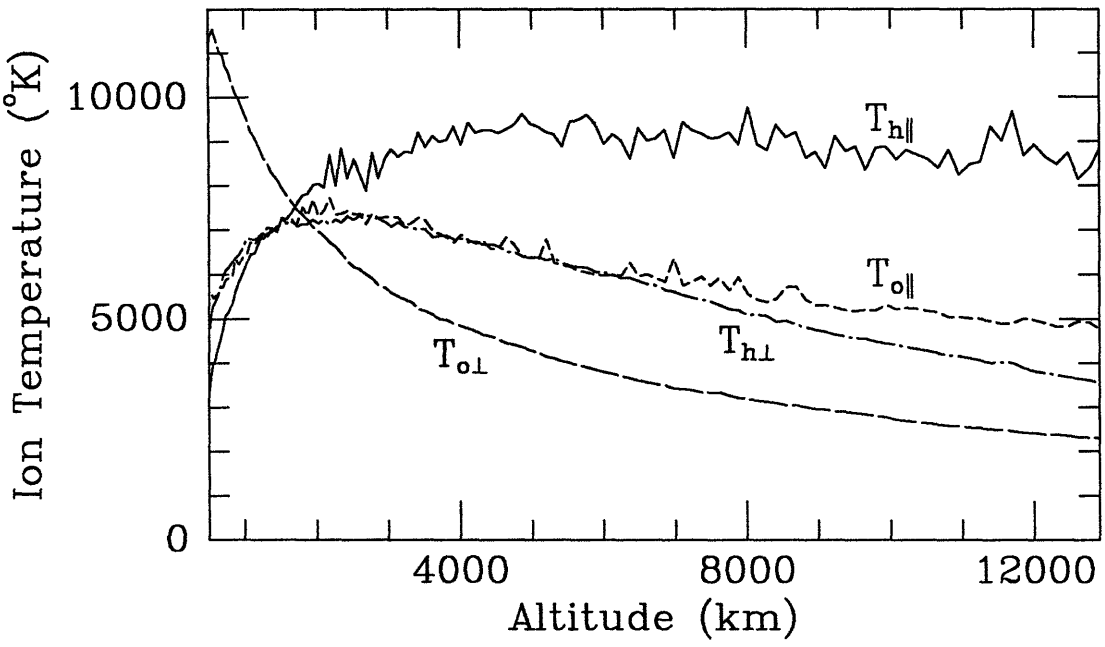

Figure 3-5: Profiles of calculated ion temperatures.

higher, downwardly moving ions were even absent.) Not only are these ion velocity profiles consistent with the Akebono observations qualitatively, but, moreover, their high-altitude values of about 20 km/s for H^+, and 4 km/s for O^+ are also within the measurement limits [*Abe et al.*, 1993b]. Of course, when there are special magnetospheric/ionospheric conditions other than the photoelectrons affecting the plasma flow in the polar cap, these results may be altered [*Chandler*, 1995]. However, such situations are beyond the scope of this model, in its present form.

The ion parallel and perpendicular temperatures obtained from the kinetic calculations are shown in Fig. 3-5. The temperatures are less than but to the order of 10^4 °K, which is the upper limit estimated from Akebono measurements [*Abe et al.*, 1993b]. The ion temperatures here are higher than those in *Tam et al.* [1995b] because the present calculation is performed with larger energy spreads in the initial ion distributions. Because these initial distributions only consist of the upgoing half of the ions, (which may be reflected due to the gravitational potential), a larger energy spread generally implies a higher intrinsic energy flux. This effect will tend to reduce the field-aligned potential drop, as suggested by Eq. (2.2). We shall discuss the effect

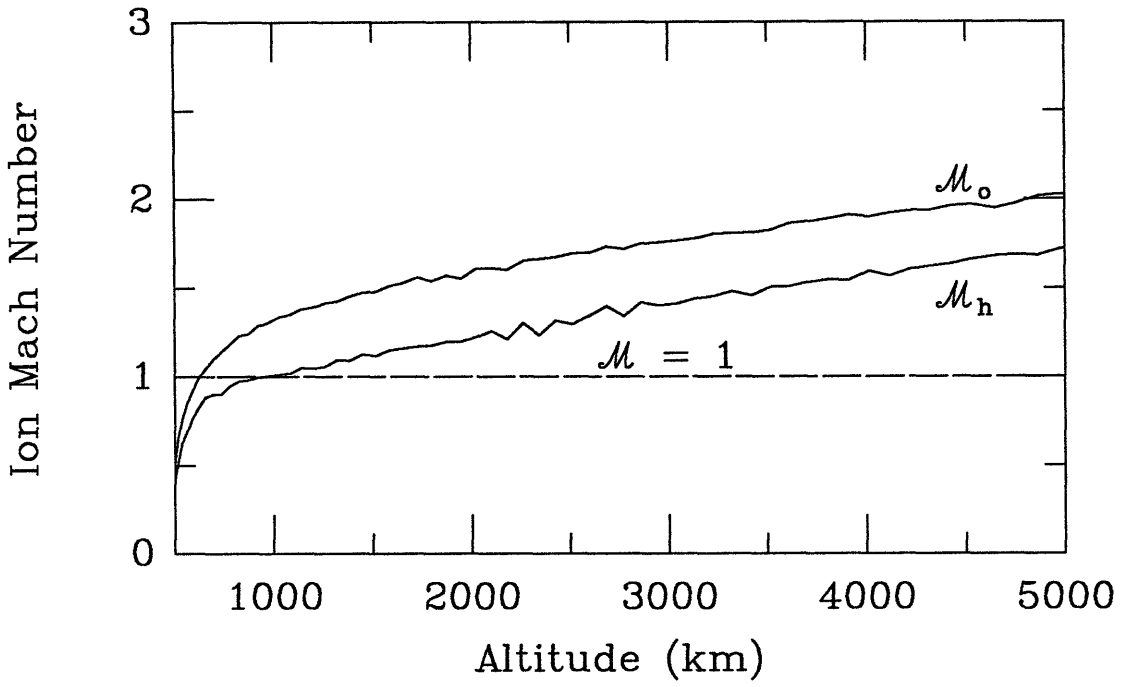

Figure 3-6: Ion Mach numbers.

of the ion temperatures further in Chapter 4.

The Mach number, defined for each ion species j as:

$$\mathcal{M}_j = \sqrt{\frac{m_j u_j^2}{2T_j}}, \tag{3.10}$$

increases in general with altitude due to the upward gradient of the outflow velocities and the downward gradient of the temperatures (see Fig. 3-4 and 3-5). From Fig. 3-6, it is clear that the continuous solution spans the subsonic and supersonic regimes of both ion species. In particular, both ion species attain supersonic flows at high altitudes, in agreement with Akebono observations [*Abe et al.*, 1993b].

In order to compare our results with Akebono's electron measurements [*Yau et al.*, 1995], we combine all the electrons (thermal and photoelectrons) in the calculation into a single population. The thermal electrons in this total population are assumed to be in a drifting Maxwellian distribution whose density, velocity and temperature are determined as explained in Section 3.1.1. The resulting Maxwellian and the ki-

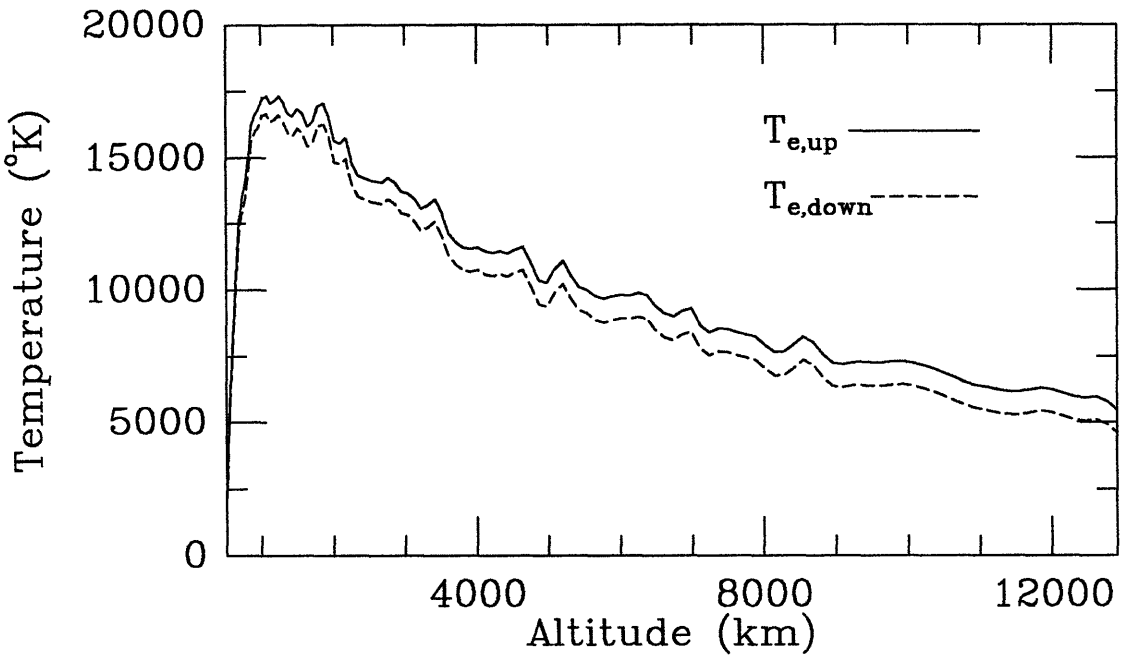

Figure 3-7: Parallel temperatures for upwardly and downwardly moving electrons, the || subscript has been omitted for simplicity.

netic results for the photoelectrons combine to give the total distribution of the electron population. This total distribution is then divided into two components: $f_{e,up}$ and $f_{e,down}$, corresponding to upwardly and downwardly moving electrons, respectively. The parallel temperature profiles obtained from these components are shown in Fig. 3-7. The solution reveals a temperature anisotropy between the upwardly and downwardly moving electrons, *i.e.* $T_{e,up} > T_{e,down}$ (the || subscript is omitted for simplicity). In the calculation, this anisotropy is entirely due to the photoelectrons. Because such a temperature anisotropy was observed in the dayside polar wind [*Yau et al.*, 1995] but seems absent on the nightside [*Abe et al.*, 1996], the role of photoelectrons in the model is consistent with the observed polar wind scenario. This anisotropy also produces an upwardly directed total heat flux for the entire electron population, as shown in Fig. 3-8, and is consistent with the observations by the Akebono satellite [*Yau et al.*, 1995]. Despite such a temperature anisotropy introduced by the photoelectrons, the overall temperature profile still seems to be dominated by the thermal electrons. This justifies the use of the thermal electron temperature in

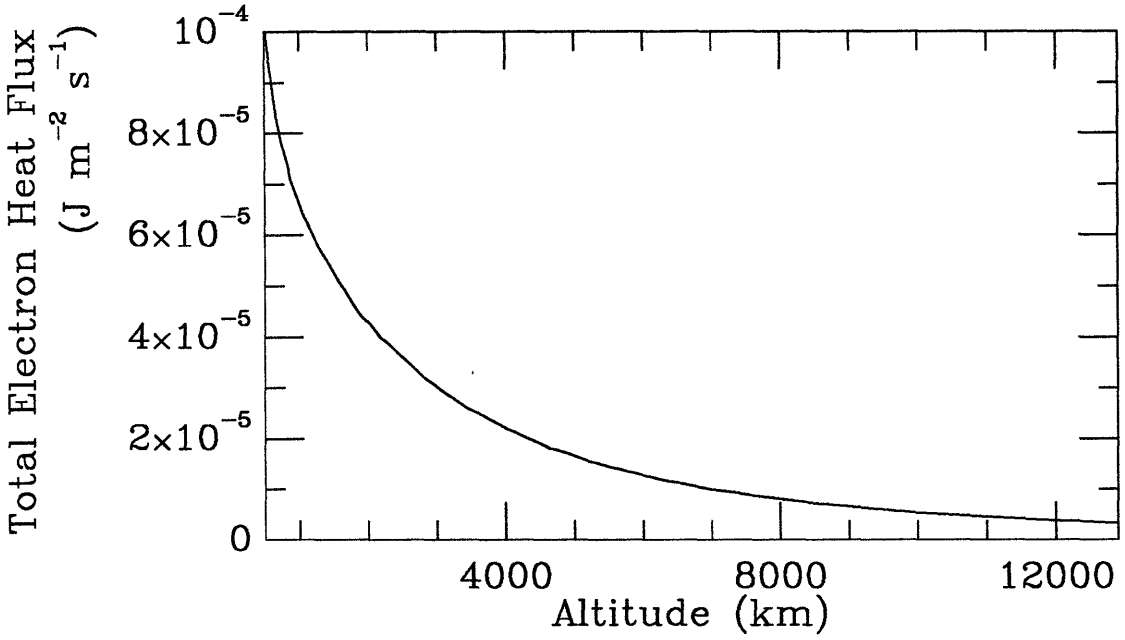

Figure 3-8: Total heat flux profile for the total electron population.

the collisional operator of the kinetic calculations, and thus the test-particle approach for photoelectrons.

3.3 Possible Extensions of the Model in the Polar Wind Application

We have demonstrated theory/observation closure of the photoelectron driven classical polar wind by establishing qualitative and quantitative consistency between results obtained from the self-consistent hybrid model and data from the Akebono satellite. The model can easily be extended so that its results can be compared to a wider range of polar outflow conditions.

First of all, the model can be readily applied to the night-time polar wind where photoelectrons are virtually absent — this can be done by setting the photoelectron to thermal electron density ratio to zero in the fluid calculation. In Chapter 4, we will compare the polar wind results generated by the model based on different boundary conditions for this density ratio, including one that corresponds to the night-time

condition.

The model, in its present form, has assumed that the open magnetic field line in the polar cap region is radial, and that transport in the polar wind is important only in the field-aligned direction. Particle drifts transverse to the magnetic field, such as those due to the convective electric field and the curvature of the geomagnetic field lines, are ignored. In principle, one could extend the model to include such drifting motions. Because the sources of these drifts are due to the configuration of the background, one can incorporate these effects into the model by introducing the resulting drift velocities into the Monte Carlo simulations.

Because the polar cap is a relatively quiescent region, our model has not examined the possibility of wave-particle interaction. Nevertheless, the model can be used to investigate wave instabilities, and incorporate them self-consistently into the steady-state polar wind description if any exists. Because the model uses kinetic descriptions for all the particle components except thermal electron, which is assumed to be a drifting Maxwellian distribution, results generated by the model are in terms of distribution functions, and thus can be readily used to investigate local instabilities. Instead of the fluid equations, the model would consist of a dispersion relation, in which the particle distribution functions would be supplied by the kinetic calculations. In the case that any wave instability is found, the model can also incorporate its effect on the particles. This is because wave turbulence, like Coulomb interaction, can be represented by a collisional operator in the kinetic equation. By replacing the Coulomb collisional operator with the wave operator, we can find a new Langevin equation, and carry out the Monte Carlo simulations accordingly. Indeed, the Monte Carlo technique used in this model has been applied to find particle distributions under wave turbulence [*Retterer et al.*, 1983]. With an iterative scheme between the dispersion relation and the new kinetic calculations for the particle distributions, convergence of the model will yield a steady-state solution that takes into account wave-particle interaction.

Recent studies have shown that waves can be generated non-locally and propagate to the regions of interest where they interact with the plasma [*Johnson et al.*, 1995,

and references therein]. The generation of these waves is beyond the scope of this work. However, their effect may be readily, and heuristically, included, based on measured spectrum, for example.

In general, the technique used by the self-consistent hybrid model is so powerful that it can be applied to a variety of steady-state problems, even when a large scale inhomogeneous plasma is involved, as in the case of the classical polar wind. In Chapter 5, we will demonstrate the versatility of this self-consistent hybrid technique by applying the model to the solar wind.

Chapter 4

Polar Wind Parametric Studies

Polar-orbiting satellites, such as DE-1, DE-2 and Akebono, have measured or estimated various polar wind quantities, *e.g.* the ion and electron outflow characteristics, and the corresponding ambipolar potential difference [*Winningham and Gurgiolo*, 1982; *Abe et al.*, 1993a, 1993b; *Yau et al.*, 1995]. The values obtained from the satellite data for these quantities should correspond to those arising from a particular set of polar wind condition. However, these observed values may not be representative enough for the polar wind in general because of the variability of the polar wind settings.

Indeed, the dynamics of the polar wind depends on a number of conditions. For example, the correlation between the H^+ outflow velocity and the amount of magnetic activity, *i.e.* the K_p index, calculated by *Abe et al.* [1993a] from Akebono data, seems to indicate an increase of the velocity gradient with the K_p index on a time scale of several days. For K_p index of shorter time scales, however, no conclusion has been drawn because of insufficient statistical data.

The polar wind dynamics, evidently, also depends on the magnetic local time, as implied by the day-night asymmetries that have been observed by the Akebono satellite [*Abe et al.*, 1993b, 1996; *Yau et al.*, 1995], and discussed in Chapter 1. The magnetic local time is related to the solar zenith angle. Indeed, *Winningham and Gurgiolo* [1982] have observed that the field-aligned electric potential difference of the polar wind varied as the solar zenith angle. Because the solar zenith angle is

related to the photoionization rate, which directly contributes to the local ionospheric photoelectron density [*Jasperse*, 1981], we expect this density to be an important factor in the polar wind dynamics, despite its relatively small value compared to that of the thermal electrons.

The polar wind dynamics is primarily dictated by the environment in the source region — the ionosphere. Factors such as geomagnetic activity (*i.e.* the geomagnetic field) and the magnetic local time (*i.e.* the photoionization rate), prescribe the ionospheric particle distributions, which evolve, giving rise to particle distributions at higher altitudes as the plasma flows upward along the geomagnetic field line. A variation in the ionospheric distributions not only reflects a different source environment, but also should lead to different polar outflow dynamics. Unfortunately, particle distributions possess infinite degrees of freedom (impossible to be represented by a finite number of parameters); to study how the polar wind dynamics varies with the ionospheric distributions, without making further assumptions, is not feasible.

We therefore assign the ionospheric particle distributions to a certain form, characterized by only a few parameters, and study how the polar dynamics varies with the boundary parametric values. We would like to point out that the polar wind dynamics exhibits a complex inter-relationship between all the effects that are present in the plasma outflow. Therefore, it may not be easy to attribute certain changes in a polar wind quantity to a single factor, such as the photoelectron density. Indeed, as we will show later, some physical quantities are governed by competing effects in the polar wind. Changes in the polar wind photoelectron density, for example, may enhance or diminish these competing effects to different extents, leading to the relative importance of one effect over the other. For this reason, it is necessary to investigate the overall impact of a single factor on the polar wind dynamics based on a self-consistent model.

The polar wind parametric studies in the subsequent sections are based on the self-consistent hybrid model introduced in Chapter 3. The simulation altitudes for these studies range from 500 km to 2 R_E. In the kinetic calculations, initial distributions are introduced at the lower boundary for H^+, O^+ and photoelectrons. For the

ions, they are the upper-half portion of the distribution function in Eq. (2.21), whose shape is essentially characterized by only one parameter, the temperature T_*. (The other parameter, n_0, is determined by the density normalization in the fluid calculation.) The shape of the initial photoelectron distribution function is kept invariant throughout the studies (see the next section for discussion), and is the same as that used in Section 3.2, (*i.e.* $T_* = 21.6$ eV, energy cutoffs at 2 and 62 eV). Similar to the ions, the density parameter for photoelectrons is normalized in the fluid calculation.

Boundary conditions for the fluid calculations are also imposed at the lower simulation end. The boundary conditions for the ion densities, n_h and n_o, provide the normalization constants for the H^+ and O^+ distributions, respectively. The photoelectron distribution, on the other hand, is normalized by an imposed ratio of photoelectron to thermal electron densities (n_s/n_e) at the boundary. The thermal electron distribution is assumed to be a drifting Maxwellian, which is characterized by three parameters — n_e, u_e and T_e. However, with the quasi-neutral and current-free constraints, only a boundary condition for T_e is required for the thermal electron population.

4.1 Photoelectron Effect

Let us first look at the effect of photoelectrons on the polar wind. The ionospheric photoelectron distribution is governed by the photoionization spectrum: The amplitude of the spectrum affects the photoelectron density, and its shape determines the shape of the photoelectron distribution. The amplitude of the photoionization spectrum depends on the photoionization rates, which vary with the solar zenith angle, and thus also with the magnetic local time. The shape of the photoionization spectrum, on the other hand, varies with the relative abundance of all the molecules and ions in the ionosphere. As the relative molecule and ion abundance is beyond the scope of this thesis, we shall use an invariant shape for the initial photoelectron distribution throughout the studies. To study the effect of photoelectrons, we generate polar wind solutions with different boundary conditions for the relative photoelectron

Parameters at 500 km altitude

Case	(a)	(b)	(c)	(d)
n_s/n_e	0	5×10^{-4}	1×10^{-3}	1.5×10^{-3}
Common parameters				
n_o (m^{-3})	4.0×10^{10}			
n_h (m^{-3})	1.5×10^{9}			
T_{o*} (eV)	2.2			
T_{h*} (eV)	1.0			
T_e (°K)	3000			

Table 4.1: Boundary conditions for the four cases with different relative photoelectron density.

density while keeping other boundary conditions the same. Specifically, the following photoelectron to thermal electron density ratio n_s/n_e are imposed at the lower boundary for different cases: (a) 0; (b) 5.0×10^{-4}; (c) 1.0×10^{-3}; (d) 1.5×10^{-3}. These values and the other parameters used in the four cases considered in this study are summarized in Table 4.1.

The profiles n_s/n_e for these four cases are shown in Fig. 4-1. Notice that in Case (a), the density ratio is identically zero because of the absence of photoelectrons. In other cases, the photoelectron densities remain small compared to those of the thermal electrons throughout the simulation range. The test-particle approach for photoelectrons is thus justifiable for these solutions. Figure 4-2 shows that the relative photoelectron density can significantly affect the self-consistent electric potential difference, in that a higher relative photoelectron density leads to a larger potential difference. Because the photoelectrons are suprathermal particles, they will skew the electron distribution, giving rise to a higher electron energy flux, thereby increasing the ambipolar potential difference and the resulting electric field.

A higher relative photoelectron density also leads to a higher electron temperature in the low-altitude collisional regime, as Fig. 4-3 indicates. The upward temperature gradient is related to collisional heating of the thermal electron population. In Case (a) where photoelectrons are absent, thermal electrons are heated through their collisions with the ions. When photoelectrons are present, the heating becomes more important as energy is transferred to the thermal electrons also through collisions

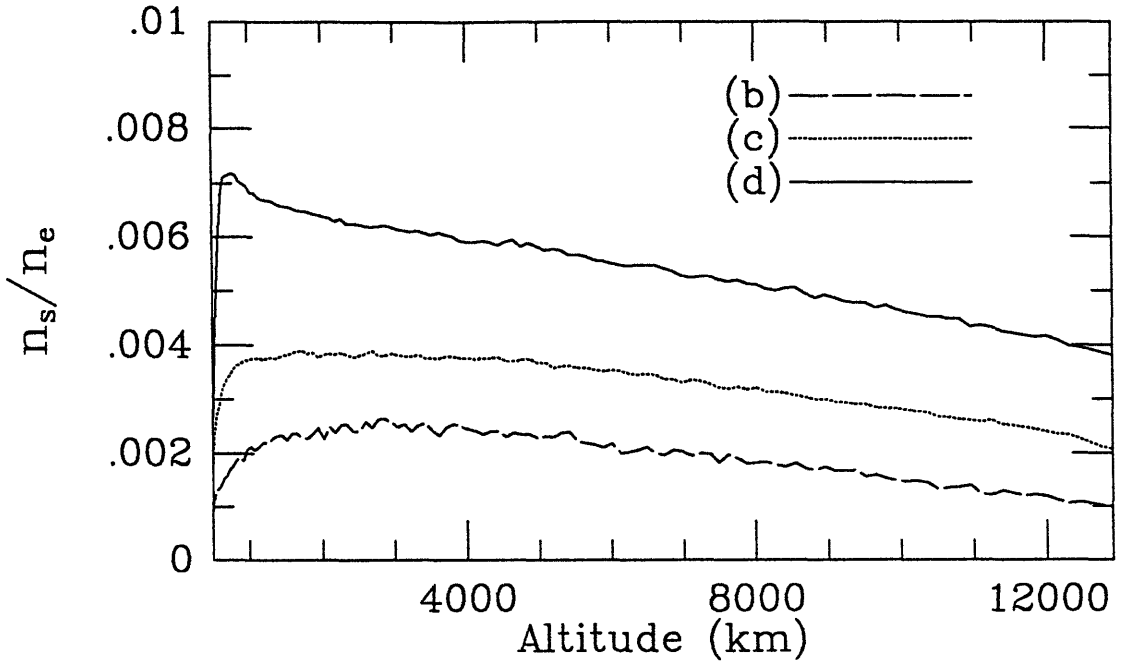

Figure 4-1: Profiles of relative photoelectron density. The labels correspond to the cases listed in Table 4.1.

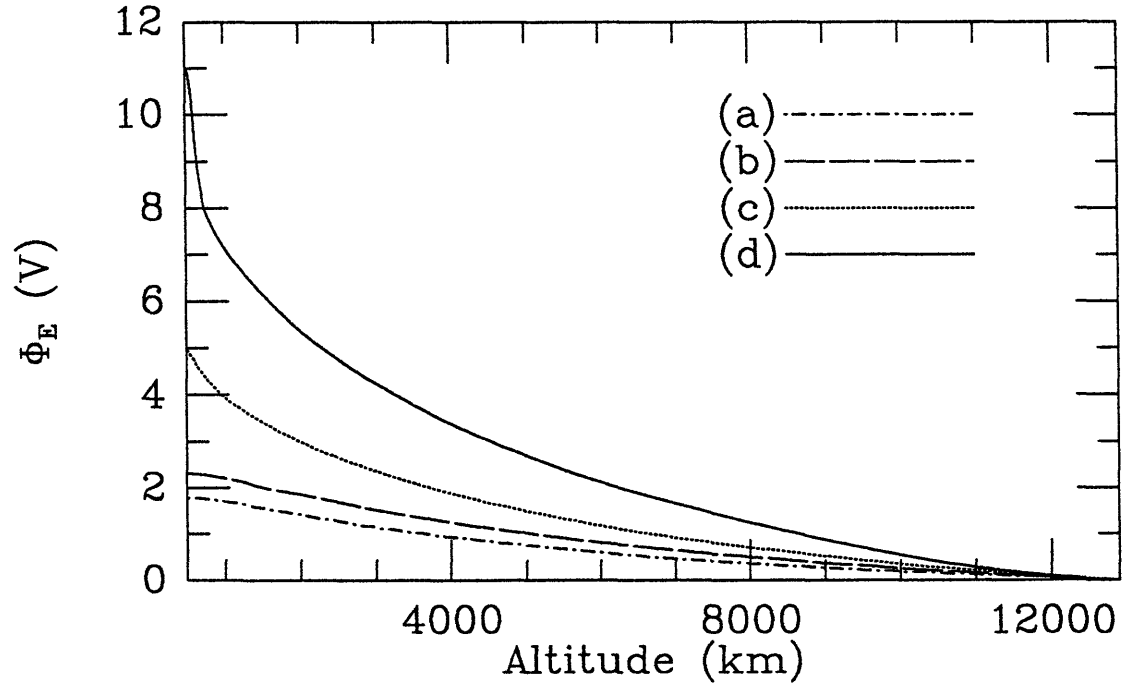

Figure 4-2: Profiles of the self-consistent ambipolar electric potential. The labels correspond to the cases listed in Table 4.1.

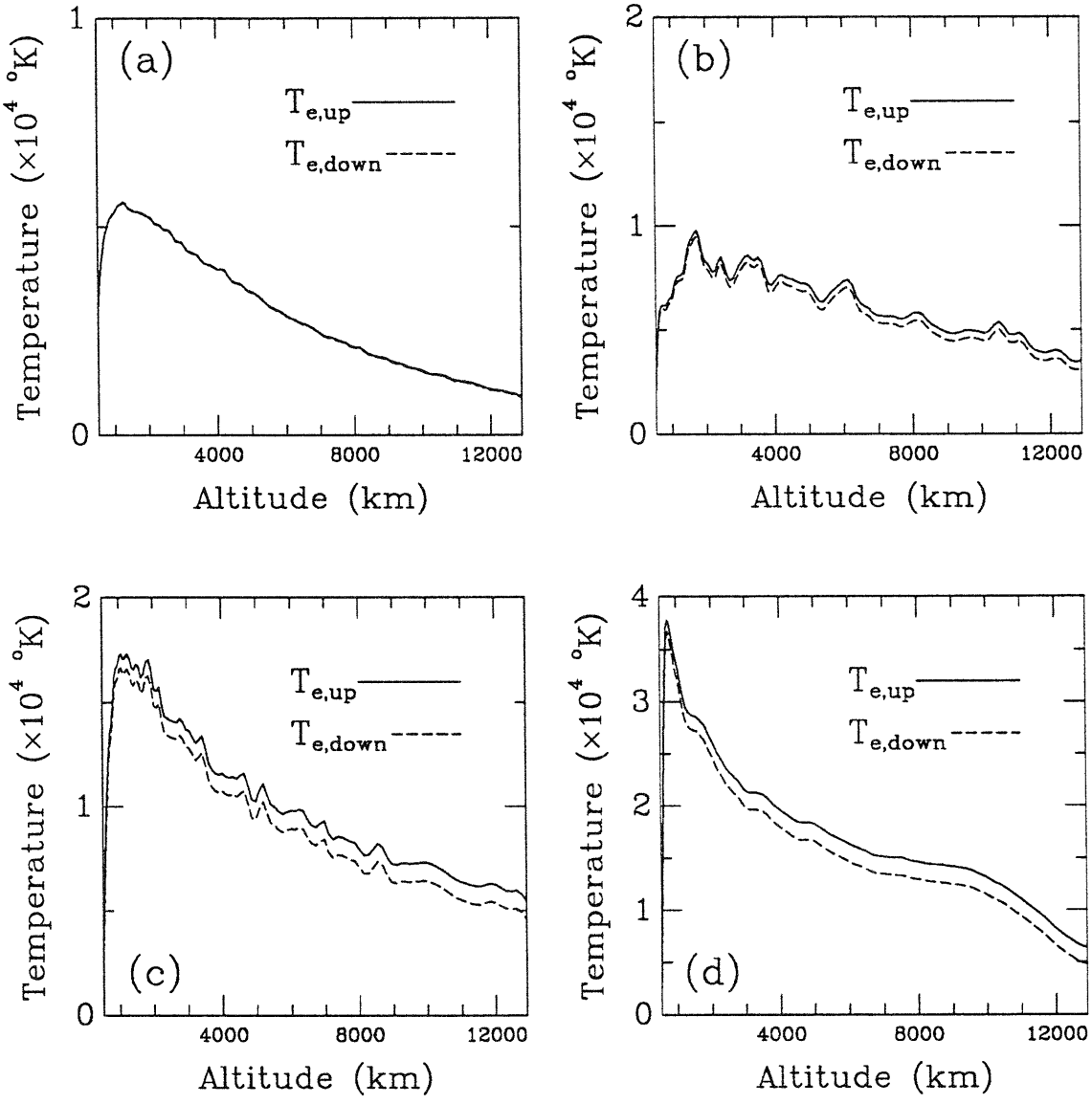

Figure 4-3: Parallel temperature profiles for the upwardly and downwardly moving electron population. The labels correspond to the cases listed in Table 4.1.

with the photoelectrons. As the relative photoelectron density increases, the source of energy provided by the suprathermal population becomes larger, and collisional heating leads to a steeper electron temperature gradient. Because every effect in the polar wind is related due to self-consistency of the dynamics, one may also associate this electron temperature with the electric potential difference, where the two are related in Eq. (3.2) and (3.3) in terms of a balance between competing effects — thermal pressure pushing the electrons outward and electric field pulling them back.

The impact of the relative photoelectron density on the total electron heat flux, $Q_{e,total}$, (*i.e.* the heat flux carried by the combined population of thermal and suprathermal electrons) can be seen in Fig. 4-4. In the model, because the thermal electron population is assumed to be a Maxwellian, the electron heat flux is carried only by the suprathermal population.[1] In the absence of photoelectrons (Case (a)), $Q_{e,total}$ is thus identically zero. Because $Q_{e,total}$ is directly related to the number density of the population, it is in fact more correlated with the actual photoelectron density n_s, as shown in Fig. 4-5, than with the density ratio n_s/n_e. Nevertheless, the density ratio at the boundary can influence the photoelectron density, not only directly, but also in a non-trivial way through the ambipolar field. Let us consider the transition from Case (a) through (d) as we increase the relative photoelectron density. Because the density ratio n_s/n_e is small, as we vary its boundary value, the thermal electron density at the boundary only changes by a negligible amount. Hence, a higher relative photoelectron density means more suprathermal electrons contribute to the tail of the total distribution. Because the upwardly directed electron heat flux is a result of the escape of these energetic particles, more photoelectrons in the distribution, in general, lead to a larger $Q_{e,total}$ (see Case (a) through (c)). However, a higher relative photoelectron density, as we have seen, also leads to a larger ambipolar electric field. This field provides an energy barrier for the escaping electrons, reflecting those with relatively low energies. When the electric field becomes sufficiently large, as a result of the increases in relative photoelectron density, it is able to reflect electrons with energies well in the suprathermal range, significantly weakening the tail

[1] Validity of this assumption is discussed in Section 4.1.1

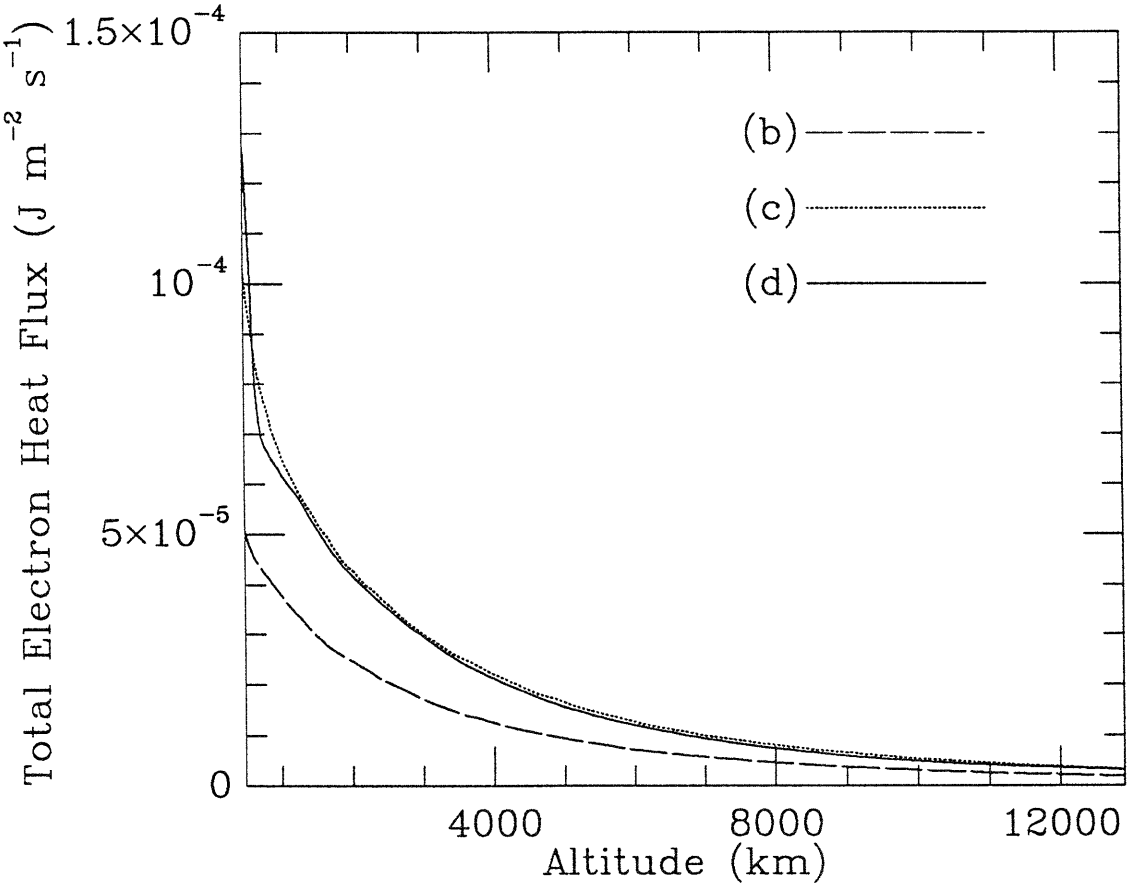

Figure 4-4: Total heat flux profiles for the total electron population. The labels correspond to the cases listed in Table 4.1.

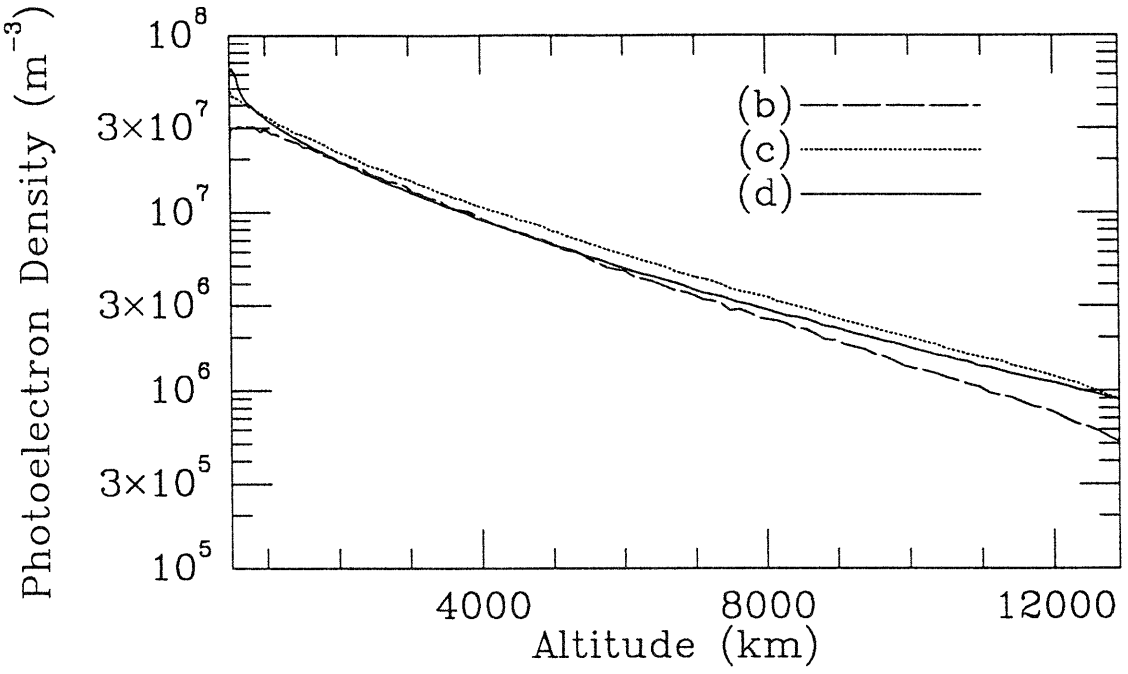

Figure 4-5: Profiles of the photoelectron density. The labels correspond to the cases listed in Table 4.1.

Case	n_s/n_e	Number flux at 10000 km ($m^{-2}s^{-1}$)	
		H^+	O^+
(a)	0	9.49×10^{10}	3.25×10^{11}
(b)	5×10^{-4}	1.24×10^{11}	1.82×10^{12}
(c)	1×10^{-3}	2.35×10^{11}	3.20×10^{12}
(d)	1.5×10^{-3}	2.61×10^{11}	3.19×10^{12}

Table 4.2: A list of the density ratio n_s/n_e at 500 km altitude, and the ion number fluxes for the four cases, whose boundary conditions are shown in Table 4.1.

portion of the distribution, and lowering $Q_{e,total}$. The significance of this competing effect due to the electric field is evident, as we compare Case (c) and (d) in terms of photoelectron density and total electron heat flux.

Through its impact on the polar wind ambipolar field, the relative photoelectron density has a significant effect not only on the electron population, but also on the dynamics of the ion outflows. For example, as shown in Table 4.2, the ion number fluxes generally increase with the relative photoelectron density. This correlation is mainly due to the magnitude of the self-consistent ambipolar field: the higher the relative photoelectron density, the larger the ambipolar field, and consequently, due

to acceleration by the field, the greater the number of escaping ions contributing to the number fluxes at high altitudes.

Intuitively, this ion acceleration by the ambipolar field should increase their densities at high altitudes. However, the acceleration itself also creates a competing effect that would lower the ion density, due to conservation of the species. Because mass conservation must hold for every species in the classical polar wind, the ions, in particular, have to satisfy Eq. (2.1). In principle, a larger electric field tends to accelerate the ions to higher outflow velocities, thereby reducing the densities to a larger extent. Comparison of the resulting ion density profiles for our four cases, as shown in Fig. 4-6, provides an indication of the competing effects due to acceleration by the self-consistent electric field. In general, both H^+ and O^+ densities increase with the relative of photoelectrons, provided that the self-consistent electric field is sufficiently low (compare Case (a) and (b)). However, when the electric field is sufficiently large, the trend is reversed (compare Case (b), (c) and (d)) for the reason discussed above.

Figures 4-7 and 4-8 show respectively the resulting outflow velocity profiles for O^+ and H^+ in the four cases. For O^+, its velocity variation with the relative photoelectron density is rather simple: the velocity increases with the boundary density ratio n_s/n_e, due to the magnitude of the self-consistent ambipolar field. However, for H^+, the variation of its velocity is more complicated. As we see from Fig. 4-8, Case (b) generally has a smaller H^+ outflow velocity than Case (a), contrary to intuition considering that the self-consistent electric field is larger in (b). In fact, this piece of information provides an excellent example demonstrating the complexity of the global kinetic collisional dynamics of the polar wind — the counter-intuitive result is due to Coulomb collisions between the H^+ and O^+ ions.

Note that in our results (and Akebono observations [*Abe et al.*, 1993b]), H^+ is the minority ion species; an H^+ ion will collide mostly with O^+. Because O^+ has a smaller outflow velocity than H^+, the Coulomb interaction between the two species will slow down the latter. The significance of this slowing-down effect on H^+ depends on the efficiency of the collisions. One way to describe this efficiency is to compare

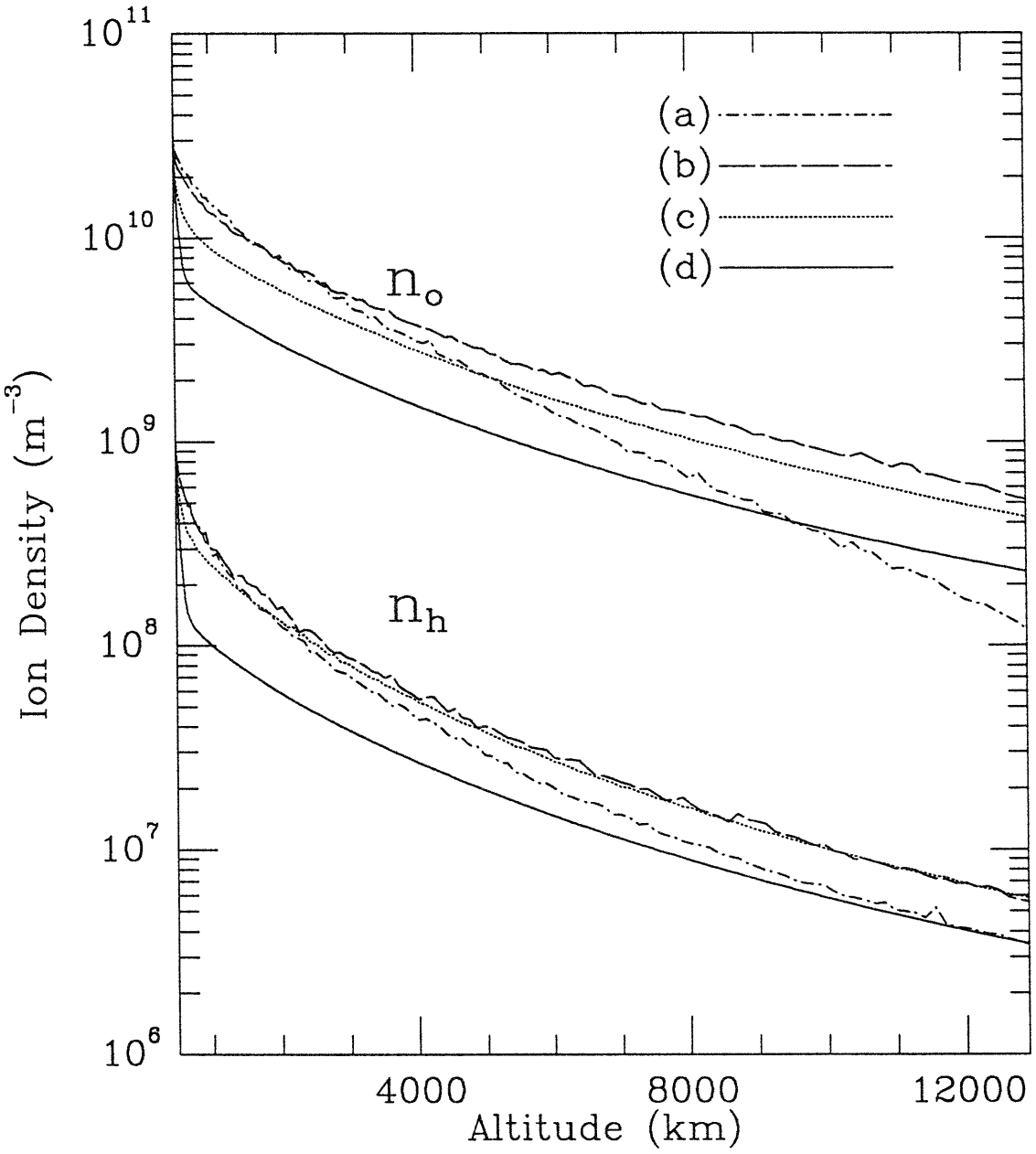

Figure 4-6: Profiles of the O^+ and H^+ densities. The labels correspond to the cases listed in Table 4.1.

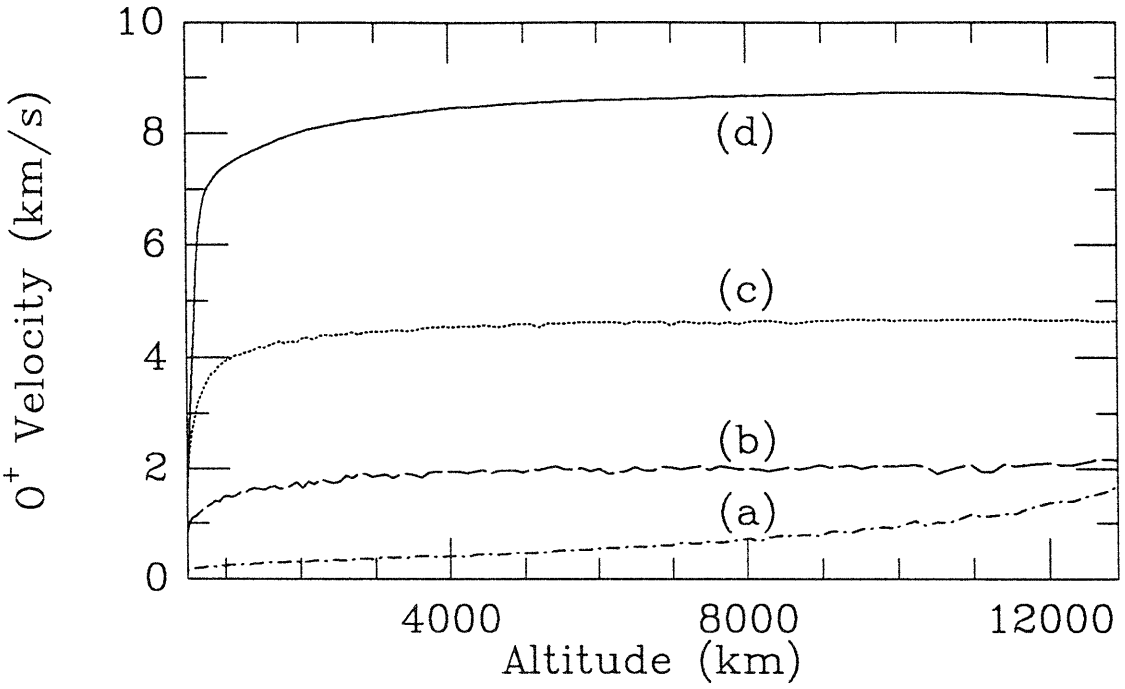

Figure 4-7: Profiles of the O^+ outflow velocity. The labels correspond to the cases listed in Table 4.1.

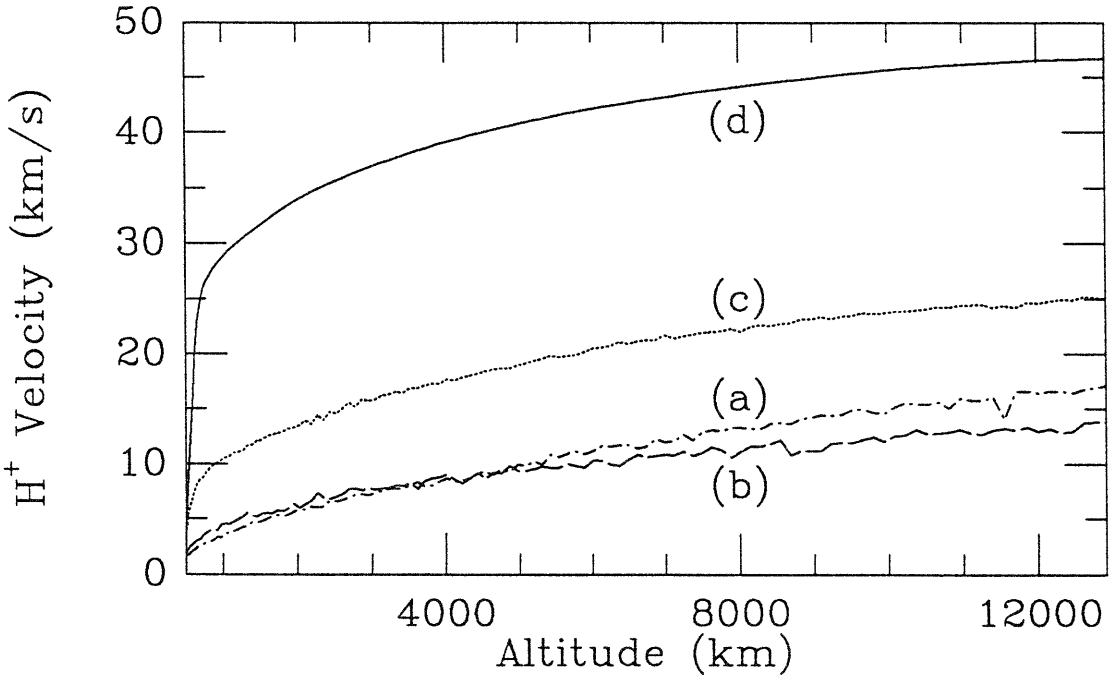

Figure 4-8: Profiles of the H^+ outflow velocity. The labels correspond to the cases listed in Table 4.1.

Case	(a)	(b)	(c)	(d)
τ_{transit} (s)	256.7	208.6	200.0	91.78
$\tau_{\text{coll,s}}$ (s)	84.53	31.40	302.3	16605
$\tau_{\text{coll,}\parallel}$ (s)	1049	381.8	12909.9	2.020×10^6
$\tau_{\text{coll,}\perp}$ (s)	93.81	34.88	325.2	7027
$\tau_{\text{transit}}/\tau_{\text{coll,s}}$	3.037	6.643	0.662	0.014
$\tau_{\text{transit}}/\tau_{\text{coll,}\parallel}$	0.245	0.546	0.015	4.543×10^{-5}
$\tau_{\text{transit}}/\tau_{\text{coll,}\perp}$	2.736	5.981	0.615	0.013

Table 4.3: H^+ time scales at 5000 km altitude

the local time scales of the collisional process with the local H^+ transit time

$$\tau_{\text{transit}} = L/u_h,$$

where L is the local scale length. Note that τ_{transit} characterizes the time scale where a typical H^+ ion stays in the local region. For the present purpose, we are interested in comparing τ_{transit} with the collisional time τ_{coll} that corresponds to H^+ collisions with O^+, *i.e.*

$$\tau_{\text{coll}} = \nu_{\text{coll}}^{-1},$$

where ν_{coll} represents the collisional frequencies defined in Eq. (2.8 – 2.10). For the case considered, there are three characteristic times: $\tau_{\text{coll,s}}$ for the slowing-down effect, and $\tau_{\text{coll,}\parallel}$ and $\tau_{\text{coll,}\perp}$ for diffusion. Table 4.3 shows these characteristic times for the H^+- O^+ interaction (which is the most significant type of Coulomb collisions for the H^+ species), and τ_{transit} (based on the local O^+ scale length), and the ratio of these time scales, all at 5000 km altitude. Note that in particular, the ratio $\tau_{\text{transit}}/\tau_{\text{coll,s}}$ is an indicator for the significance of the slowing-down effect on H^+ due to collisions with O^+— the larger the ratio, the more an H^+ ion is slowed down. It is clear that this ratio is larger in Case (b) than in (a), suggesting that H^+ ions are subjected to the slowing-down effect to a larger extent in (b), resulting in an overall smaller outflow velocity. Although we have only showed the time scales at one local point, these ratios, for our comparison purpose, sufficiently characterize the role of collisions in our polar wind solutions.

Collisions also play a significant role in shaping the polar wind ion temperature profiles. In particular, collisions lead to velocity diffusion in the distribution of the species, which tend to increase the temperatures as the particles move along the field lines. Because ions in the polar wind are predominantly outgoing, we would expect diffusion to contribute to a temperature which increases with altitude. Figure 4-9 shows the resulting H^+ and O^+ temperatures for our polar wind cases with different relative photoelectron densities at the boundary.[2] The collisional impact is most noticeable when we look at the profiles for H^+ parallel temperature $T_{h||}$. In particular, $T_{h||}$ in Case (d) is much lower than in the other cases. One of the reasons for that is the relatively collisionless nature of the H^+ outflow, or in other words, the relatively low H^+ diffusion rates for the case. (Note from Eq. (2.9) and (2.10) that the diffusion rates are proportional to the density of the field species, and also that the densities n_o, n_h, and $n_e \approx n_o + n_h$ are generally lower in Case (d) than in the other cases.) Of course, the overall velocity diffusion for a given species results from collisions with each particle species, including the species itself whose diffusion is described. However, in order to demonstrate that Case (d) is indeed the least collisional case for H^+, we will highlight only its collisions with the O^+, which is the major ion species in both the polar wind observations and our solutions. These H^+-O^+interactions, whose collisional times at 5000 km altitude are shown and compared with the transit times in Table 4.3, are sufficient to characterize the full H^+ collisions for our present purpose. As the table indicates, H^+ ions in Case (d) have a small ratio of $\tau_{\text{transit}}/\tau_{\text{coll},\perp}$, and an even much smaller ratio of $\tau_{\text{transit}}/\tau_{\text{coll},||}$.[3] Hence, velocity diffusion due to collisions, particularly those in the field-aligned direction, are rather insignificant for this case. In comparison, collisional effects on the H^+ ions are more important in the other cases, and diffusion may dominate in the complex interplay among other polar wind

[2]Because the calculation results have not been smoothed, wiggles are still present in the lines, reflecting the statistical nature of the Monte Carlo technique. These wiggles, however, do not affect the general trend of the results.

[3]Note that the parallel and perpendicular directions here are relative to the vectorial difference between the velocities of individual H^+ ions and the outflow velocity of the O^+ species. Because the outflow velocities of the two ion species are very different, the vectorial difference that we refer to is almost field-aligned.

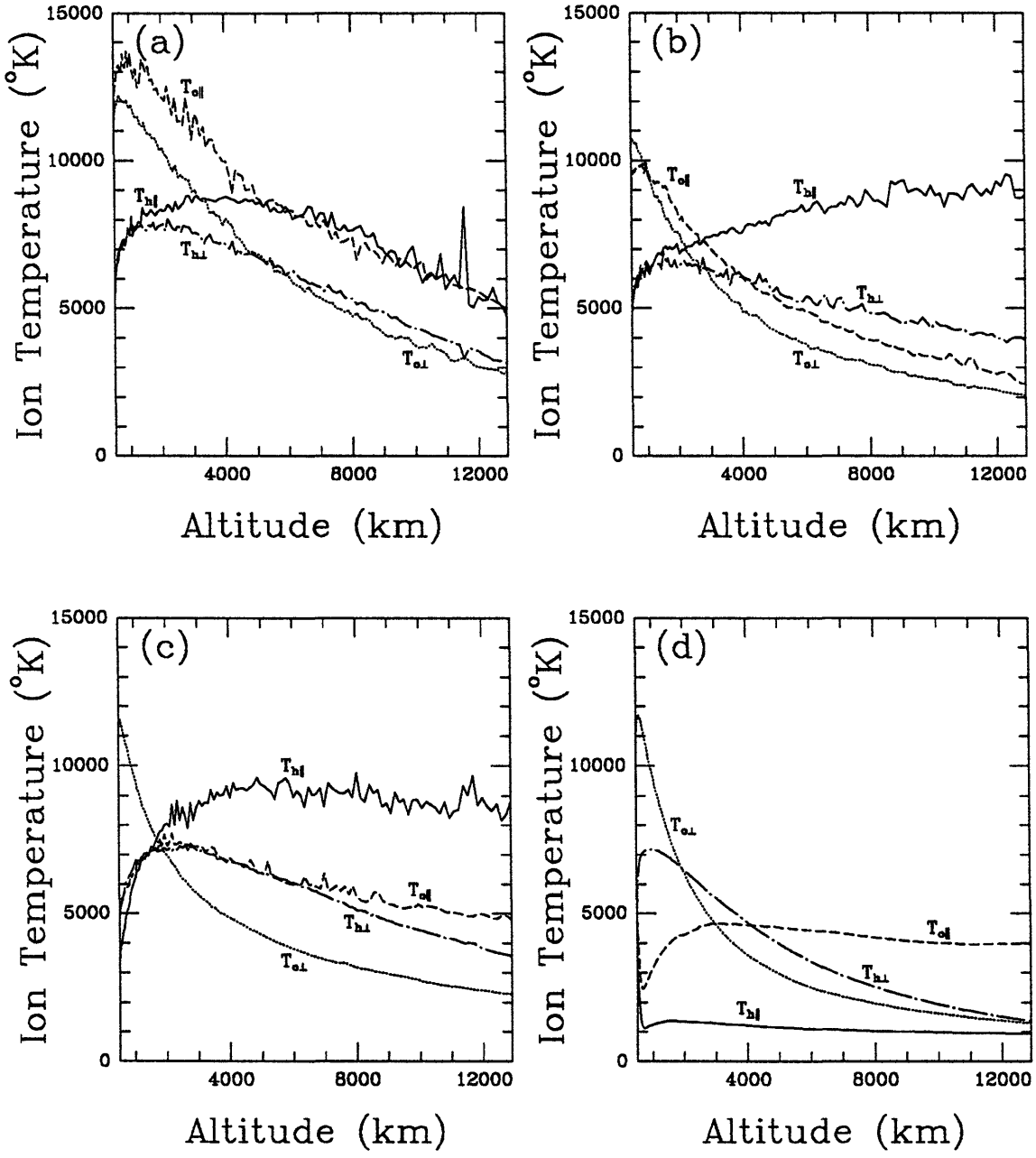

Figure 4-9: Profiles of the ion temperatures. The labels correspond to the cases listed in Table 4.1.

effects, giving rise to an upward gradient in $T_{h\|}$ at some altitudes. Similarly, the upward gradients in $T_{h\perp}$ at low altitudes are also due to the fact that diffusion is dominant.

In contrast to the diffusion effect which tends to create an upward gradient in the ion temperature, acceleration of the ions by the field-aligned electric field tends to do the opposite, and is largely responsible for the downward gradient of $T_{h\|}$ and $T_{o\|}$ at low altitudes in Case (d). This effect arises because of the global steady-state nature of the classical polar wind. To understand this effect, let us consider particles of the same species but with different velocities flowing out from altitude s_1 to s_2 while being accelerated by a field-aligned electric field. For a particle with a high outflow velocity, the time it takes to cover the altitude range is short. Because of the short duration, the momentum it receives from the electric field is small. By the same token, the momentum transfer to a particle of small outflow velocity will be large, although the particle will reach s_2 at a later time. However, in steady-state, the arrival time is not an issue. An observer of the steady-state flow simply sees that the outflow velocity differential among particles reduces as they move upward. Reduction of the outflow velocity differential, of course, means a decrease in the parallel temperature of the species. The impact on the temperature due to this velocity-differential momentum transfer depends on the strength of the electric field: the higher the electric field, the more significant its impact. Because the electric field in our polar wind solutions (the slope of the potential profile in Fig. 4-2) is generally larger at low altitude, and in Case (d), its effect on the temperature is most noticeable there, where it dominates the diffusion effect, leading to decreasing parallel temperatures for both ion species.

There are also other effects in the polar wind that may contribute to the resulting ion temperature profiles. These effects, like diffusion and velocity-differential momentum transfer, modify the distributions of the species as the particles move along the field line. The temperatures at high altitudes are thus the integrated results of all the effects that govern the evolution of the particle distributions. A well-known effect is the mirror force that converts the particles' energies transverse to the field into the parallel direction as they travel upward. As the collisional effects weaken with

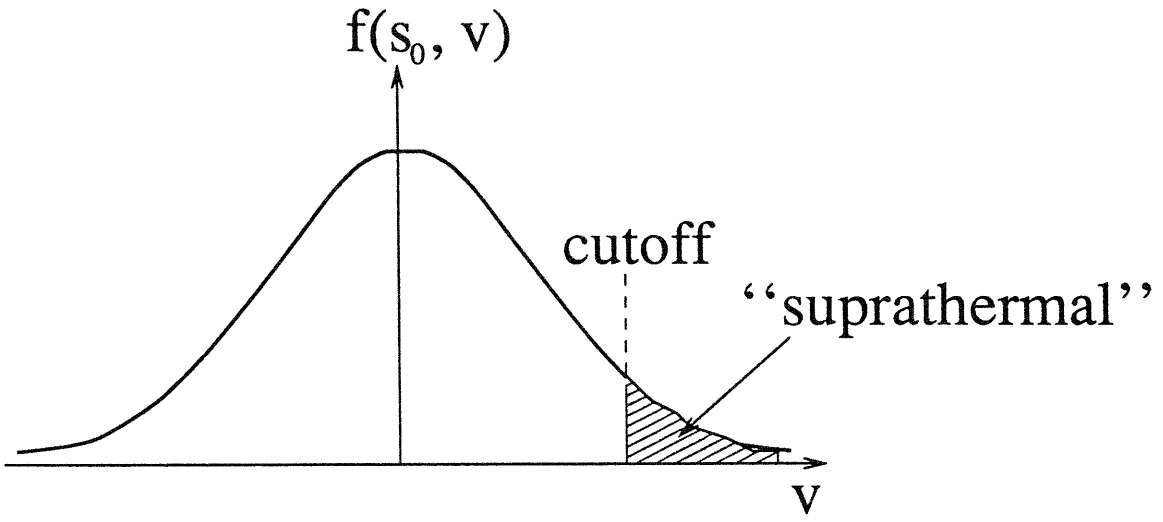

Figure 4-10: An illustration of the "night-time" regime where a high-energy portion of the thermal electrons at the lower boundary s_0 are relabeled as "suprathermal" in the test-particle calculations.

altitude due to the density decrease, the mirror effect dominates the perpendicular temperature profiles at high altitudes, leading to a downward gradient in $T_{h\perp}$ and $T_{o\perp}$ in all the cases considered.

4.1.1 Night-time Solution

As mentioned, in the self-consistent hybrid model, the electron heat flux is entirely carried by the photoelectrons as the thermal electrons are assumed to be a drifting Maxwellian distribution. This assumption is certainly valid for the daytime polar wind calculations as we have shown in Chapter 2 that the electron heat flux is primarily carried by the photoelectron population. For the night-time polar wind (Case (a)), where photoelectrons are absent, this assumption may need further justification.

To address this issue, we shall show that the thermal electrons indeed carry a minimal amount of heat flux. Under night-time conditions, the role of the photoelectrons will be fulfilled by the suprathermal electrons in the tail portion of the distribution function; these suprathermal electrons will carry the bulk of the electron heat flux, as described by *Scudder and Olbert* [1979]. We have calculated the heat flux contribution of these "suprathermal" electrons (defined by their low-energy cutoff, see

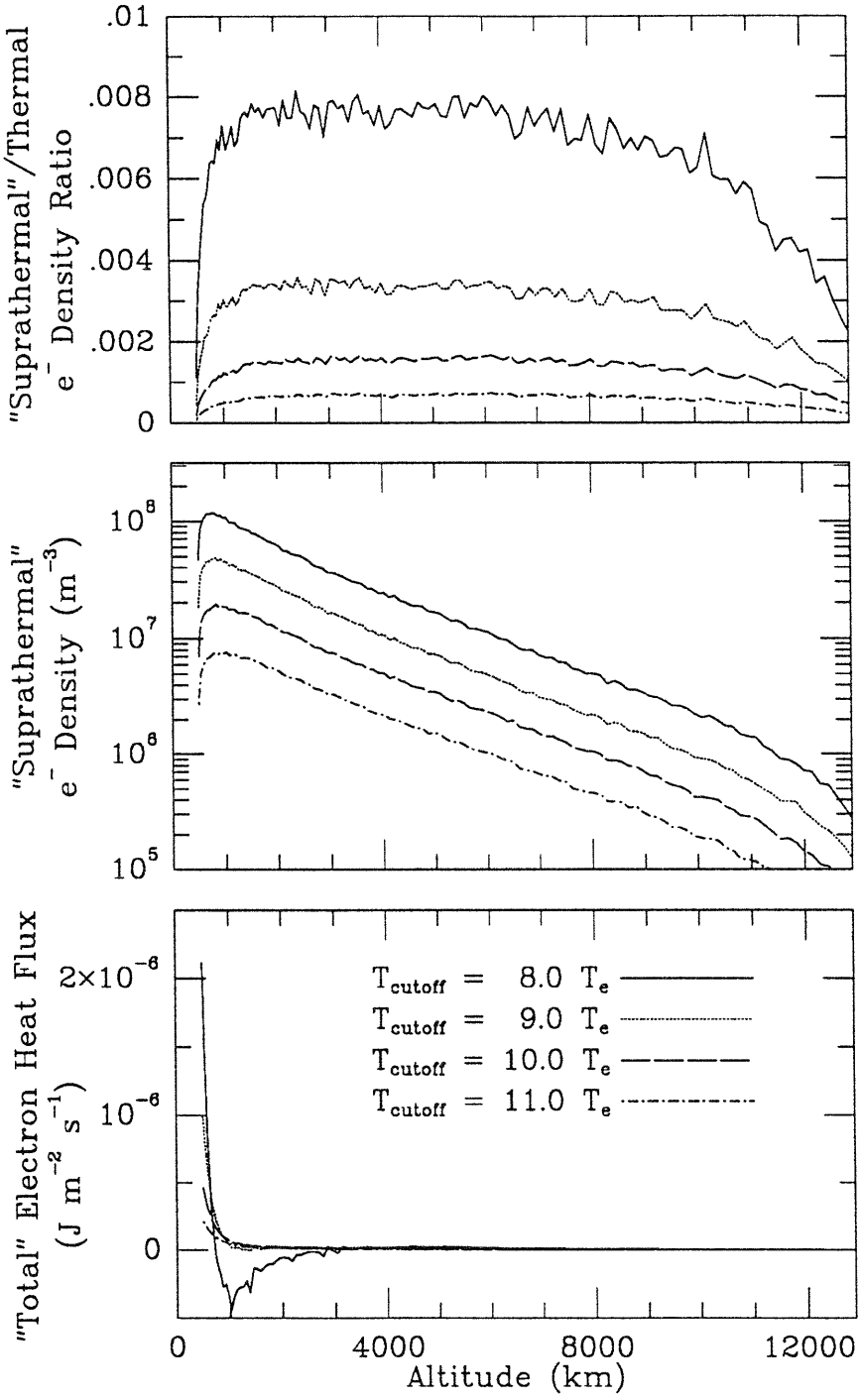

Figure 4-11: Results of the test-particle calculations in which the background is the night-time polar wind solution (Case (a) of this section). Top panel: ratio of "suprathermal" (test-particle) to thermal electron densities; middle panel: "suprathermal" electron density; bottom panel: "Total" electron heat flux for the "whole" electron population.

Fig. 4-10) by performing global kinetic collisional test-particle calculations using the night-time polar wind solution (Case (a)) as the background. Figure 4-11 shows the results of these calculations for different suprathermal energy cutoffs. The boundary values of test-particle to background density ratio, shown in the top panel, are determined assuming a Maxwellian background. The suprathermal densities, determined from the test-particle calculations, are shown in the middle panel. The bottom panel shows the total heat flux, which is obtained by combining the suprathermal test particles with the background (assumed to be Maxwellian). The "total" heat fluxes here are much smaller than those with photoelectrons present (*c.f.* Fig. 4-4), even though we use energy cutoffs low enough to yield a higher "suprathermal" electron density than the corresponding daytime photoelectron density (*c.f.* Fig. 4-5). Moreover, the heat flux carried by the suprathermal tail of the thermal electron distribution diminishes very rapidly and almost vanishes as the particles move to higher altitudes. Our calculation results therefore indicate that the heat flux carried by the thermal electrons is indeed negligible, especially at high altitudes, justifying the approximation used to describe the thermal electrons in the self-consistent hybrid model.

4.2 Effect of O^+ Temperature

Because of self-consistency, the dynamics of the polar wind outflow, to some extent, should depend on all of its particle components and the electric field. Besides the photoelectron density, other polar wind quantities may also be important in the flow dynamics itself. For example, as the polar wind solution comparison in the previous section suggests, the ion densities, temperatures, and flow velocities may determine the impact of collisions, which may in turn modify the quantities of the species themselves at a higher altitude as the plasma expands. *Abe et al.* [1993b] have estimated the H^+ and O^+ ion densities, temperatures and outflow velocities at high altitude based on data from the Akebono satellite. However, because the data have not been corrected for the spacecraft potential and the particle drift velocities perpendicular to the spin plane of the instrument, the estimates they provide are only the lower limits

Parameters at 500 km altitude

Case	(a)	(b)	(c)
T_{o*} (eV)	1.0	1.4	2.2
Common parameters			
n_o (m^{-3})	4.0×10^{10}		
n_h (m^{-3})	1.5×10^{9}		
n_s/n_e	7.5×10^{-4}		
T_{h*} (eV)	1.0		
T_e (°K)	3000		

Table 4.4: Boundary conditions for the three cases with different O^+ temperature.

for the densities and upper limits for the temperatures. Because of these experimental uncertainties, a polar wind parametric study based on these physical quantities may be useful, in that it may indicate to what extent these quantities are relevant to the overall polar wind dynamics.

In this section, we will focus on the temperature of O^+ ions, the major ion species in the polar wind. In other words, we shall compare different polar wind solutions by varying the parameter T_{o*}, while keeping the other parameters constant. The O^+ temperature parameter, T_{o*}, for the different cases are: (a) 1.0 eV; (b) 1.4 eV; (c) 2.2 eV. These values and the other boundary conditions for the three solutions are summarized in Table 4.4. Note that the initial distributions applied at the lower simulation end of the kinetic calculations only consist of the upgoing particle population, while the resulting distributions also take into account the reflected population, and thus have higher energy spreads in the field-aligned direction. In this study, the resulting temperatures $T_{o\|}$ at the lower simulation end for the polar wind solutions (a), (b) and (c) are shown in Table 4.5, and are respectively about 2200, 3100, and 5200 °K.

Figure 4-12 shows the self-consistent electric potential of these polar wind solutions. This figure suggests that the ambipolar electric field in the polar wind can be significantly influenced by the ionospheric O^+ temperature. The overall potential difference in our solutions decreases from 8 to 3 V when the boundary O^+ temperature increases by only about 3000 °K from Case (a) through (c). Because the O^+ ions are more collisional than the photoelectrons, we cannot simply rely on the suprathermal

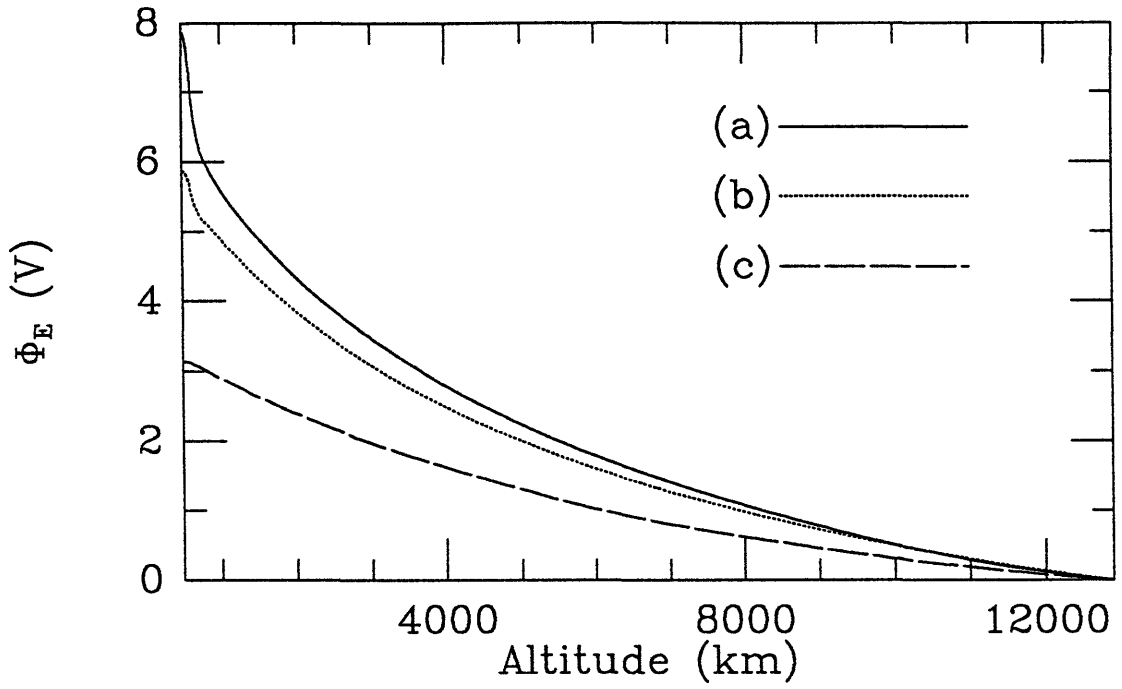

Figure 4-12: Profiles of the self-consistent ambipolar electric potential. The labels correspond to the cases listed in Table 4.4.

scenario invoked for the latter. We also need to consider that the various constituents are tied together by the quasi-neutrality and current-free conditions. In the present case, increasing the ion boundary temperature results, due to our choice of distribution function, in a larger ion flux that would contribute to the current and must be counter-balanced by an enhancement in the total electron flux. This is achieved self-consistently by a reduction in the ambipolar electric field. In fact, this argument applies not only to O^+, but also to the H^+ ions. However, because O^+ is the major ion species in the polar wind, the self-consistent electric field is more sensitive to its low-altitude temperature than that of H^+, as we shall show in Section 4.3.

Similar to the cases in Section 4.1, the electric field in our polar wind solutions here is responsible for driving the ion flux to high altitudes. As Table 4.5 shows, the H^+ number flux at 10000 km altitude decreases from Case (a) through (c), in response to the magnitude of the self-consistent electric potential difference in the solutions. The O^+ number flux, however, demonstrates an opposite trend, decreasing with the magnitude of the electric field. This is simply due to the boundary conditions for the

Case	T_{o*} (eV)	$T_{o\|\|}$ (°K)	$\Delta\Phi_E$ (V)	Number flux at 10000 km ($m^{-2}s^{-1}$)	
				H^+	O^+
(a)	1.0	2209	7.87	2.64×10^{11}	2.05×10^{12}
(b)	1.4	3074	5.87	2.43×10^{11}	2.35×10^{12}
(c)	2.2	5168	3.14	1.91×10^{11}	2.69×10^{12}

Table 4.5: A list of the O^+ temperature parameter T_{o*}, its corresponding parallel temperature at 500 km altitude, the resulting overall self-consistent electric potential difference ($\Delta\Phi_E$) across the simulation range, and the ion number fluxes for the three cases, whose boundary conditions are shown in Table 4.4.

O^+ temperature. As discussed earlier, a higher boundary temperature corresponds to a higher intrinsic number flux. Thus, the variation in the O^+ number flux can be considered a cause for the variation of the electric field, which leads to variation of other polar wind quantities, including the H^+ number flux.

In fact, the self-consistent electric field is essential to the polar wind dynamics. Many polar wind quantities are dictated by the magnitude of the electric field. For example, as shown in Fig. 4-13, the ion densities in polar wind solutions of this study increase, while the resulting self-consistent electric field decreases from (a) through (c). The impact by the electric field on the ion densities has been discussed in Section 4.1. Basically, when the electric field is sufficiently large, its acceleration of the ions will deplete the species locally (a consequence of particle conservation). A larger electric field will accelerate the ions to higher outflow velocities, thus depleting the species more, and resulting in smaller ion densities. The variation trends demonstrated by the H^+ and O^+ outflow velocities (Fig. 4-14 and 4-15 respectively), and the ion densities are all dominated by this effect due to acceleration by the electric field.

On the other hand, the ion temperature profiles in our polar wind solutions, as shown in Fig. 4-16, are governed by a mixture of effects that have been discussed in Section 4.1. Basically, these effects are mainly due to the mirror force, diffusion, and velocity-dependent momentum transfer by the electric field. In particular, diffusion shows a strong dependence on the particle densities, while the impact of velocity-dependent momentum transfer is mainly based on the local value of the self-consistent electric field. Because of the self-consistent responses by the ambipolar field and the

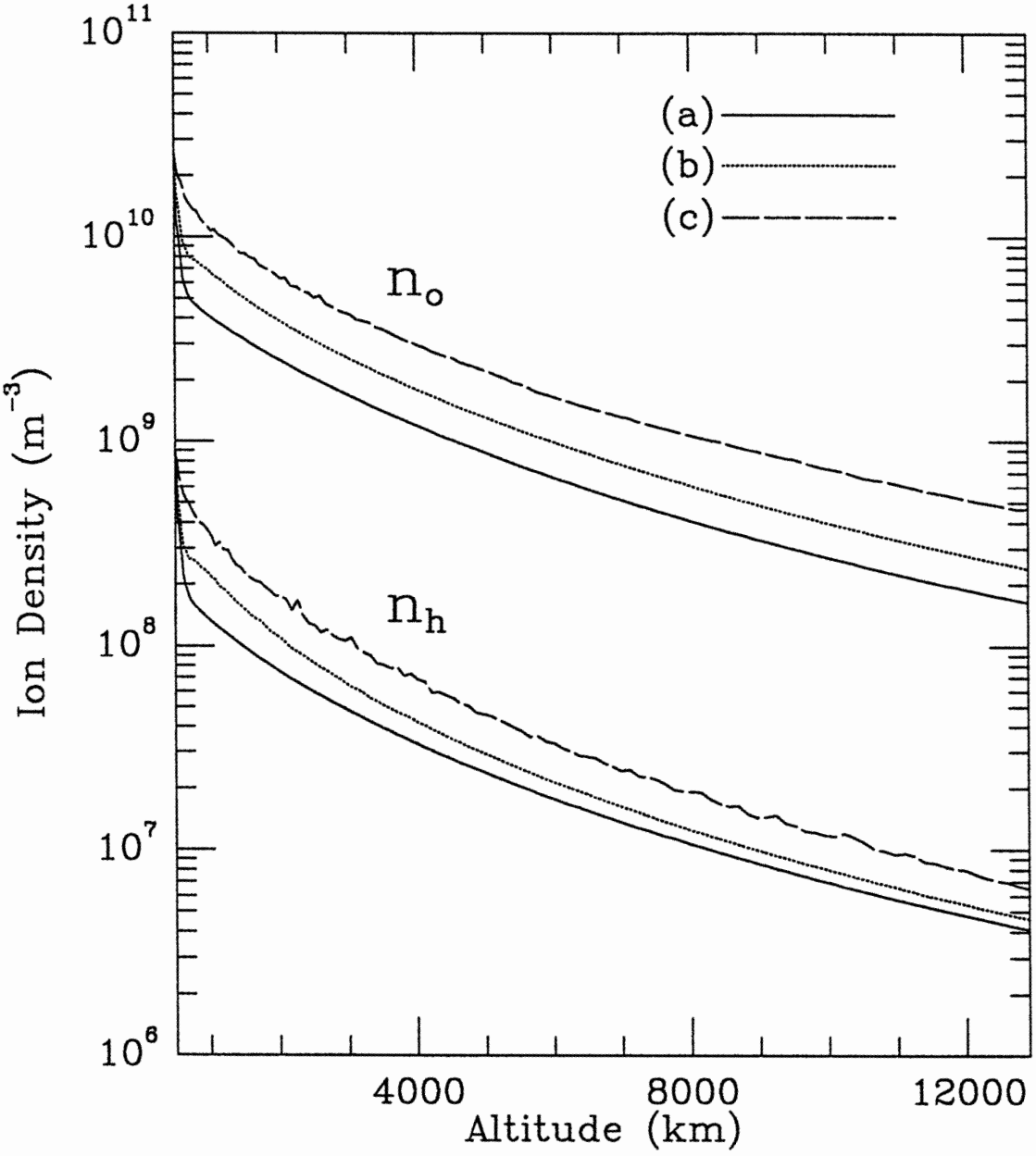

Figure 4-13: Profiles of the O^+ and H^+ densities. The labels correspond to the cases listed in Table 4.4.

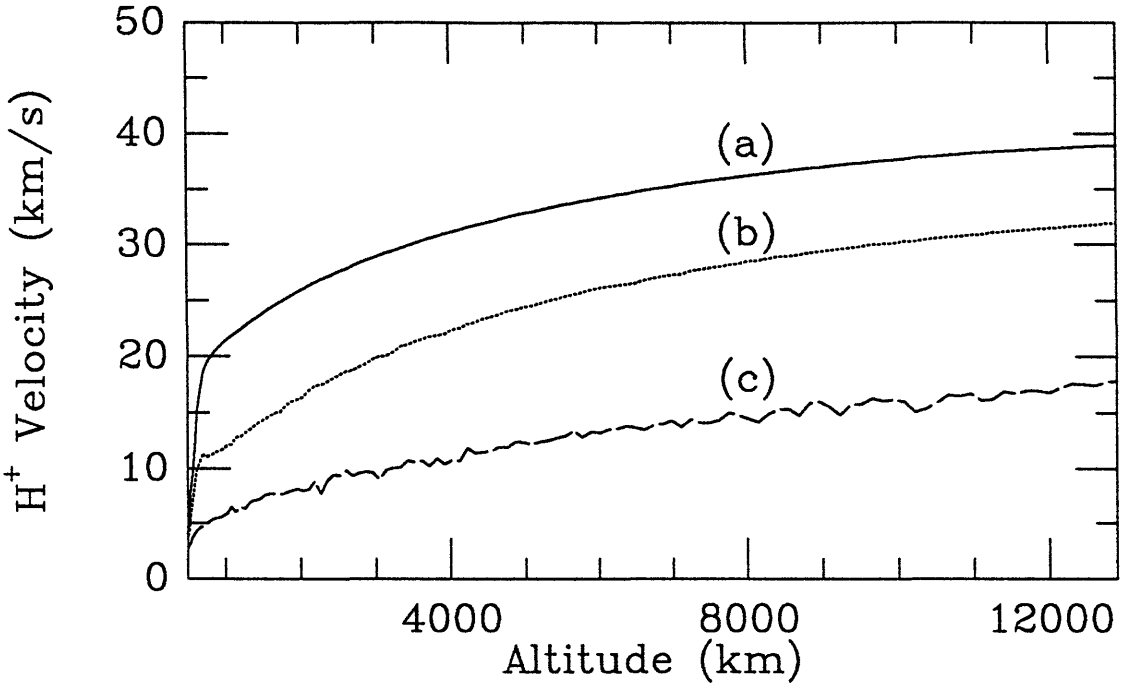

Figure 4-14: Profiles of the H^+ outflow velocity. The labels correspond to the cases listed in Table 4.4.

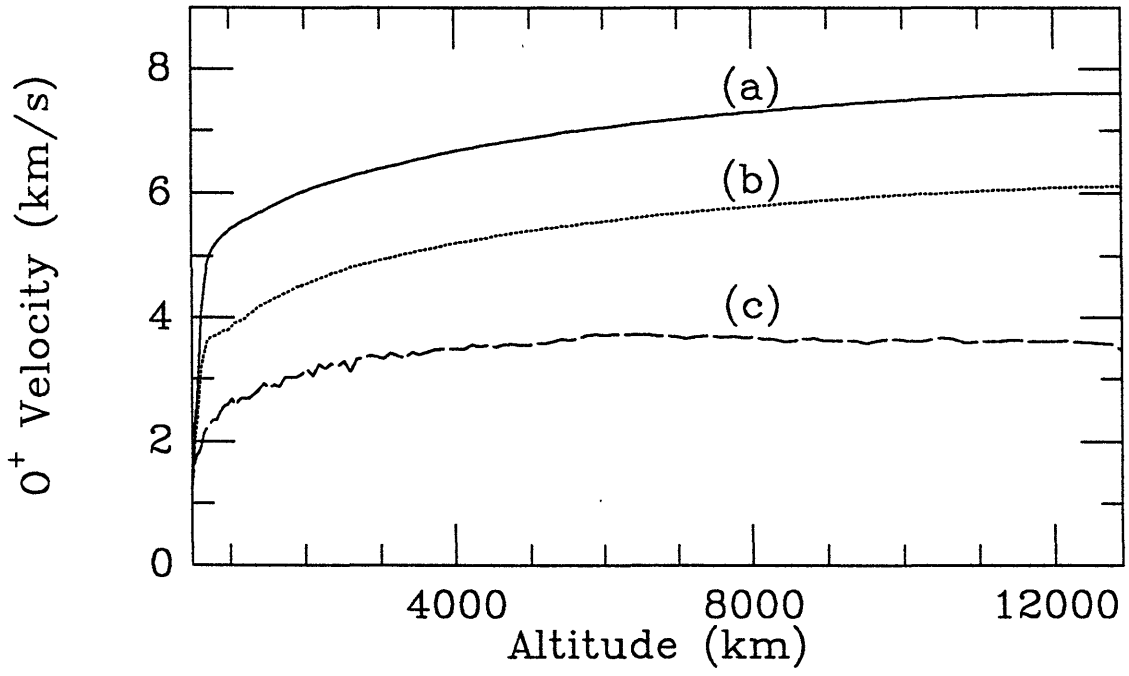

Figure 4-15: Profiles of the O^+ outflow velocity. The labels correspond to the cases listed in Table 4.4.

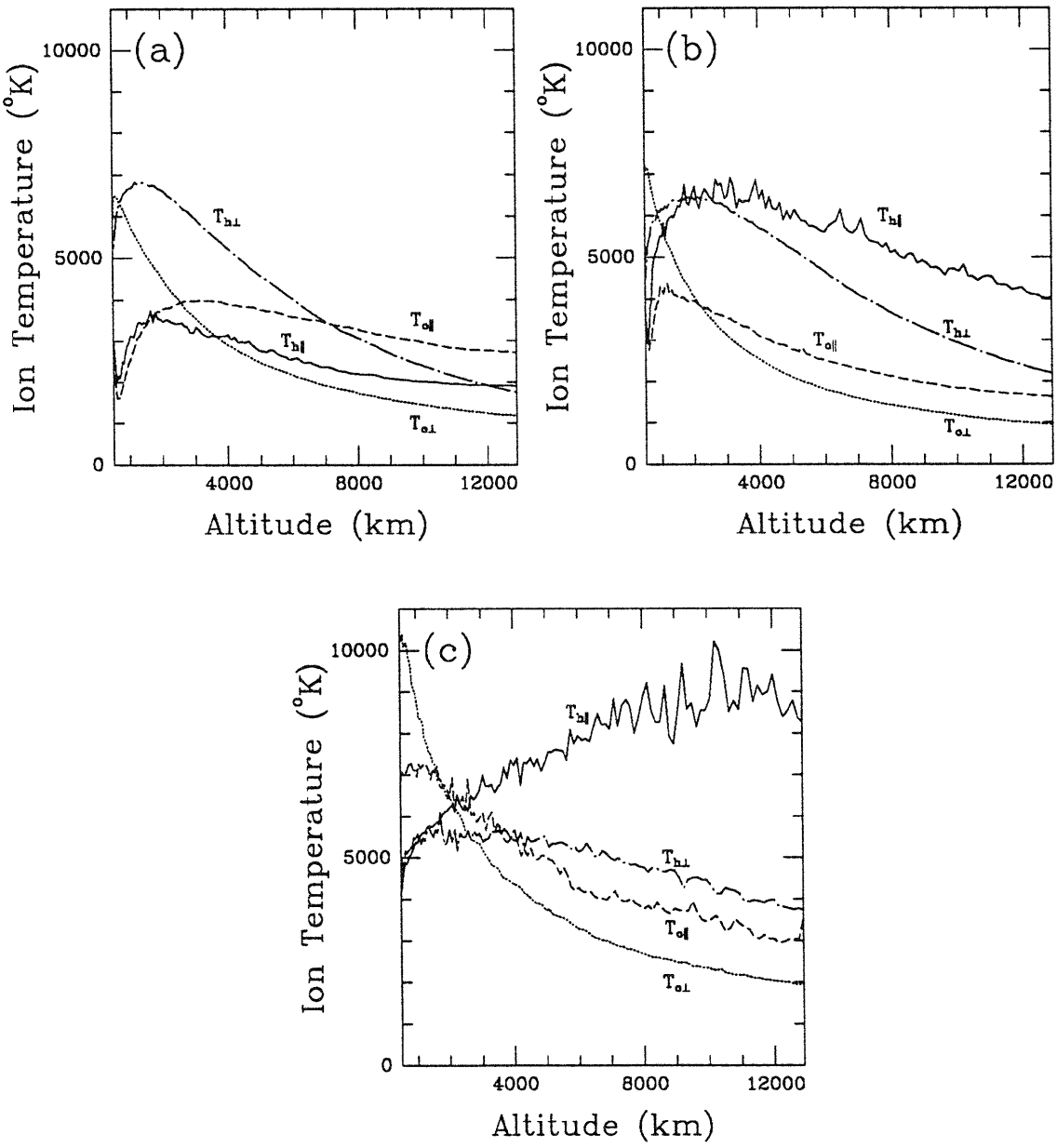

Figure 4-16: Profiles of the ion temperatures. The labels correspond to the cases listed in Table 4.4.

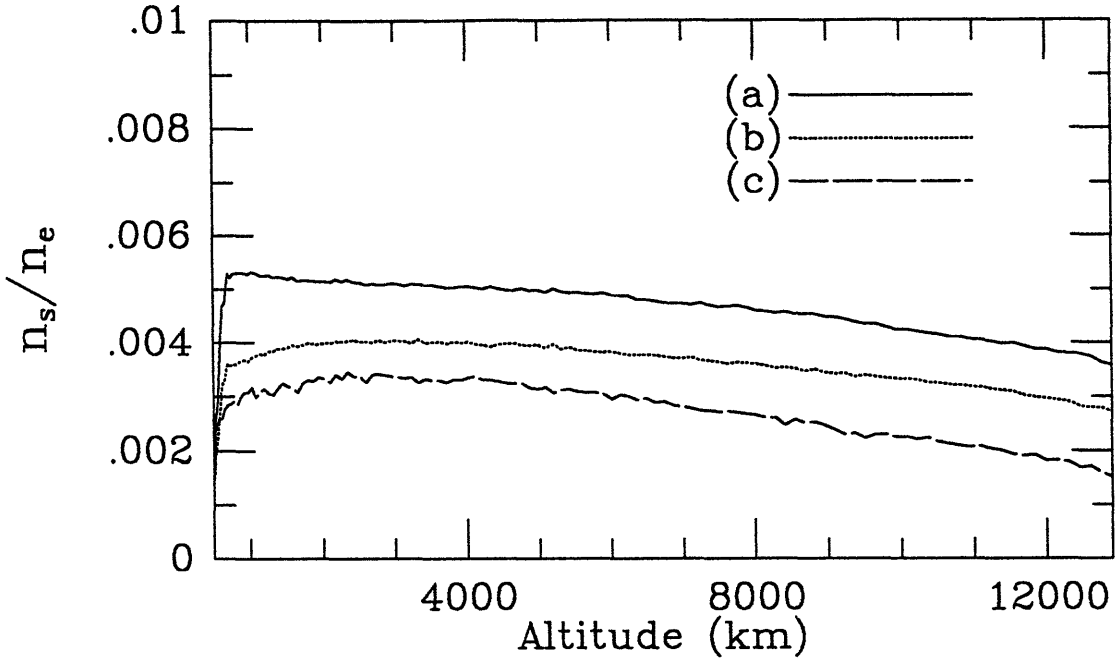

Figure 4-17: Profiles of relative photoelectron density. The labels correspond to the cases listed in Table 4.4.

particle densities, a change in the O^+ boundary temperature will alter the impact of these effects on the polar wind ion temperatures themselves. For example, it can be seen from Fig. 4-13 that Case (c) has the largest ion densities (and also thermal electron density, because of quasi-neutrality) in general. These highest densities lead to the strongest collisional diffusion, which accounts for the largest value of $T_{h\|}$ at high altitudes in the three cases considered. Similarly, the electric field is in general largest in Case (a), followed by (b). The drop in $T_{o\|}$ and $T_{h\|}$ at low altitudes (where the local electric field is the largest) in these two cases reflects dominance of the effect due to velocity-dependent momentum transfer.

A variation in the boundary O^+ temperature will result in different polar wind electron characteristics, dictated by a different self-consistent electric field. For example, the density ratio n_s/n_e and the electron temperature, shown in Fig. 4-17 and 4-18 respectively, decreases from solution (a) through (c). This is similar to the trend demonstrated by the electric field (which is the slope of the electric potential shown in Fig. 4-12). The correlation between the electric field and the relative photo-

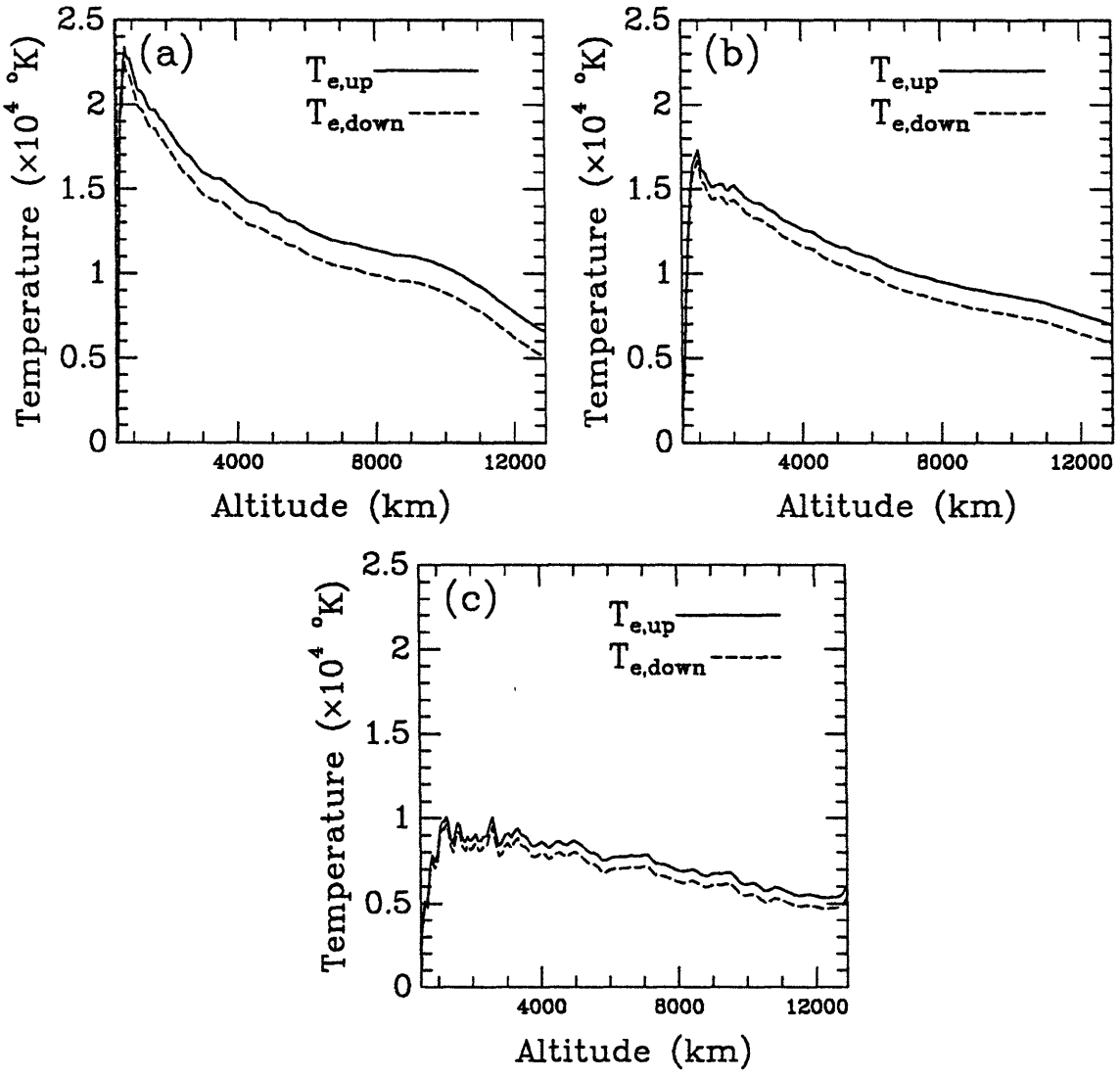

Figure 4-18: Parallel temperature profiles for the upwardly and downwardly moving electron population. The labels correspond to the cases listed in Table 4.4.

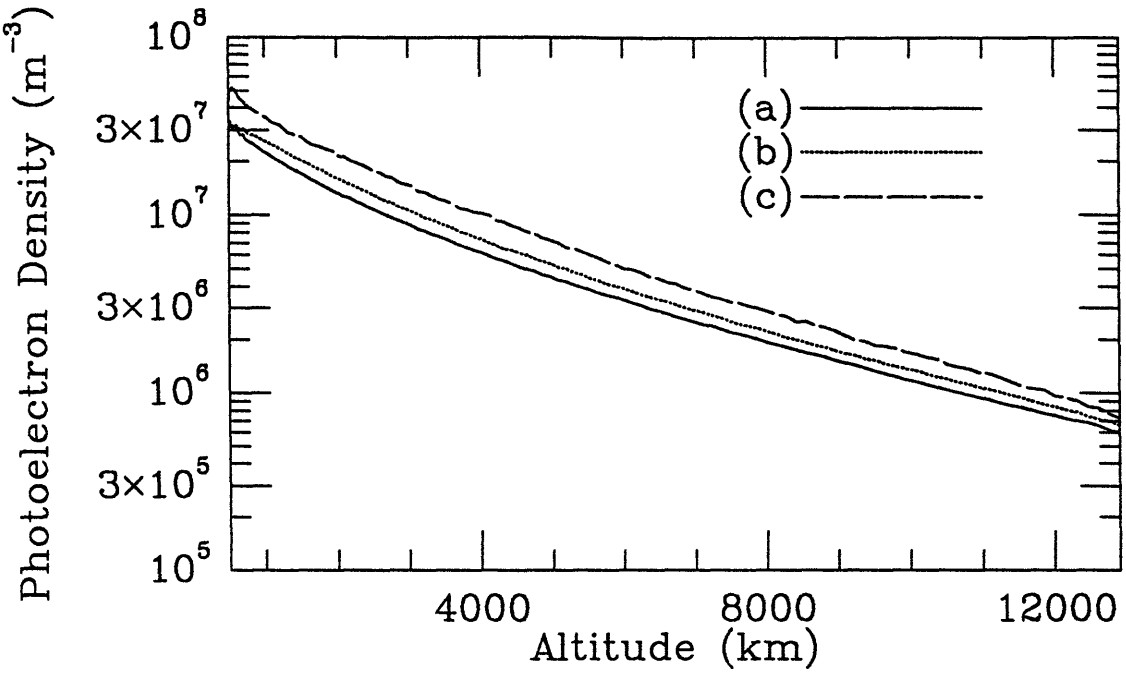

Figure 4-19: Profiles of the photoelectron density. The labels correspond to the cases listed in Table 4.4.

electron density has been discussed in Section 4.1. In fact, as explained, the behavior of the two quantities is also related to that of the electron temperature. Basically, the density ratio n_s/n_e is an indicator of the effectiveness of thermal electron heating due to their collisions with the suprathermal population. The larger the density ratio, the greater the heat source available for each thermal electron on average, leading to a higher thermal electron temperature, and a higher overall electron temperature. A higher temperature would lead to a larger pressure gradient. To balance that, a larger electric field is required.

Although the density ratio n_s/n_e is closely correlated and has the same trend as the self-consistent electric field, the photoelectron density itself, on the other hand, exhibits an opposite trend. As shown in Fig. 4-19, the photoelectron density, unlike its ratio to the thermal electron density, increases from Case (a) through (c) with increasing O^+ temperature. This increase in the photoelectron density is mainly due to the decrease in the electric field from (a) through (c). Unlike the study in Section 4.1, this parametric study keeps all the density-related boundary conditions

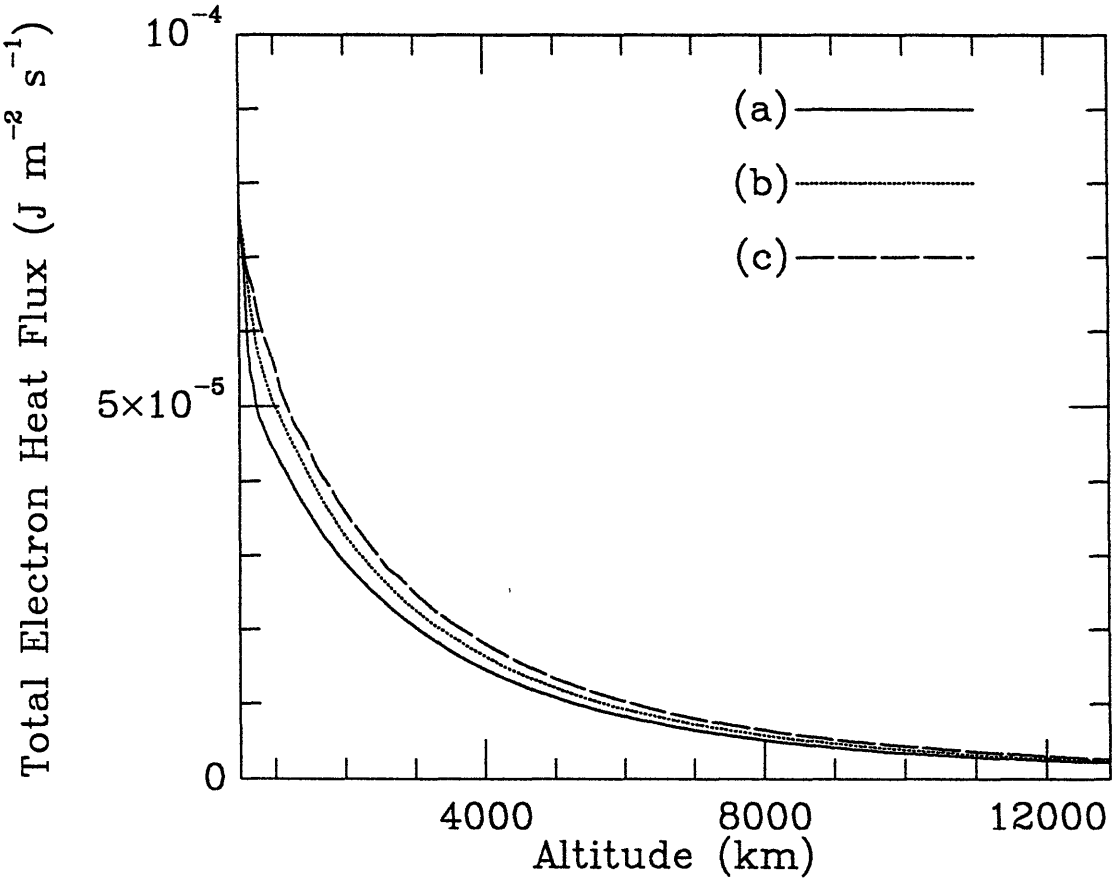

Figure 4-20: Total heat flux profiles for the total electron population. The labels correspond to the cases listed in Table 4.4.

unchanged. In particular, the photoelectron density at the boundary for all three cases considered in this section are the same. With a smaller electric field, such as that in Case (c) in our comparative study, more photoelectrons are able to overcome the electric potential barrier and escape, resulting in a larger photoelectron density throughout the simulation range. These escaping photoelectrons also contribute to the heat flux, giving rise to a total electron heat flux in the upward direction that increases from Case (a) through (c), as shown in Fig. 4-20.

As mentioned above, the photoelectron density and its ratio to the thermal electron density exhibit opposite trends in relation to the increase in O^+ temperature. The seemingly contradictory results are accounted for by an increase in thermal electron density as the self-consistent electric field decreases in response to an increase in O^+ boundary temperature (Case (a) through (c)). In fact, this change in the thermal electron density is due to a combination of quasi-neutrality and the depletion effect of the electric field on the ion densities discussed earlier: A smaller electric field would give rise to higher ion densities (compare Fig. 4-12 and Fig. 4-13), which, via quasi-neutrality, imply a larger thermal electron density.

4.3 Effect of H^+ Temperature

We have demonstrated in Section 4.1 and 4.2 that the ionospheric relative photoelectron density and O^+ temperature can significantly influence the self-consistent electric field in the polar wind, and through it lead to remarkably different outflow dynamics. In particular, we have shown that a larger ionospheric O^+ temperature would lead to a smaller electric field, due to the larger ion flux introduced by the higher temperature. This mechanism, in principle, should also apply to the H^+ ions.

In this section, we shall examine the impact on the polar wind dynamics due to the H^+ ions as a source of this ion flux mechanism. Specifically, we control the amount of H^+ flux by varying its temperature at the lower end of our simulation, and compare the different polar wind solutions generated from these boundary conditions. In this set of calculations, the H^+ temperature parameter T_{h*} is given the following values:

Parameters at 500 km altitude

Case	(a)	(b)	(c)
T_{h*} (eV)	1.0	1.8	2.8
Common parameters			
n_o (m^{-3})	4.0×10^{10}		
n_h (m^{-3})	1.5×10^{9}		
n_s/n_e	7.5×10^{-4}		
T_{o*} (eV)	1.0		
T_e (°K)	3000		

Table 4.6: Boundary conditions for the three cases with different H^+ temperature.

(a) 1.0 eV; (b) 1.8 eV; (c) 2.8 eV. These boundary values as well as those of other parameters applied to these calculations are summarized in Table 4.6. Similar to the study in Section 4.2, the initial distributions applied at the lower simulation end of the kinetic calculations only consist of the upgoing particle population, while the resulting distributions also take into account the reflected population. The resulting parallel temperatures at the lower simulation end are thus different from those used in the initial distributions. For the three solutions considered in this section, $T_{h\|}$ at the lower boundary is about 2400, 4000, and 6000°K for Cases (a), (b) and (c), respectively.

The self-consistent electric potential of these polar wind solutions is shown in Fig. 4-21. Notice that the ion flux mechanism that has been discussed in Section 4.2 still applies in this study — the electric field decreases as the boundary H^+ temperature increases from Case (a) through (c). However, because H^+ is only a minority ion species, its impact on the self-consistent ambipolar field is not as significant as that due to O^+ — variation by over 3500°K in low-altitude $T_{h\|}$ only causes the electric potential difference to change by about 1 V (see Table 4.7), in contrast to a 5 V change in the potential difference introduced by a 3000°K variation in $T_{o\|}$ (see Table 4.5).

Increasing the H^+ boundary temperature, as for O^+, seems to influence most polar wind quantities through the electric field. For example, both the relative photoelectron density (n_s/n_e) and electron temperature, as shown in Fig. 4-22 and 4-23 respectively, like the self-consistent electric field, decrease with increasing H^+ temperature (Case (a) through (c)), consistent with the physical interpretation that relates

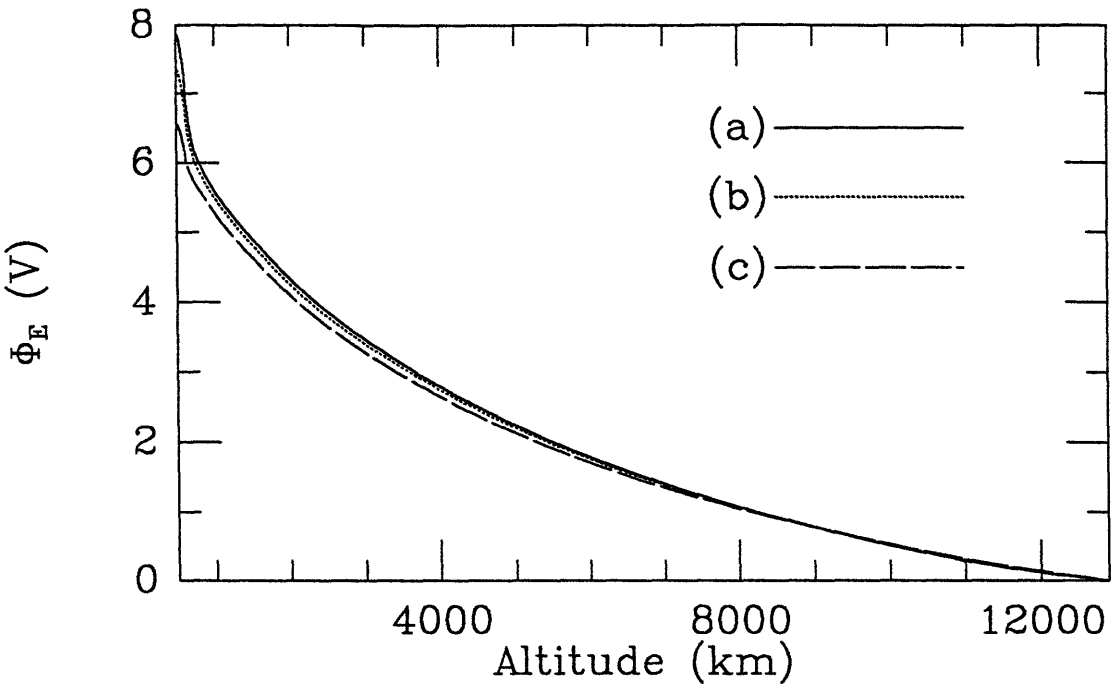

Figure 4-21: Profiles of the self-consistent ambipolar electric potential. The labels correspond to the cases listed in Table 4.6.

the three together (see Section 4.1). Because the H^+ temperature increase has a smaller impact on the self-consistent electric field than the corresponding effect of the O^+, the variations of the density ratio n_s/n_e and electron temperature among the three cases in this study are also smaller than the corresponding variations in Section 4.2 (*c.f.* Fig. 4-17 and 4-18).

The photoelectron density and the total electron heat flux also exhibit the same kind of response to the electric field as that found in the study of the O^+ case. As shown in Fig. 4-24 and 4-25, both quantities increase, in association with the increase in the H^+ boundary temperature, and the resulting decrease in the self-consistent electric field (Case (a) through (c)). The physical interpretation for such variations and their relation with the electric field variation have been discussed in Section 4.1. Basically, the electric field provides a potential barrier that the escaping photoelectrons need to overcome. The smaller the electric field, the smaller the potential barrier, and the more photoelectrons are able to escape, not only leading to a larger photoelectron density at higher altitudes, but also carrying a larger total amount of

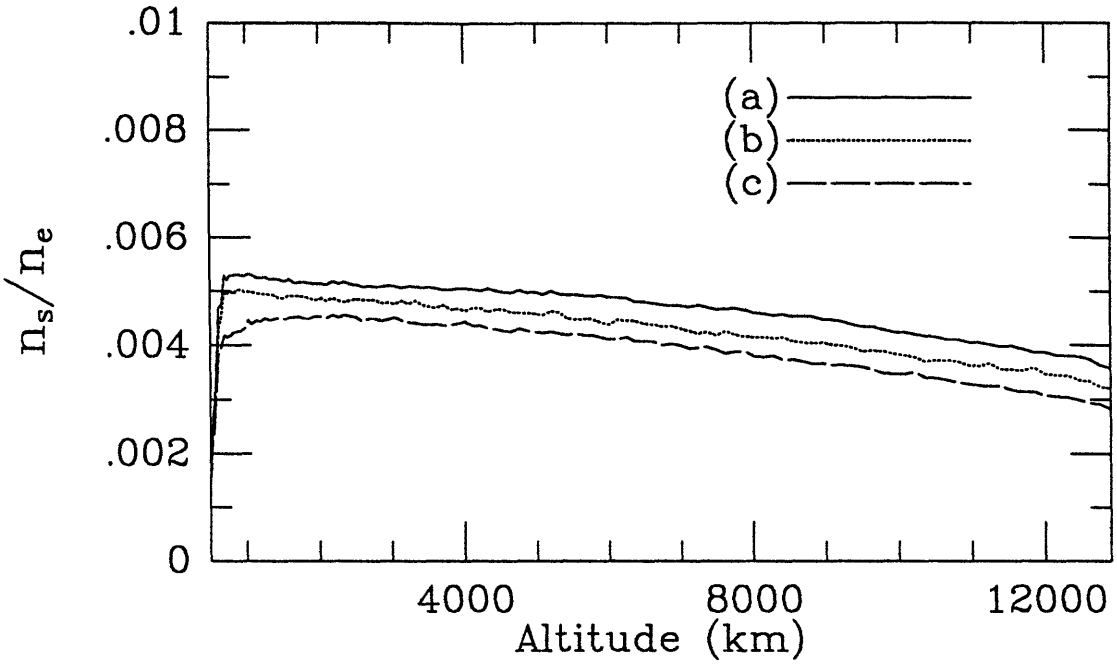

Figure 4-22: Profiles of relative photoelectron density. The labels correspond to the cases listed in Table 4.6.

heat flux. Therefore, we would expect larger changes in these quantities for a larger electric field variation. Indeed, the changes in these quantities due to increasing H^+ temperature (Fig. 4-24 and 4-25) are smaller than the corresponding changes due to the change in O^+ temperature (Fig. 4-19 and 4-20), consistent with the smaller electric field variation found in this study.

The impact of H^+ temperature on the ion quantities also seems to rely mainly on the self-consistent electric field. The impact of the electric field on the ions has been discussed in the previous sections. In particular, ions are driven upward by the electric field. In other words, an increase in the electric field tends to enhance the ion outflow, giving rise to a larger ion number flux. Such a relationship is indeed found in our polar wind solutions. Table 4.7 indicates that reducing the self-consistent electric potential difference from Case (a) through (c) (which implies reducing the electric field (*c.f.* Fig. 4-21)) leads to a decrease in the O^+ number flux. The table, however, also shows an increase in the H^+ number flux from Case (a) through (c). This increase in fact reflects the cause that leads to all the changes seen in the three cases:

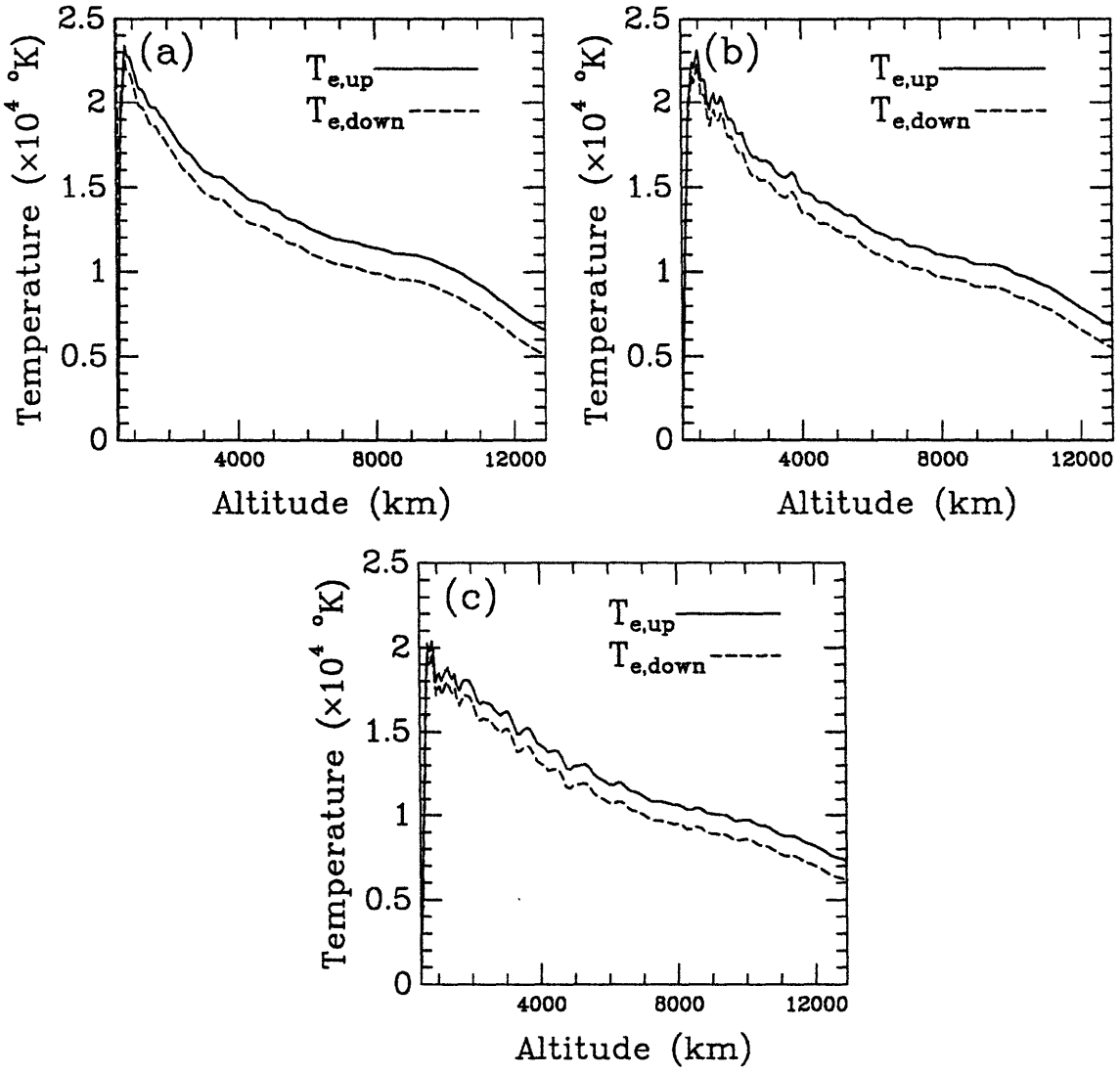

Figure 4-23: Parallel temperature profiles for the upwardly and downwardly moving electron population. The labels correspond to the cases listed in Table 4.6.

Case	T_{h*} (eV)	$T_{h\|\|}$ (°K)	$\Delta\Phi_E$ (V)	Number flux at 10000 km ($m^{-2}s^{-1}$)	
				H^+	O^+
(a)	1.0	2359	7.87	2.64×10^{11}	2.05×10^{12}
(b)	1.8	3988	7.34	3.86×10^{11}	2.00×10^{12}
(c)	2.8	6024	6.55	5.06×10^{11}	1.97×10^{12}

Table 4.7: A list of the H^+ temperature parameter T_{h*}, its corresponding parallel temperature at 500 km altitude, the resulting overall self-consistent electric potential difference ($\Delta\Phi_E$) across the simulation range, and the ion number fluxes for the three cases, whose boundary conditions are shown in Table 4.6.

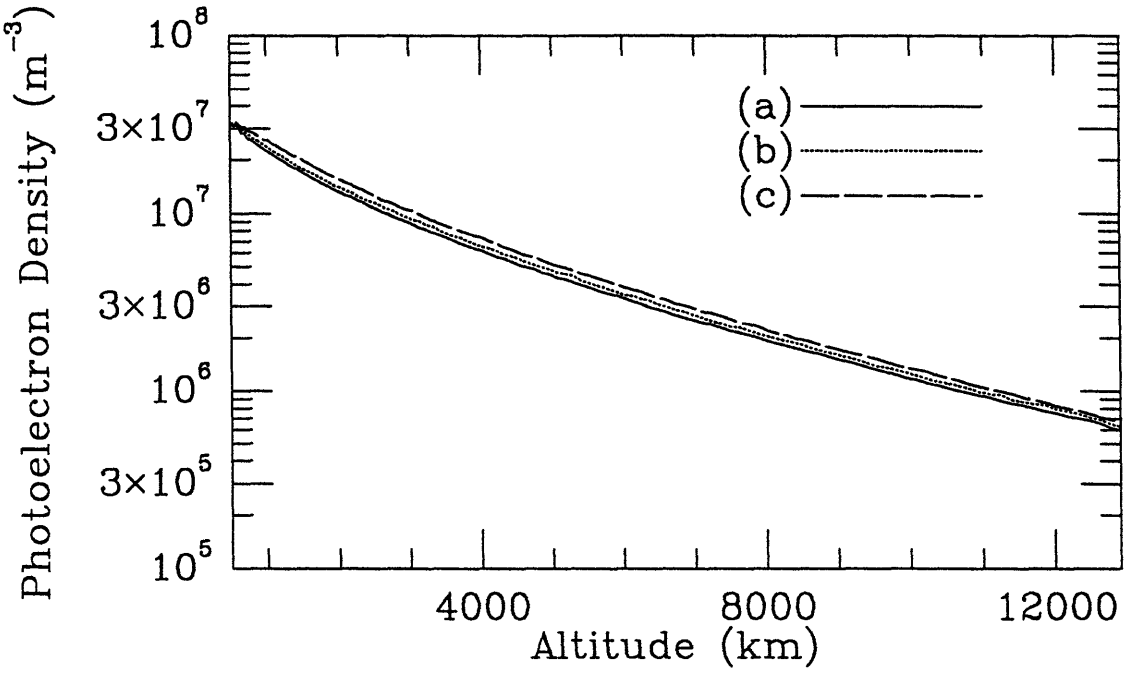

Figure 4-24: Profiles of the photoelectron density. The labels correspond to the cases listed in Table 4.6.

a different H^+ boundary temperature corresponds to a different initial distribution, and thus an intrinsically different number flux for the species. Because only the upgoing portion of the particle population constitutes the initial distributions in the kinetic calculations, a higher boundary temperature corresponds to a larger intrinsic number flux, accounting for the variation in the H^+ number flux in the three cases. In fact, a similar scenario that involves the ion number fluxes occurs in the study of the O^+ temperature effect in Section 4.2, in which the roles of O^+ and H^+ are inversed (*c.f.* Table 4.5).

The variation of the H^+ number flux in response to the change in H^+ boundary temperature brings out an important point about our comparative study. The quantities whose boundary values are affected by a change in the boundary parameter will combine "cause" and "effect" in their overall variation. This variation will result both from this direct relationship at the boundary (cause) and from the self-consistent response to the change in the boundary parameter (effect). For this reason, variations of such quantities may show rather complicated patterns. In this H^+ study, where

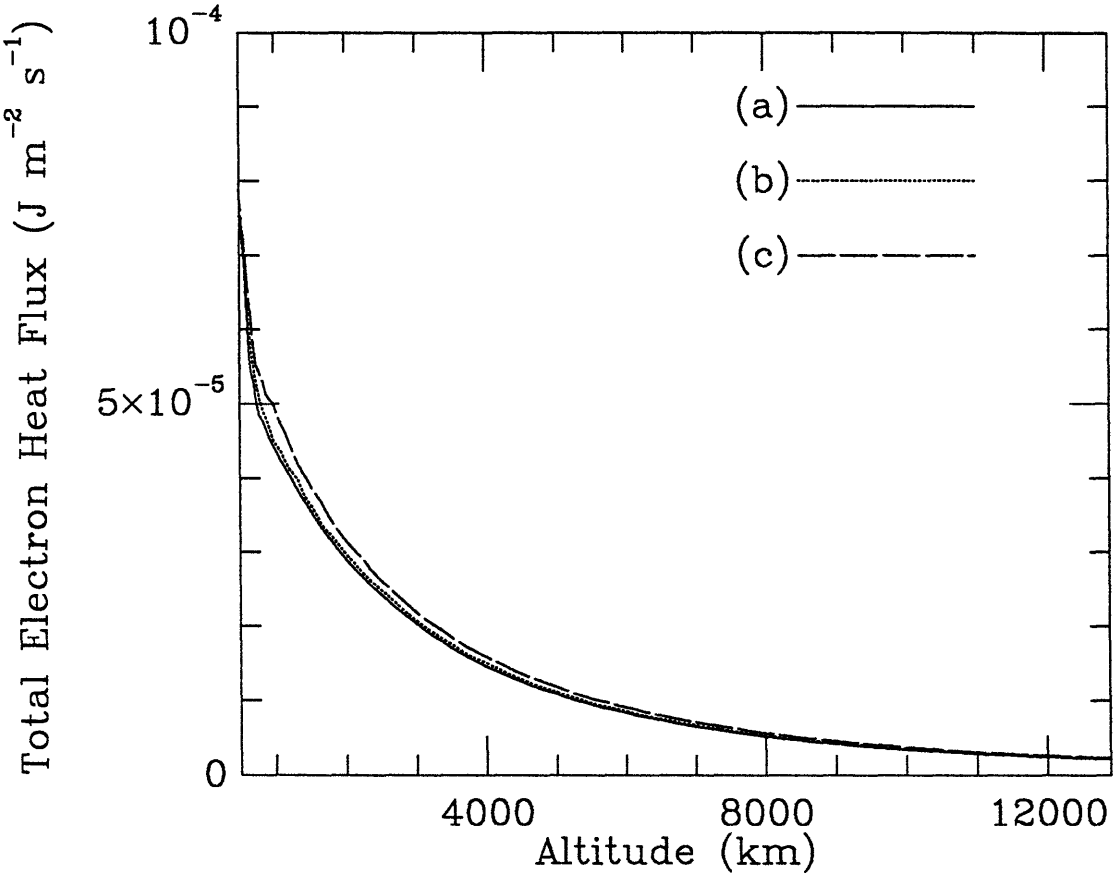

Figure 4-25: Total heat flux profiles for the total electron population. The labels correspond to the cases listed in Table 4.6.

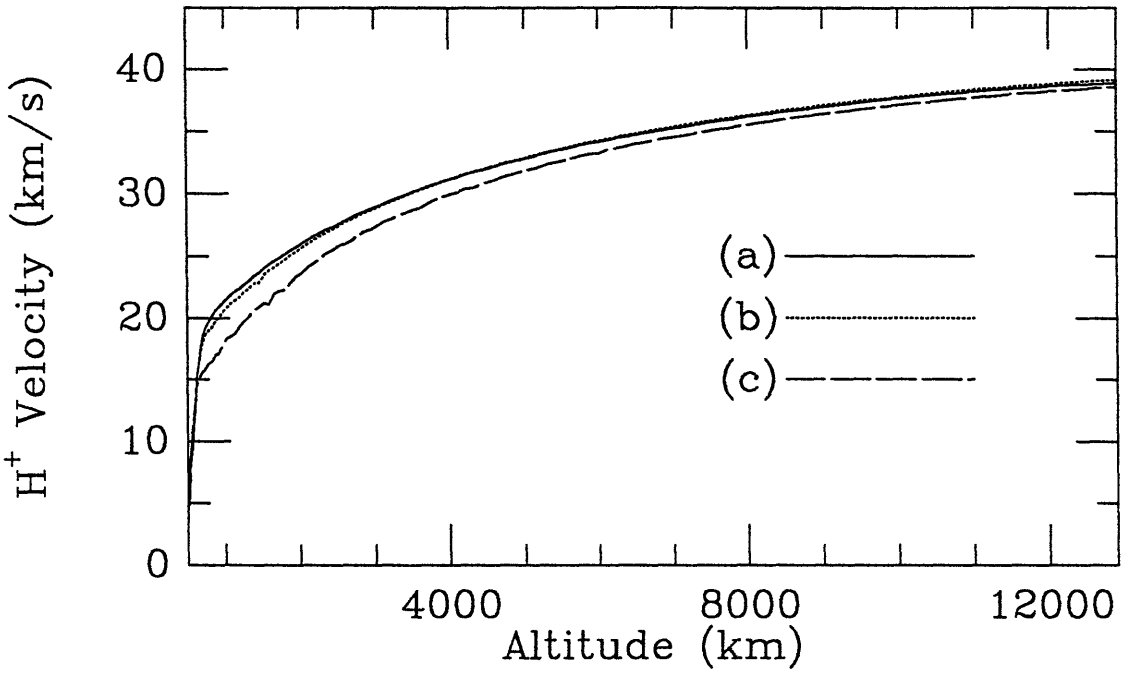

Figure 4-26: Profiles of the H^+ outflow velocity. The labels correspond to the cases listed in Table 4.6.

the varying boundary condition involves the shape of the H^+ distribution function, essentially all the H^+-related quantities are subjected to this mixing of cause and effect. Therefore, we shall focus on the O^+ when we dicuss the H^+ temperature effect on the ions, as this will reveal the self-consistent effects more clearly.

Figures 4-26 and 4-27 show respectively the H^+ and O^+ outflow velocities for the three polar wind solutions. The O^+ outflow velocity, in particular, decreases from Case (a) through (c). Such a variation is mainly due to the different extent of ion acceleration by the self-consistent electric field, which also shows a similar variation among the three cases (*c.f.* Fig. 4-21). This ion acceleration by the electric field also has an influence on the ion densities. As discussed in Section 4.2, acceleration of the escaping ions introduces a density depleting effect because of conservation of the species in the outflow. The densities of the escaping ions are thus higher when they are accelerated less, or in other words, when the electric field is smaller. The variations of the ion densities shown in Fig. 4-28 are thus also consistent with the electric field variation.

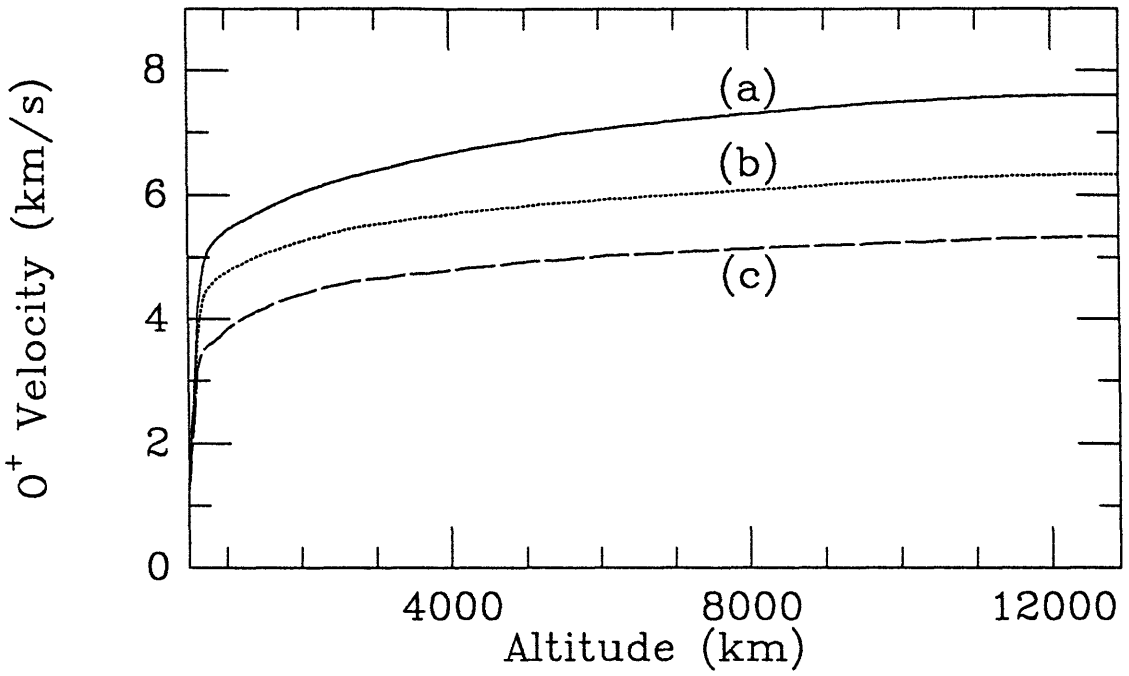

Figure 4-27: Profiles of the O^+ outflow velocity. The labels correspond to the cases listed in Table 4.6.

So far, comparison of the polar wind solutions with different H^+ boundary temperature has indicated that the effect of the H^+ temperature on the polar wind dynamics is mainly through its influence on the self-consistent electric field. Because variation of the boundary H^+ temperature only induces a slight change in the self-consistent electric field, most of the polar wind quantities only exhibit small variations in response to the H^+ temperature variation. Indeed, comparison of the ion temperature profiles of the polar wind solutions, as shown in Fig. 4-29, indicates very little qualitative difference. Because of such resemblance in the qualitative features of the ion temperatures, effects that may govern the temperatures, such as diffusion, also seem to be influenced by the boundary H^+ temperature to a rather small extent.

There is one interesting point, however, if we compare the ion temperature profiles in this study with those in Section 4.2. Notice that in all three cases shown in Fig. 4-29, both $T_{h\|}$ and $T_{o\|}$ are characterized by a downward gradient at low altitudes, while in Fig. 4-16, such decrease in temperature is clearly present only in (a), and with a diminished size in (b), but absent in (c). The difference in these temperature

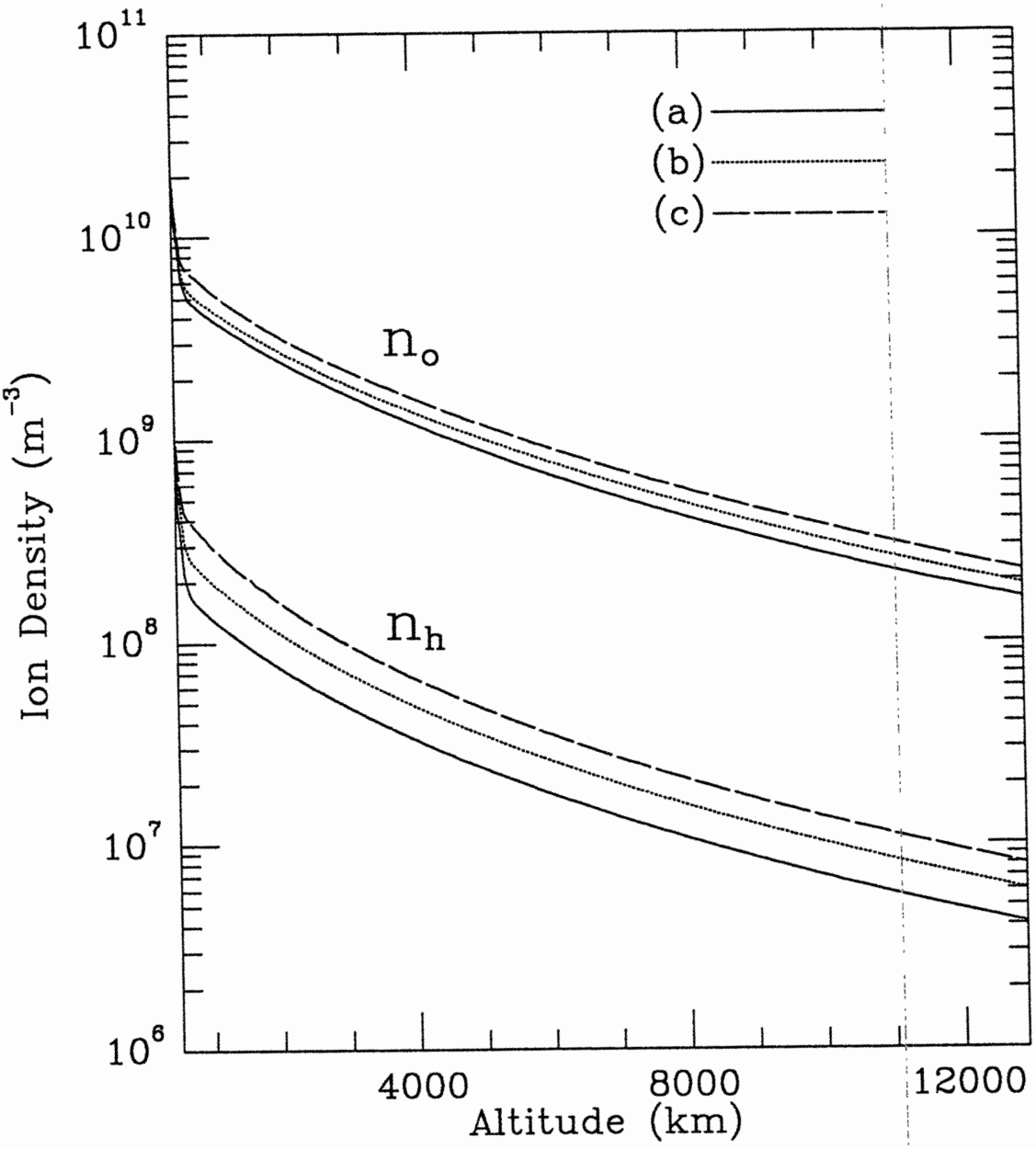

Figure 4-28: Profiles of the O^+ and H^+ densities. The labels correspond to the cases listed in Table 4.6.

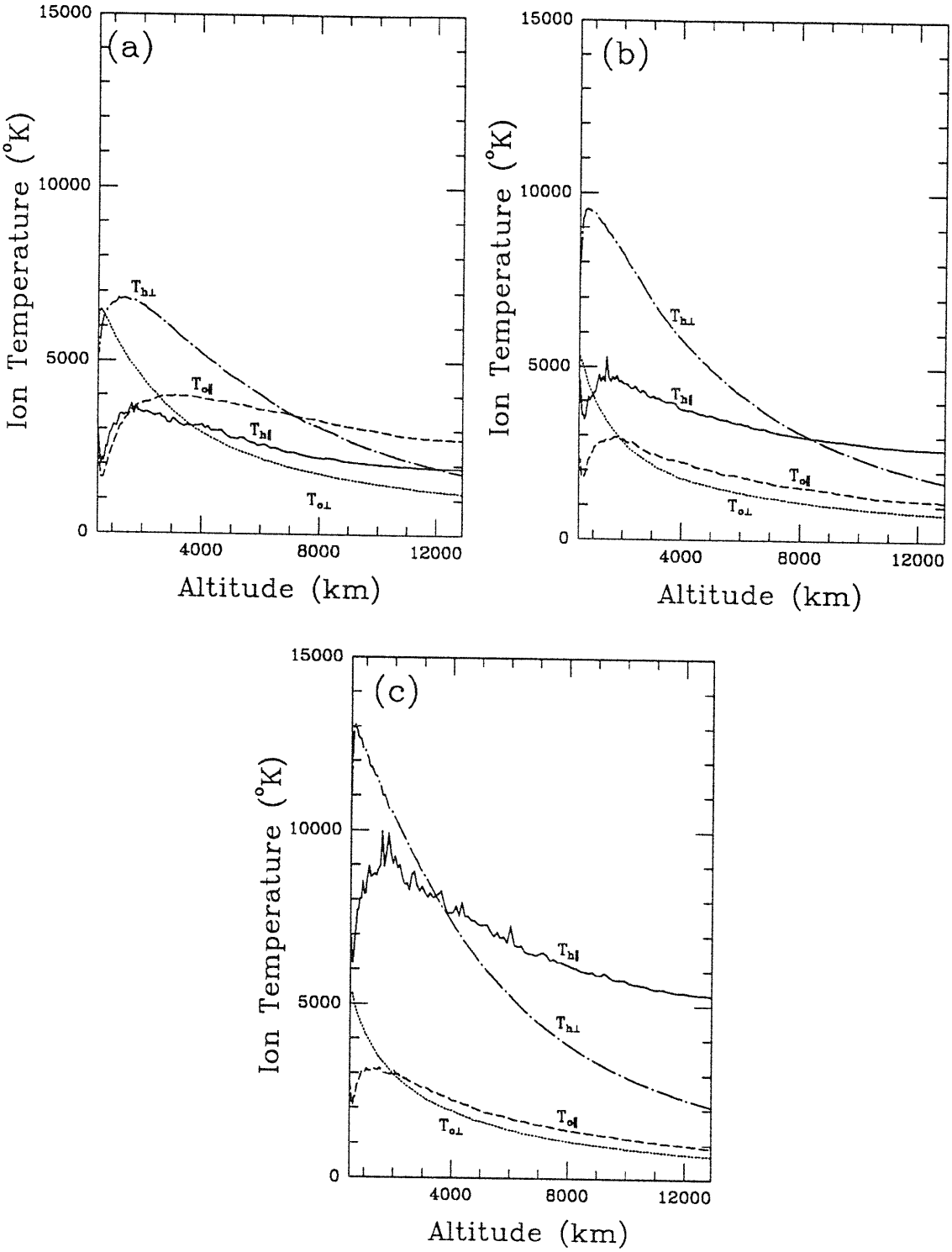

Figure 4-29: Profiles of the ion temperatures. The labels correspond to the cases listed in Table 4.6.

profiles indeed provides us with evidence that relates such features in the temperature profiles to the effect of velocity-dependent momentum transfer due to the electric field. Among the three cases shown in Fig. 4-29, the self-consistent electric field differs only by a relatively small amount (*c.f.* Table 4.7 and Fig. 4-21); this velocity-dependent momentum transfer remains dominant at low altitudes, leading in all cases to the decrease in $T_{h\|}$ and $T_{o\|}$. The same can be said about Case (a) of Section 4.2. In Case (b) and (c) of that section, however, the self-consistent electric field is noticeably smaller, especially in (c), as is evident from the electric potential difference shown in Fig. 4-12 and Table 4.5. The effect due to the electric field becomes less dominant in (b), and the parallel temperatures decrease to a smaller extent. In Case (c), where the electric field is even smaller, the impact of diffusion takes over, resulting in increases of the parallel temperatures at low altitudes. Overall, the low-altitude features in the $T_{h\|}$ and $T_{o\|}$ profiles in these polar wind solutions are consistent with the physical interpretation based on the velocity-dependent momentum transfer mechanism.

4.4 Effect of O^+ Density

In the previous sections, we have examined the impact on the polar wind due to a few ionospheric quantities, namely, the relative photoelectron density, the O^+ temperature, and the H^+ temperature. Changes in these quantities can alter the polar wind dynamics to various extents, depending on their impact on the self-consistent ambipolar electric field. Indeed, we have shown from our calculations that the self-consistent electric field becomes larger if we use a larger relative photoelectron density, a smaller O^+ temperature, or a smaller H^+ temperature at the lower boundary. Notice that all these variations in the boundary conditions either enhance the upward electron flux or reduce the ion outflow flux, without changing the density of the total electron population or any ion species.

To complete the polar wind parametric studies in this thesis, we shall examine how the polar wind dynamics varies with the ionospheric particle densities. In particular, we choose the O^+ density because it is the major ion species in the polar wind, and

Parameters at 500 km altitude

Case	(a)	(b)	(c)
n_o (m^{-3})	2.0×10^{10}	3.0×10^{10}	4.0×10^{10}
Common parameters			
n_h (m^{-3})	1.5×10^{9}		
n_s/n_e	7.5×10^{-4}		
T_{o*} (eV)	1.0		
T_{h*} (eV)	1.0		
T_e (°K)	3000		

Table 4.8: Boundary conditions for the three cases with different O^+ density.

we expect its effect to be more prominent than that for H^+. To study its effect, we generate different polar wind solutions, varying only the boundary condition for the O^+ density, n_o, in the fluid calculation. Table 4.8 summarizes all the boundary conditions applied in each case. In particular, the boundary values for n_o in these cases are: (a) 2.0×10^{10} m^{-3}; (b) 3.0×10^{10} m^{-3}; (c) 4.0×10^{10} m^{-3}.

The self-consistent electric potential profiles for the three cases are shown in Fig. 4-30. First, we can see that variation of the O^+ density, even by a factor of 2 (*c.f.* Cases (a) and (c)), leads to only a small change in the electric field, as the lines in the figure almost overlap each other. But more important is how the electric field varies with the O^+ boundary density — the electric field increases from Case (a) through (c) in response to the increasing O^+ density at the boundary.

A larger O^+ density corresponds to a larger ion flux in the outflow. This, at first thought, should tend to decrease the ambipolar field, a result contrary to the simulation. However, by changing the O^+ density but keeping the density ratio n_s/n_e the same at the boundary, we have also implicitly varied the photoelectron and thermal electron densities when we apply the quasi-neutrality condition of the classical polar wind. In this case, an increase in the imposed value of the O^+ density parameter corresponds to an increase in the photoelectron density at the boundary. This correspondence gives rise to the photoelectron density variation shown in Fig. 4-31, with the quantity increasing from Case (a) through (c). An increase in the photoelectron density, of course, leads to an increase in the total electron heat flux in the upward direction, as indicated by Fig. 4-32. Thus, by increasing only the O^+ density at the

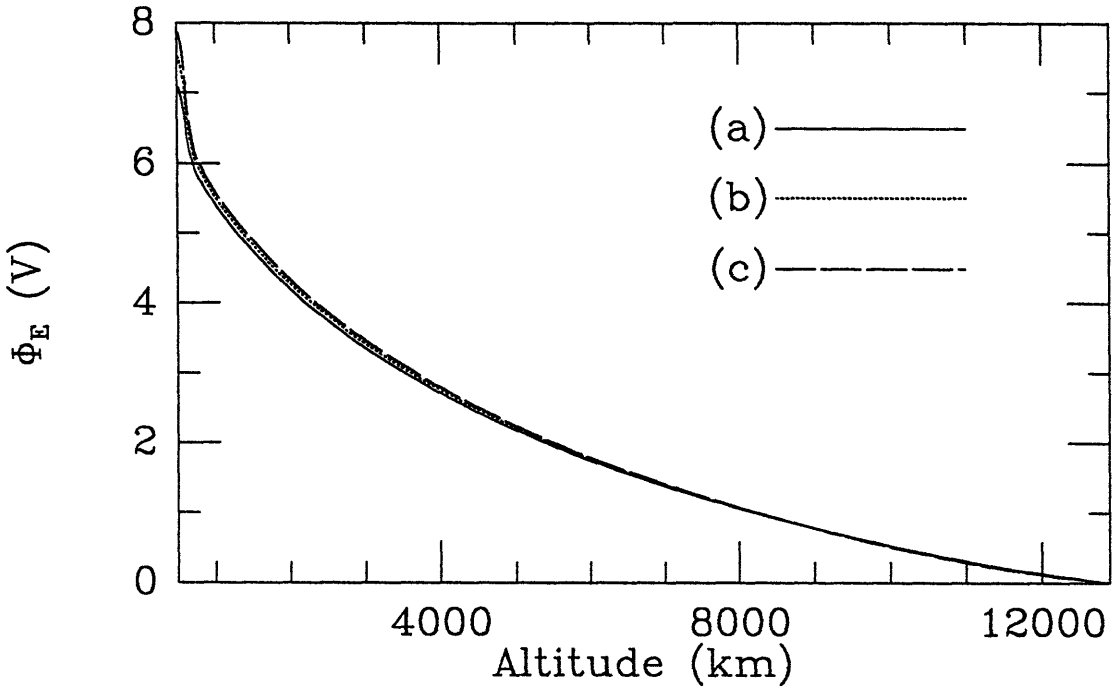

Figure 4-30: Profiles of the self-consistent ambipolar electric potential. The labels correspond to the cases listed in Table 4.8.

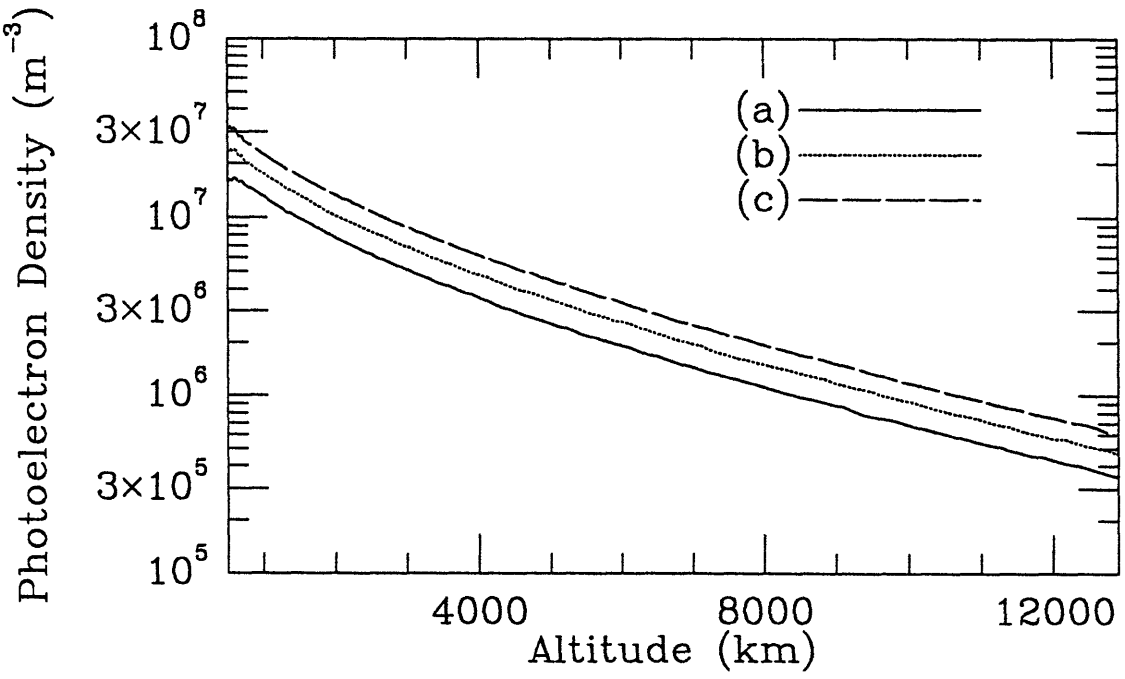

Figure 4-31: Profiles of the photoelectron density. The labels correspond to the cases listed in Table 4.8.

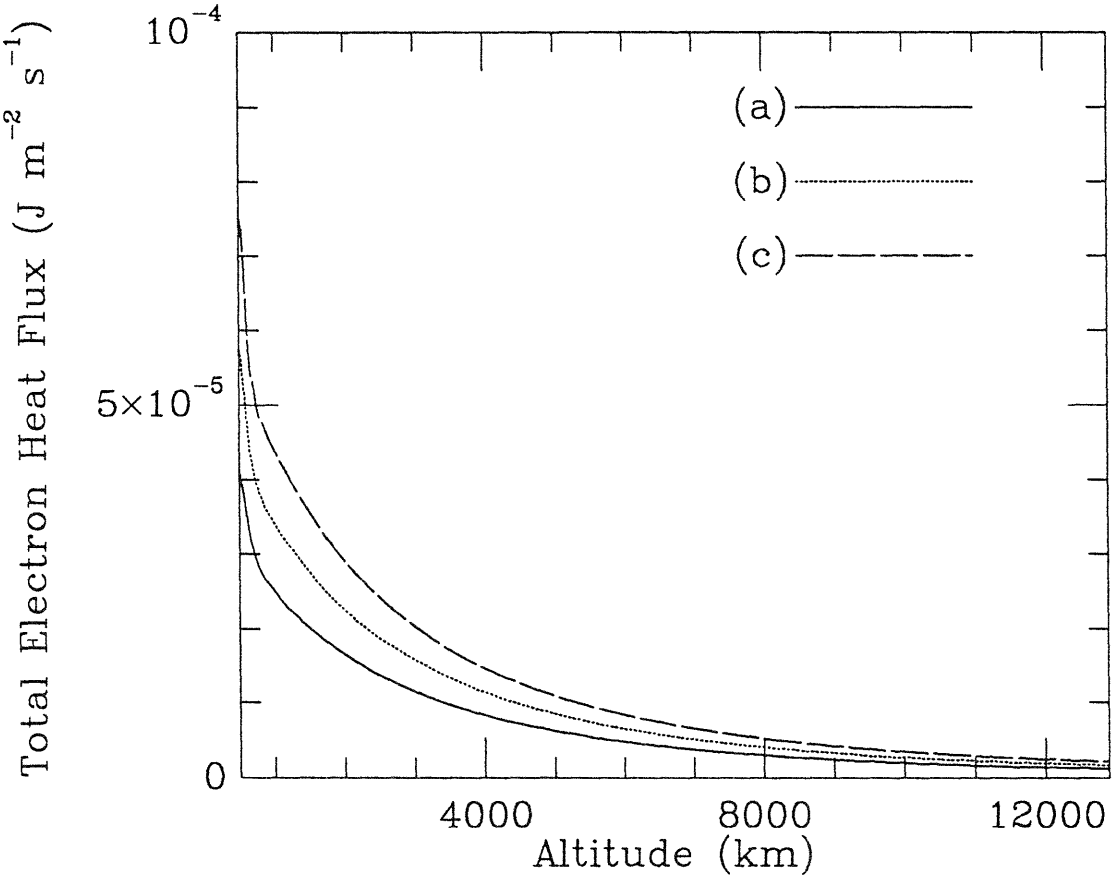

Figure 4-32: Total heat flux profiles for the total electron population. The labels correspond to the cases listed in Table 4.8.

boundary, we have enhanced not only the overall ion flux, but also the total upward electron flux. These enhancements almost offset each other so that the combined effect leads to only a slight change in the electric potential.

We can, however, clarify whether the ion or electron flux is enhanced to a greater extent by the increase in the boundary O^+ density, if we consider the average fluxes per unit density. Because the same relative photoelectron density is maintained at the boundary, the overall electron distribution will remain the same, except for the density normalization. The average electron flux per unit density is therefore unaffected by the changing boundary condition for the O^+ density. On the other hand, because O^+ has a smaller outflow velocity than H^+ due to its heavier mass, a larger relative portion of O^+ gives rise to a smaller average ion flux contribution per particle, *i.e.* a smaller ion flux per unit density. Therefore, an increase in the O^+ density at the boundary will reduce the average ion flux per unit density, but make no difference to the corresponding electron quantity, thereby enhancing the net flux contribution per unit density for the negatively charged particles. Because of the quasi-neutral characteristic of the classical polar wind, the total densities of the oppositely charged particles are the same. Therefore, an increase in the boundary O^+ density (from Case (a) to (c)) enhances the total electron flux to a greater extent compared with the total ion flux, leading to the increase in the self-consistent electric field and its potential difference shown in Fig. 4-30.

Although as we have mentioned, the boundary condition for the ratio of photoelectron to thermal electron densities, n_s/n_e, is the same for the three cases, this density ratio in general shows an increase at higher altitudes, as we go from Case (a) to Case (c) (see Fig. 4-33). As discussed in the previous sections, this increase, together with the variation in electron temperature, which also shows a slight increase from (a) through (c) (see Fig. 4-34), are consistent with the relationship (discussed in Section 4.1) that connects them with the electric field variation.

The self-consistent electric field also seems to be the mechanism whose variation induced by the O^+ density increase has the most significant impact on the O^+ outflow velocity. Figure 4-35 shows the profiles of this velocity for the three polar wind

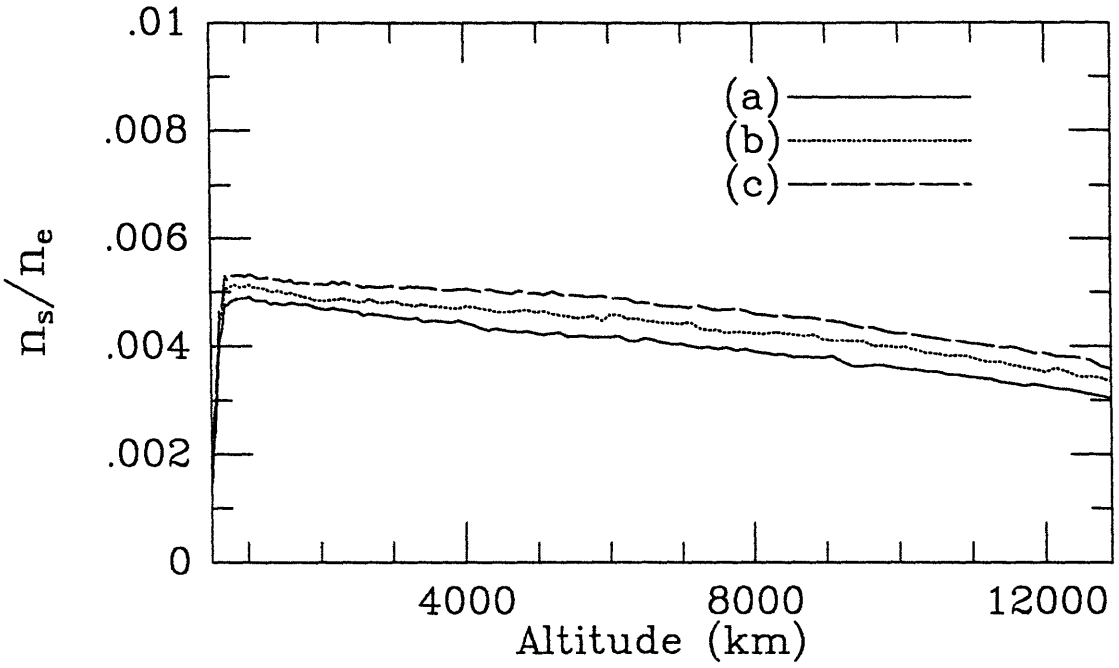

Figure 4-33: Profiles of relative photoelectron density. The labels correspond to the cases listed in Table 4.8.

solutions. Note that the variation of these profiles indicates an increasing outflow velocity from Case (a) through (c). As the self-consistent electric field also demonstrates such a trend, the effect of the O^+ density variation on its acceleration appears to be mediated by the electric field.

Acceleration of the H^+ ions in the polar wind, however, may be significantly influenced by some effects other than that of the electric field, depending on the ionospheric O^+ density. As Fig. 4-36 indicates, the H^+ outflow velocity shows a variation that is not fully consistent with the corresponding electric field changes among the three polar wind solutions. Because the electric field generally increases from (a) to (b), and from (b) to (c) (*c.f.* the electric potential profiles in Fig. 4-30), we would expect the H^+ outflow velocity to follow the same variation pattern if there were no significant competing mechanism against the electric field in accelerating the species. However, even though the H^+ outflow velocity is clearly the smallest in Case (a), it shows very little or no increase from (b) to (c). Therefore, there must be some other mechanisms which are at least as significant as the electric field in governing

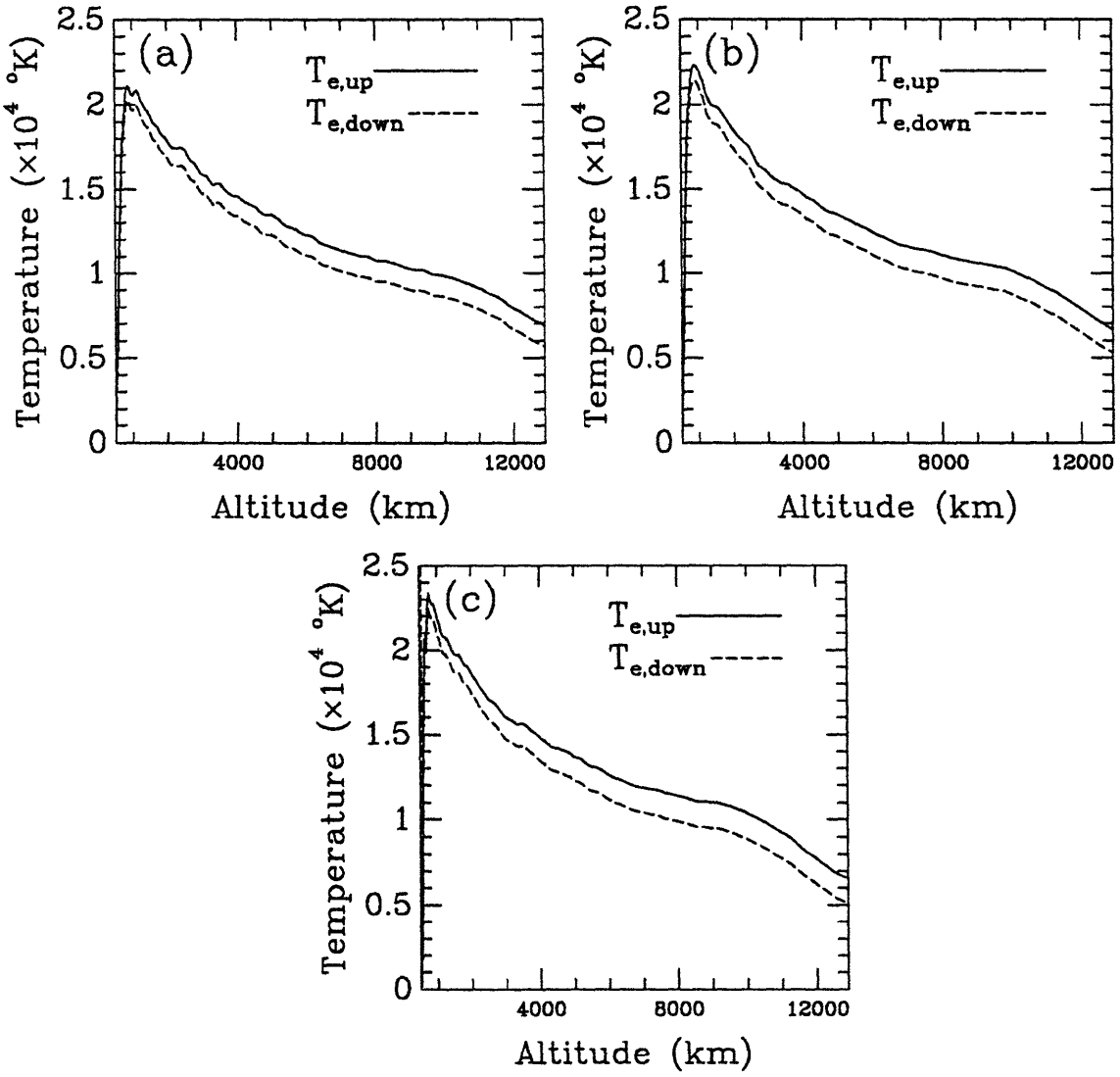

Figure 4-34: Parallel temperature profiles for the upwardly and downwardly moving electron population. The labels correspond to the cases listed in Table 4.8.

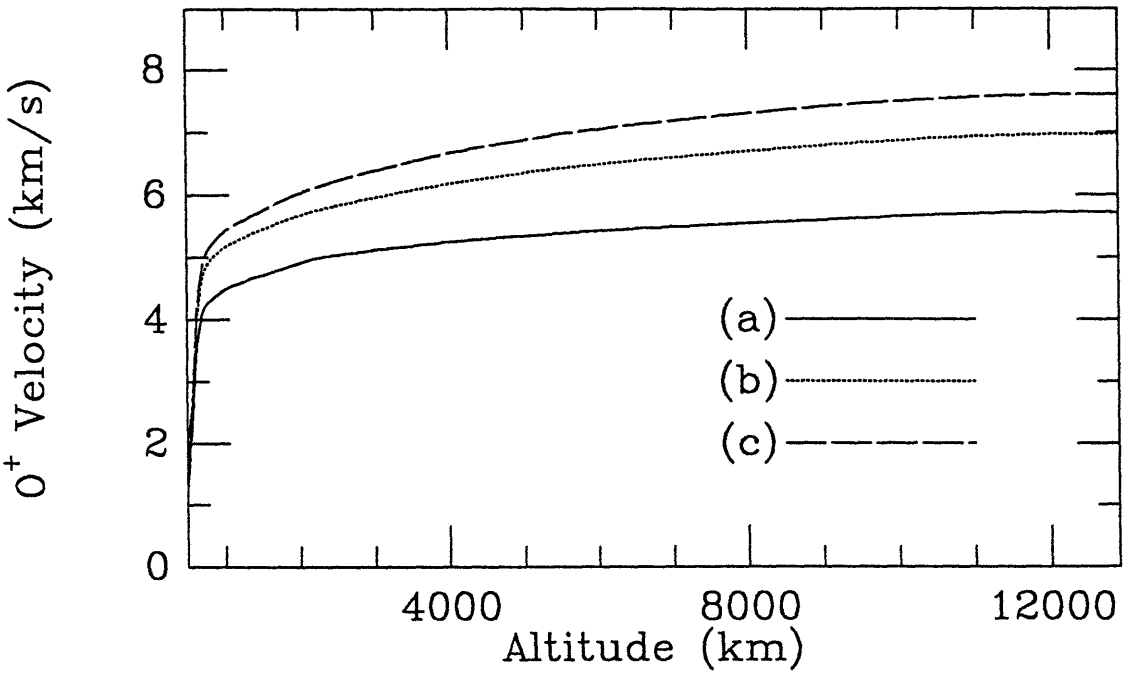

Figure 4-35: Profiles of the O^+ outflow velocity. The labels correspond to the cases listed in Table 4.8.

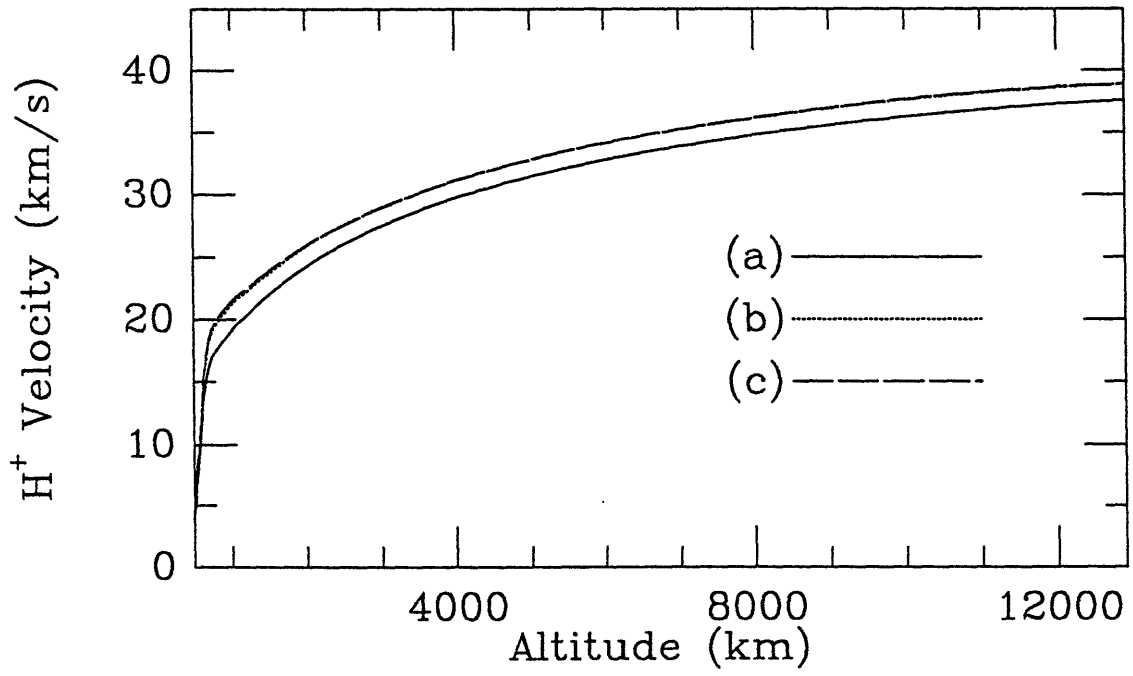

Figure 4-36: Profiles of the H^+ outflow velocity. The labels correspond to the cases listed in Table 4.8.

the H^+ acceleration, and whose effects are enhanced or reduced by the variation of the O^+ density. The mechanism in question is Coulomb collisions, in particular, those of the H^+ with the O^+ ions. We have discussed in Section 4.1 that such collisions have a slowing-down effect on the H^+ ions, due to their higher outflow velocity than that of O^+. This slowing-down mechanism thus competes against the electric field. Moreover, because the rates of collisions are proportional to the field particle densities (see Eq. (2.11)), the effect of this collisional slowing-down is enhanced by a larger O^+ density. As shown in Fig. 4-37, the O^+ density increases from Case (a) through (c) (mainly due to the imposed boundary conditions). In other words, this slowing-down effect is the strongest in Case (c), and the weakest in (a). Incidentally, ion acceleration due to the electric field is also the most effective in (c), and the least in (a). To determine which of the two competing effects is more important for H^+ acceleration when the O^+ density changes, we can refer to the H^+ outflow velocity profiles. When the O^+ density increases, the acceleration effect by the electric field seems to be more enhanced as the resulting H^+ outflow velocity increases (Case (a) to (b)). However, further increase in O^+ density (Case (b) to (c)) does not clearly favor the acceleration effect; the increasing collisional slowing-down may counteract the acceleration, resulting in minimal increase in the H^+ outflow velocity.

Collisional slowing-down also has a significant impact on the number flux of the H^+ outflow. In contrast to the electric field pushing more ions to escape, the H^+-O^+ collisions pull the H^+ ions back, reducing the number of escaping particles of the species. Table 4.9 shows that the H^+ number flux, instead of increasing with the resulting electric potential difference, decreases with increasing O^+ density (Case (a) through (c)). This variation clearly indicates that the H^+ number flux is subjected to the impact of collisions to a greater extent when the O^+ density is increased.

Collisions also have other effects on the ion dynamics. In particular, as discussed in Section 4.1, velocity diffusion arising from collisions can increase the particle temperatures. Because collisional effects are more significant with larger particle densities, the impact of diffusion should increase from Case (a) through (c) in this study. Indeed, as shown in Fig. 4-38, the ion temperatures are generally higher in (c), and

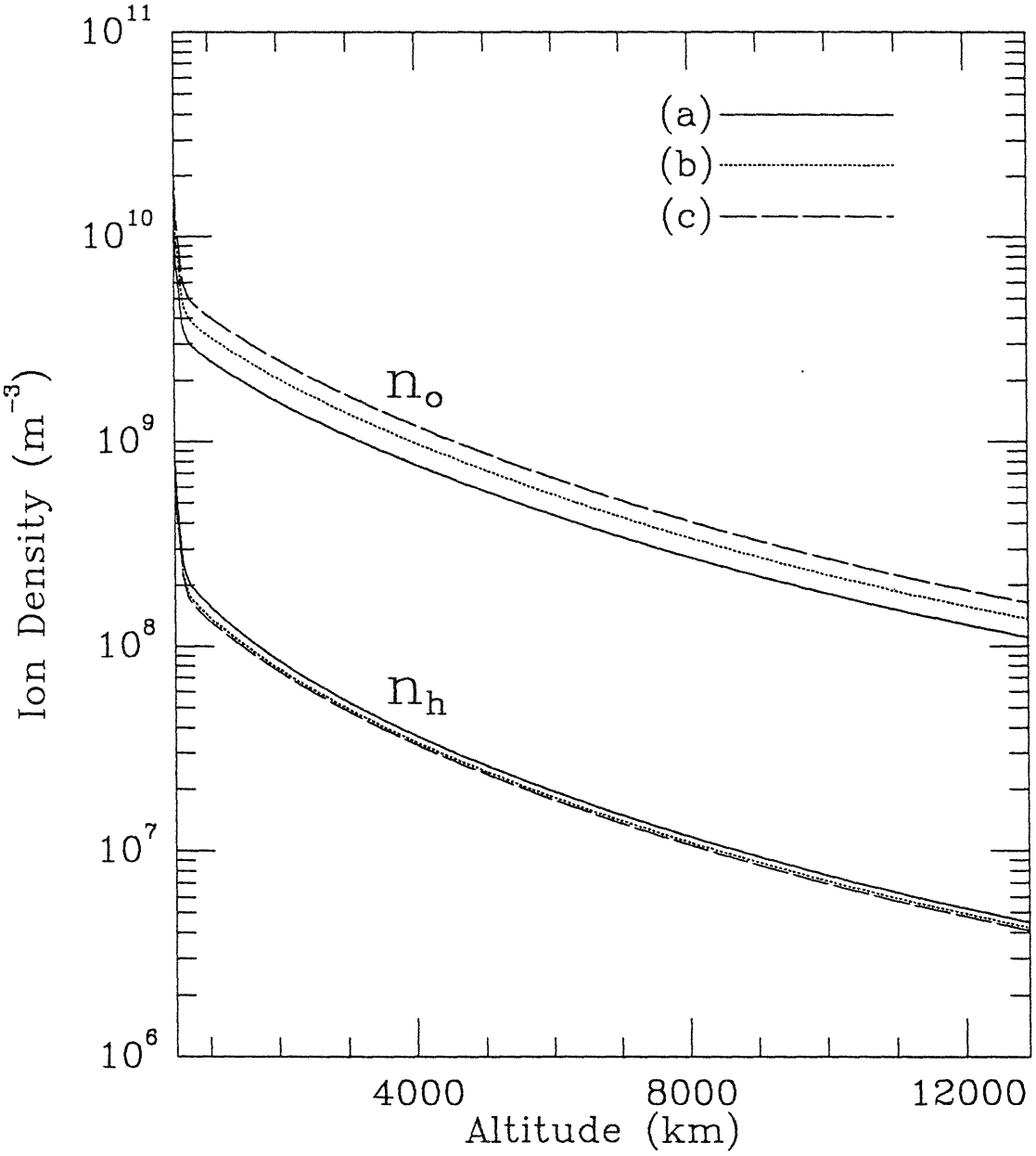

Figure 4-37: Profiles of the O^+ and H^+ densities. The labels correspond to the cases listed in Table 4.8.

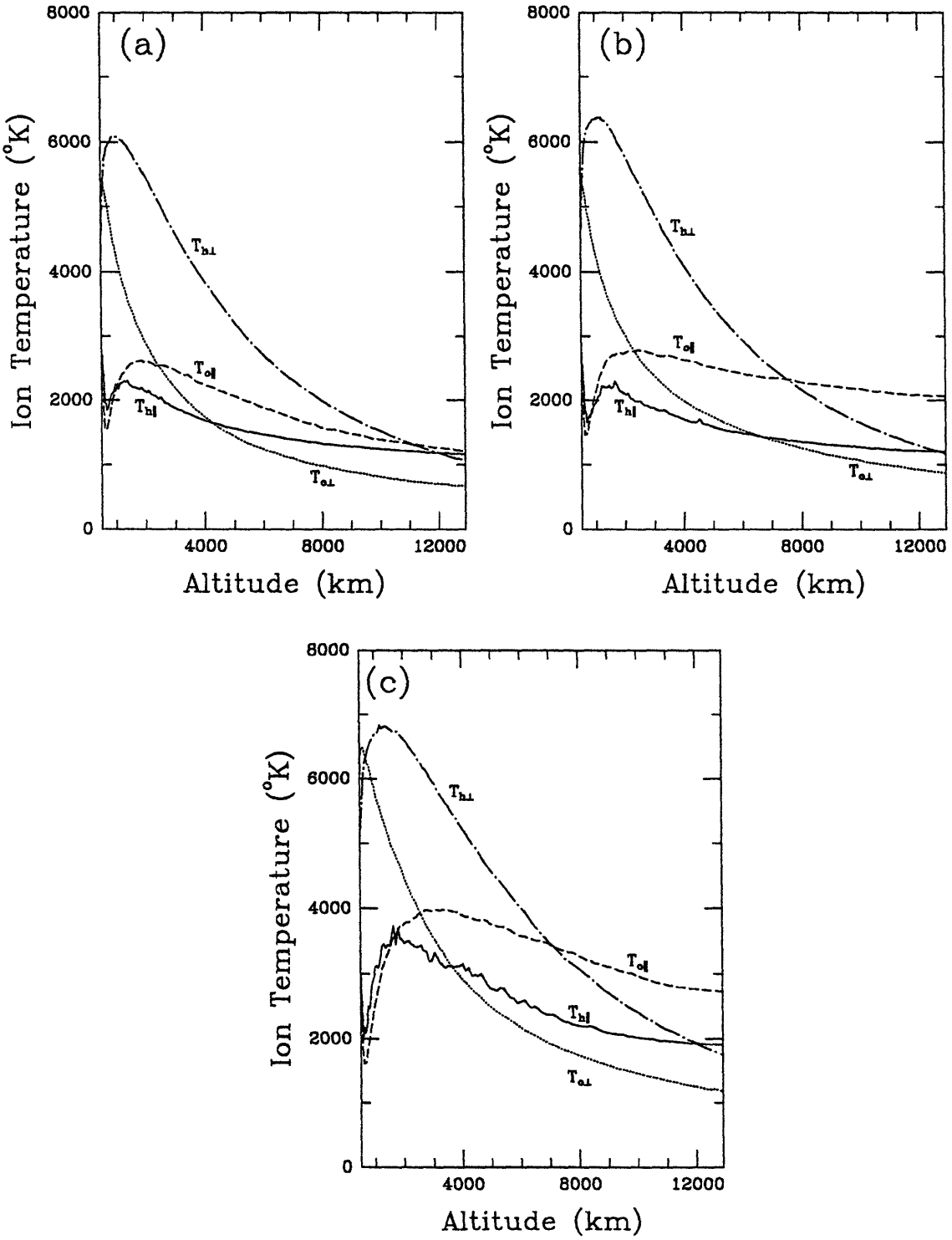

Figure 4-38: Profiles of the ion temperatures. The labels correspond to the cases listed in Table 4.8.

Case	n_o (m^{-3})	$\Delta\Phi_E$ (V)	Number flux at 10000 km ($m^{-2}s^{-1}$)	
			H^+	O^+
(a)	2.0×10^{10}	7.08	2.79×10^{11}	1.04×10^{12}
(b)	3.0×10^{10}	7.51	2.72×10^{11}	1.57×10^{12}
(c)	4.0×10^{10}	7.87	2.64×10^{11}	2.05×10^{12}

Table 4.9: A list of the O^+ density at 500 km altitude, the overall self-consistent electric potential difference ($\Delta\Phi_E$) across the simulation range, and the ion number fluxes for the three cases, whose boundary conditions are shown in Table 4.8.

lower in (a), demonstrating the significance of diffusion in the ion dynamics.

4.5 Discussion

We have studied the impact of various physical quantities in the ionosphere on the classical polar wind. These ionospheric quantities are represented by a number of parameters in our self-consistent hybrid calculation. By varying the boundary conditions on these parameters, we have examined by comparison how and to what extent some physical quantities may affect the polar wind dynamics.

The boundary conditions that we have used are within the experimental limits. However, even within such physical constraints, our polar wind solutions still demonstrate different qualitative features. Such qualitative differences are an indication of the complexity of the polar wind dynamics, an interplay between a number of physical effects. The impact of these effects on the plasma outflow depends on the polar wind quantities themselves, whose variations, therefore, may enhance or reduce these effects to different extents. Because some of these effects have opposite influences on certain quantities, the qualitative features of the polar wind strongly depend on which effect is the dominating factor.

As we have shown, some of these physical effects are particularly sensitive to certain polar wind quantities. Variations of these quantities might thus result in significant changes in the polar wind dynamics. In some cases, the change is so large that the polar wind solutions might even become unrealistic. An example is the sharp electron temperature gradient at low altitudes as shown in Fig. 4-3(d). In that cal-

culation, a relatively high density ratio is used for n_s/n_e in the boundary condition. Although the density ratio has assumed a reasonable value, when it combines with the other realistic boundary conditions, the solution features results that are beyond experimental limits. However, this does not mean that the density ratio is unrealistic; it only means the density ratio does not match well with the other boundary conditions. It is worth reminding the reader that the boundary conditions in these studies are arbitrarily chosen. However, they have to correspond to physically relevant steady-state solutions. Imposing arbitrary conditions may result in "transient" behavior in the boundary region. At the present time, we rely on physical intuition, informed by observations in the general vicinity of the boundary area. Unfortunately, we have not yet developed an algorithm that enables us to systematically verify whether a given set of boundary conditions will indeed correspond to a steady-state solution; we shall leave that to future refinements of this work. In these parametric studies, we are primarily interested in how various quantities affect the polar wind. However, we are also interested in how sensitive the dynamics of the outflow is to these quantities. Thus, cases leading to the "transient" behavior near the low-altitude boundary mentioned earlier are still useful in this regard.

Indeed, from those cases, we have learned that the polar wind dynamics is particularly sensitive to the relative photoelectron density in the ionosphere. Such sensitivity is mainly due to the large amount of upwardly directed heat flux carried by the photoelectrons. Variations in the photoelectron density will result in a significant change in the amount of electron heat flux. For a similar reason, namely the ion number flux, the polar wind is also rather sensitive to the ionospheric O^+ temperature (but not the H^+ temperature) for the range of parameters considered. The number flux of the ion outflow is mainly contributed by the upgoing portion of the ionospheric O^+ and H^+ distributions, whose energy spreads are represented by their respective temperatures. In general, the higher the temperature, the more energetic the ions, and the larger their number flux contribution to the outflow. Because O^+ is the major ion species in the polar wind, its distribution has a significant impact on the total ion number flux. Its temperature thus becomes an important factor in determining this ion flux.

On the other hand, the H^+ temperature has much less influence on the ion number flux, due to the relatively low density of the species.

Variations of these ion and electron fluxes can enhance or reduce the self-consistent electric field. For instance, a larger upward electron heat flux, or a smaller number flux for the ion outflow would lead to a larger electric field. In fact, the ambipolar electric field is the main reason for the sensitivity of the polar wind dynamics to these particle fluxes. Throughout our study, effects of the ambipolar electric field have repeatedly appeared in the results of various ion and electron quantities; these effects suggest it to be one of the most important mechanisms in the polar wind. For example, acceleration of the ions, O^+ in particular, by the electric field is the mechanism with the most apparent effect on the ion outflow velocities. The photoelectron density, and the amount of heat flux associated with it, are also influenced by the electric field, as the electric potential provides an energy barrier reflecting some of the escaping photoelectrons.

Another mechanism revealed by our study to have a significant influence on the ion dynamics is Coulomb collisions. We have identified at least two different effects that arise from collisions. First, because H^+ has a higher outflow velocity than O^+, the interaction between the two species, in particular, slows down the former, giving rise to a competing effect against the acceleration by the electric field. Second, collisions lead to velocity diffusion, which increases the temperature of the species whose collisions are described. In the polar wind, where the ions primarily travel upward, diffusion tends to create upward ion temperature gradients. Because collisional rates are proportional to the density of the background species (n_β in Eq. (2.11)), collisional effects on the polar wind ions are primarily due to their interaction with O^+, the majority ion species. Hence, the effects of collisions are more apparent when the O^+ density is high. Indeed, as we raise the boundary value of the O^+ density in our calculation, both collisional effects mentioned above become more significant. As an example, the increase in the collisional slowing-down effect acting on the H^+ number flux even dominates the corresponding increase in the electric field to the extent that the flux decreases.

Of course, collisions also have other effects on the ions. For example, similar to the collisional slowing-down of H^+, the O^+ outflow velocity is enhanced by conservation of momentum. However, because O^+ has a heavier mass and a larger density than H^+, the change in the O^+ outflow velocity due to this collisional effect is very small, and generally negligible compared to the change caused by the electric field.

Thus, the polar wind dynamics is highly complex. Not only are there numerous kinetic effects affecting this plasma outflow, but, in addition, these effects may also influence each other through their impact on the global evolution of the particle species, leading to a complex self-consistent picture. Due to this complexity, it is virtually impossible for us to study the impact of every physical effect or particle property on the polar wind itself. However, with these parametric studies, we might gather enough information to draw certain general conclusions about the polar wind dynamics. As an example, note that throughout the studies, we have used the same function to represent the photoelectron distribution. If a different distribution function is used, we can deduce from the energy flux argument that if the photoelectron population is more energetic, the self-consistent electric field will be larger. From there, we might be able to relate this electric field to the qualitative difference of various polar wind quantities.

Chapter 5

Extension of the Self-Consistent Hybrid Model — Solar Wind Application

In Chapter 3, we have introduced our self-consistent hybrid model, a new approach to describe the classical polar wind that takes into account the complex kinetic effects in the plasma outflow. Although this self-consistent approach was developed for the classical polar wind, its versatility, in particular, its ability to incorporate kinetic physics — such as Coulomb collisions — should make the model useful in other plasma applications.

One area of space plasmas to which the model can be readily extended is the solar wind. Both the polar and solar winds are examples of field-aligned global collisional plasma outflows in space. The physics that governs them is quite similar, and leads to features common to both. For example, electron distributions in both the polar and solar winds are often characterized by non-thermal features. In the polar wind, as mentioned in Section 1.1.1, and shown in Fig. 1-1, the DE-1 and DE-2 satellites have observed electron distributions with field-aligned anomalous energy fluxes [*Winningham and Gurgiolo*, 1982]. These fluxes are associated with the asymmetric tail component of the distributions, where the outward tail population is observed to be more energetic than the downward one, giving rise to an outwardly directed heat flux.

The solar wind electron distribution measured by the Helios spacecraft [*Pilipp et al.*, 1987] also demonstrated a similar anomalous feature: the outgoing suprathermal component in the field-aligned direction is more energetic than its sunward counterpart, suggesting an electron heat flux in the anti-sunward direction.

Such non-thermal features in the electron distributions of both plasma outflows have been shown to arise from global collisional effects, in particular, those due to the velocity-dependence of the Coulomb collisional rates [*Scudder and Olbert*, 1979; *Yasseen et al.*, 1989]. Similar effects have also been shown to affect the H^+ distribution in the solar wind. Using a simplified velocity-dependent collisional operator, *Livi and Marsch* [1987] demonstrated the formation of H^+ distributions characterized by an isotropic core and field-aligned tails. Again, these tails are formed by the combined action of the electric and magnetic fields, and the velocity-dependence of the collisional rates used.

Because of its kinetic treatment of both ions and suprathermal electrons, the results of our model can be compared to both Scudder and Olbert's treatment of the suprathermal electrons and Livi and Marsch's treatment of the majority ion. We should stress, however, that our approach goes well beyond the work of these groups in that our model uses a more general Fokker-Planck collisional operator, and deduces the field-aligned potential self-consistently. From a personal point of view, I find this application to the solar wind intellectually satisfying for yet another reason: The idea implemented in this thesis originated in Scudder and Olbert's pioneering studies of halo electrons in the solar wind. Their idea was later applied to the polar wind. These early studies suffered from the fact that the electric field was assumed and not deduced self-consistently. This major shortcoming is remedied by the polar wind model presented in this thesis. With this solar wind application, this idea has gone full circle to address more definitely the problem for which it was originally developed.

5.1 Comparison of the Polar and Solar Winds

Indeed, when one compares the classical polar wind and the solar wind, one can find a number of similarities. Besides the fact that both are global collisional plasma outflows in space, the magnetic field configurations for both flows share a few characteristics. The geomagnetic field in the region near to the earth is approximately a dipole configuration, and its magnitude decreases monotonically with altitude. In the polar cap region where the polar wind occurs, in particular, the magnetic field lines are open and divergent. For the solar wind, although there are a number of proposed magnetic field models, *e.g.* the Parker spiral, they all assume the existence of open, divergent magnetic field lines, with the magnitude of the field decreasing with heliocentric distance.

The nature of the polar and solar wind outflows is also basically the same. The classical polar wind conditions — a steady-state, quasi-neutral and current-free flow from a continuous source — also apply to the solar wind. In regard to flow properties, downstream of both the polar and solar winds, the ion outflows are observed to be supersonic, implying a transition from a subsonic to a supersonic regime in both cases. Both flows also change from collisional near their respective sources to collisionless further downstream.

Electron distributions in both outflows, as mentioned, show similar non-thermal features. In fact, measurements in both cases have indicated a thermal and a suprathermal electron components in the distribution. In the polar wind, the suprathermal component is primarily due to photoelectrons. For the solar wind, the thermal electrons constitute the core, while the suprathermal component has been dubbed the "halo." As mentioned earlier, formation of the suprathermal tail component of the electron distributions, in both cases, is due to global collisional effects. In fact, Coulomb collisions may be the most significant microscopic interaction in the polar wind, as wave-particle interaction may not be important in the polar cap, a relatively quiescent region. Coulomb collisions, as we shall show in Section 5.2.2, also have a strong impact on the solar wind dynamics, in particular, that of the low-

speed solar wind, where wave-particle interaction is believed to be rather insignificant. Wave-particle interactions, however, play an important role in the dynamics of the high-speed solar wind.

Thus, in setting, dominant physics, and the resulting particle properties, the classical polar wind and the solar wind are strikingly similar.[1] Because of this striking similarity, the self-consistent hybrid model should be readily applicable to the solar wind.

There are, however, some minor differences between the two outflows that should be taken into account. The most noticeable difference is the ion composition. The polar wind ions primarily consist of two species, O^+ and H^+, with the heavier ion being the more dominant species. Ions in the solar wind, on the other hand, are dominated by light species. The most abundant ion species is H^+, followed by He^{++}. In other words, the solar wind ion composition has a different characteristic from that of the polar wind in that it is dominated by the species with a larger charge-to-mass ratio. Such a difference may lead to significantly different outflow properties, but only requires a parametric adjustment in the numerical implementation of our model.

The most significant difference between the polar and solar winds, from a theoretical modeling point of view at least, is the availability of experimental data in the source region of the plasma outflow. The main source of the polar wind is the ionosphere, where *in situ* measurements are feasible [*Lee et al.*, 1980]. Realistic boundary conditions for the simulations can thus be easily chosen. On the other hand, no *in situ* measurements is possible in the coronal holes, the source of the solar wind. For a model, such as the self-consistent hybrid model, that requires boundary conditions at the source, application to the solar wind is a little more complicated than the polar wind application. We will discuss this point further in the next section.

There are several solar spacecraft and polar earth-orbiting satellites that provide considerable data on the downstream properties of the solar and polar winds. For example, Helios I and II, more recently Ulysses, and SOHO in the near future fulfill roles in the solar wind similar to those of DE-1 and Akebono in the polar wind.

[1]Indeed, historically, the polar wind was named in analogy with the solar wind [*Axford*, 1968].

Indeed, the solar wind is better diagnosed than the polar wind: its electron temperatures, which are larger than the instrument's cutoff energies, enable the spacecraft instruments to sample electrons at energies well within the core of the distribution. In the polar wind, this is difficult to achieve because the electron temperatures are smaller than this experimental cutoff (see Fig. 1-1). Ulysses, in particular, is the first spacecraft to ever explore the solar polar regions. In fact, recent issues of *Science* and *Geophysical Research Letters* were devoted to Ulysses data. The recent availability of these data, together with data expected from SOHO (which has been launched recently) and other future spacecraft, make the solar wind a particularly timely and relevant subject to study with our model.

Table 5.1 is a summary of the similarities and differences between the polar and solar winds. Overall, the major characteristics for the two outflows, such as the nature of the flow, the magnetic field configuration, and microscopic effects, are generally alike. Therefore, extension of the self-consistent hybrid model to the solar wind application can be readily done, except for some minor adjustments.

5.2 Application to the Solar Wind

As our polar/solar wind comparison has pointed out, the main complication in extending the self-consistent hybrid model to the solar wind is the lack of measurements in its source region, the coronal holes. Therefore, there are no rigid limits for the boundary conditions. The only guideline for choosing those boundary conditions would be from observations downstream of the solar wind. Thus, to obtain a realistic solar wind solution requires adjustment of the boundary conditions to generate results that match these observations.[2] A solution that is consistent with the observations may provide us with some physical constraints for the solar wind flow upstream. Indeed, some authors have combined their numerical simulations with available data in order to deduce empirical limits on coronal quantities [*Habbal and Esser*, 1994].

[2]Boundary condition adjustment to match the solar wind observations requires trial and error. But experience obtained from the polar wind parametric studies in Chapter 4 helps shorten this tedious procedure considerably.

	Solar Wind	Polar Wind
Outflow nature	subsonic to supersonic, current free	subsonic to supersonic, current free
Source	coronal holes	ionosphere (*in situ* measurements)
Electrons	core, halo	thermal, photoelectron
Ions	H^+, He^{++}, ...	O^+, H^+, ...
Measure-ments	s/c Helios I, II, Ulysses, SOHO, ...	satellites DE-1,2, Akebono
B Field	open, divergent, monotonically decreases with heliocentric distance (Parker spiral, ...)	open, divergent, monotonically decreases with altitude (near earth $\approx$ dipole)
Microscopic effects	Coulomb collisions, wave-particle interactions	Coulomb collisions, wave-particle interactions

Table 5.1: A summary of the polar/solar wind comparison.

The self-consistent hybrid model, in its classical polar wind application, takes into account the effects of the field-aligned electric field, gravitational force, Coulomb collisions, and mirror force. These are essentially all the principal effects that govern the solar wind, in particular, the low-speed solar wind. (In the high-speed solar wind, wave-particle interactions also play a significant role in the dynamics.) Thus, we choose to extend the model to the low-speed solar wind.

5.2.1 Model Adjustments

This extension requires a few minor changes in the model. Among the four major solar-wind governing effects mentioned earlier, those due to the electric field and Coulomb collisions are self-consistently determined. Gravitational and mirror forces, on the other hand, are based on the imposed background setting. In particular, the mirror force is determined by the imposed magnetic field configuration. In contrast to a dipole magnetic field for the polar wind case, the magnetic field that we use for the solar wind application has the relation $B \propto R^{-2}$, where R is the heliocentric distance. For the heliocentric regions that we will consider, this dependence seems to be a reasonably close fit [*Bird and Edenhofer*, 1990].

The difference in particle composition between the polar and solar winds also requires some adjustments of the model. Besides the different abundance of ion species, where we have to replace the O^+ with He^{++} in the solar wind application, the electron distributions in the source regions of the two outflows may also have different characteristics. In the polar wind, particularly on the dayside, the ionospheric electron distribution is composed of a thermal component and the photoelectron population. Hence, the boundary condition for the polar wind electrons consists of a drifting Maxwellian distribution for the thermal electrons, determined using quasi-neutral and current-free conditions in the fluid calculation, and a separate distribution for the suprathermal photoelectrons as an initial condition for the kinetic calculations. In the source of the solar wind, the coronal holes, there is however no evidence of such a superposed electron distribution. Thus, we assume the total electron distribution in the coronal holes to be a drifting Maxwellian, but argue that downstream of the

solar wind, the electron distribution will evolve into a superposition of a core and a halo, due to the global collisional effects discussed in Section 2.1. To distinguish the electrons that eventually constitute the halo, we use the cutoff scheme introduced in Section 4.1.1, and illustrated in Fig. 4-10. In other words, a certain portion of the tail of the electron drifting Maxwellian distribution at the boundary is assigned to be the suprathermal halo electrons downstream of the solar wind, and its evolution is described by the kinetic component of the model. The rest of the electrons is treated as the core, whose properties are determined by the fluid calculation. To determine where the cutoff should be set in distinguishing between the core and halo electrons, we use the solar wind observations downstream as a guideline. Notice that unlike the polar wind calculation, the boundary ratio of suprathermal to thermal electron densities (n_s/n_e) for the solar wind application cannot be arbitrarily chosen, but is solely determined by the cutoff itself. Therefore the cutoff can be considered one of the boundary conditions, and is adjusted so as to match the solar wind observations.

5.2.2 A Solar Wind Solution

In order to demonstrate the applicability of the self-consistent hybrid model to the solar wind, we have generated a solution that is consistent with the typical particle quantities for the low-speed solar wind at 1 AU. In this calculation, the simulation range is from 4 $R_\odot$, where $R_\odot$ is the solar radius, to 5 AU. (1 AU corresponds to about 215 $R_\odot$.) All initial and boundary conditions are applied at the lower end of the simulation. At the boundary, the distributions for the kinetic component of the model are assumed to be drifting Maxwellians with a drift velocity (u_0) 45 km/s, and temperatures of 50 and 300 eV for the H^+ and He^{++} respectively. Further, we assume that downgoing particles ($v_{||} < 0$) are collisionally absorbed by the higher density plasma at lower heliocentric distances. Thus, only the upgoing particles ($v_{||} > 0$) are used in the simulation. For the electrons, the temperature of the drifting Maxwellian distribution is 200 eV. The cutoff velocity for the halo corresponds to 6.5 times the temperature away from the drift velocity, *i.e.* the halo electrons have velocities $\mathbf{v}$ that satisfy $v_{||} > u_0$ and $m_e(\mathbf{v} - u_0\,\hat{b})^2/2T_e > 6.5$, where $v_{||}$ is the field-aligned component

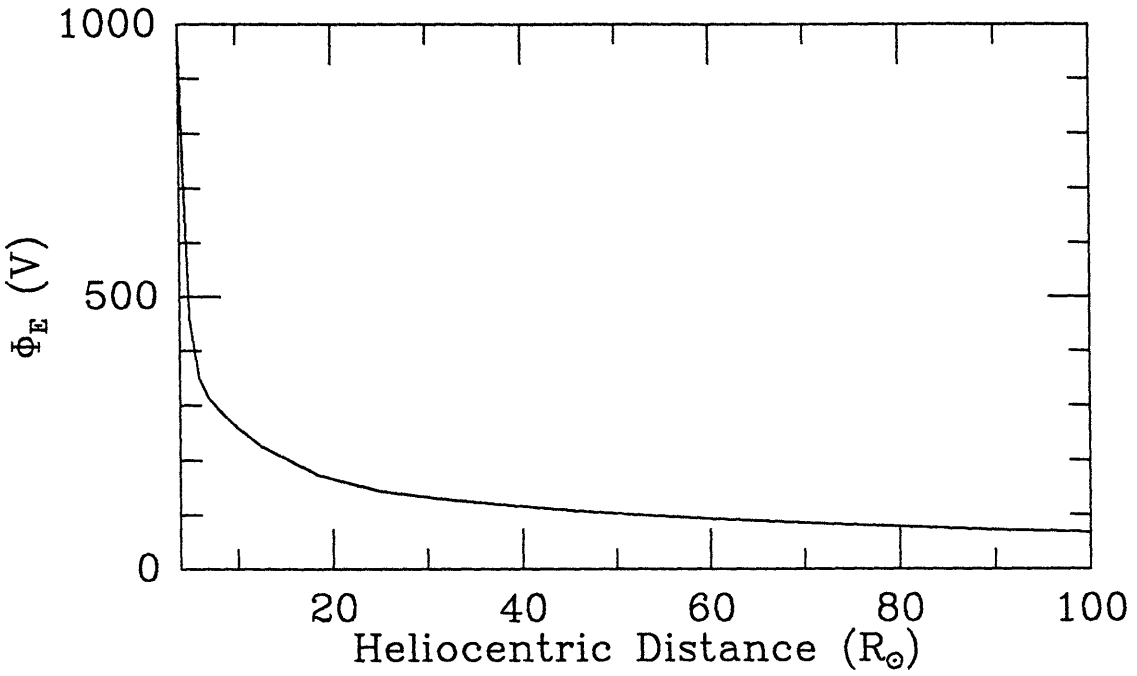

Figure 5-1: Profile of the self-consistent ambipolar electric potential up to 100 $R_\odot$.

of $\mathbf{v}$, $\hat{b}$ is the unit vector along the magnetic field line, m_e is the electron mass, and T_e is the temperature of the electron Maxwellian distribution. This halo distribution is used as the initial condition for the kinetic calculation of the suprathermal electrons, and corresponds to $n_s/n_e = 4.6366 \times 10^{-3}$. The boundary densities for H^+ and He^{++} are 3×10^{11} and 10^{10} m^{-3} respectively.

The self-consistent ambipolar electric potential for the solution drops by about 900 V across the simulation range. As shown in Fig. 5-1, most of this potential drop occurs within 20 $R_\odot$ of the sun. This electric potential profile is consistent with those assumed by *Scudder and Olbert* [1979] and *Olbert* [1982] in their global collisional calculations for solar wind electrons, both in shape and the amount of potential drop.

Figure 5-2 shows the density profiles for the H^+, He^{++}, core and halo electrons (with subscripts h, α, e, and s, respectively). Note that boundary conditions in our calculation are adjusted such that these densities are consistent with their corresponding typical values at 1 AU. The results show that at 1 AU, the H^+ density is about 2×10^7 m^{-3} (or 20 cm^{-3}), with the He^{++} density about 5% of that value, and the halo density also about 5% of the core density. These densities are comparable to the

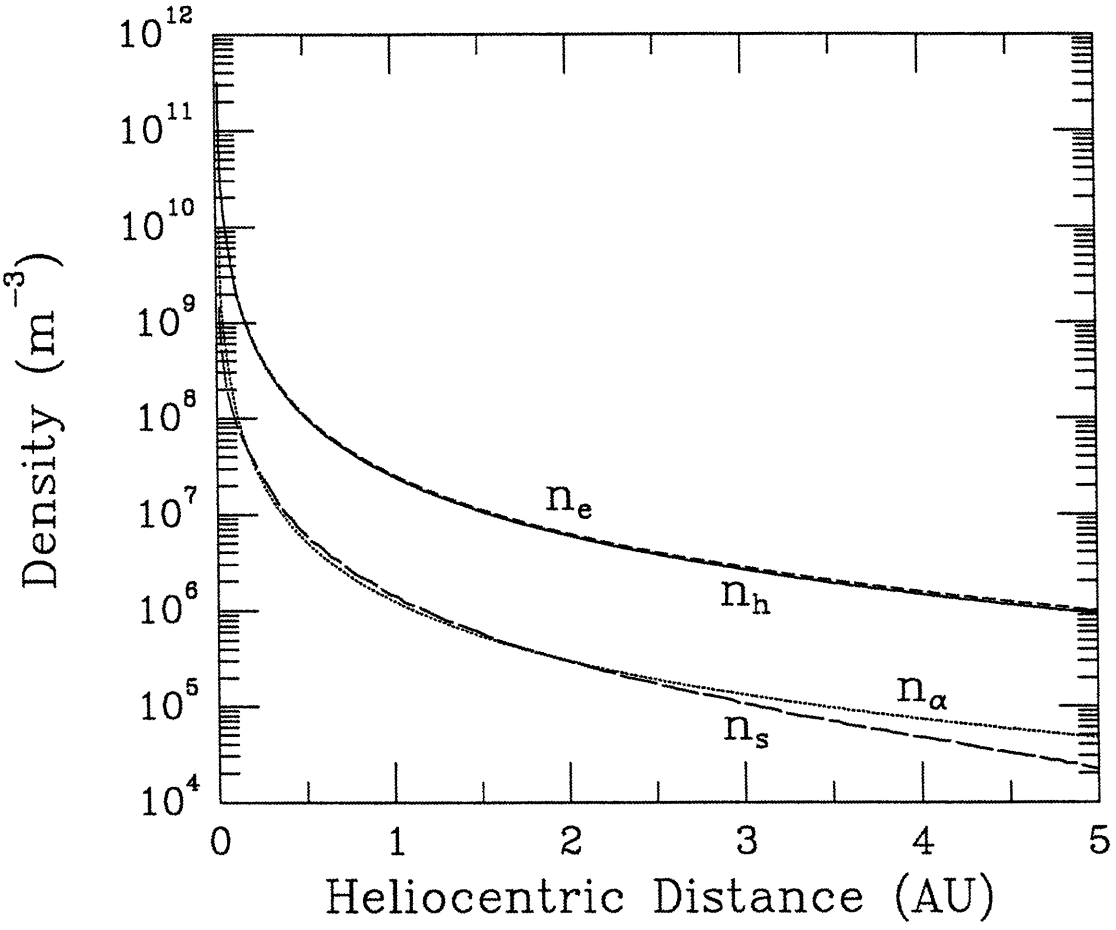

Figure 5-2: Density profiles of the H^+ (n_h), He^{++} (n_α), core (n_e), and halo electrons (n_s).

typical values of the low-speed solar wind at 1 AU [*Schwenn*, 1990], and consistent with the earlier simulations by *Livi and Marsch* [1987].

The H^+, He^{++} and core electron velocities are shown in Fig. 5-3. Notice that the solar wind attains its high velocity only within a few $R_\odot$, mainly due to acceleration by the large potential difference shown in Fig. 5-1. This acceleration mechanism is opposed by the gravitational force. From about 6 to 12 $R_\odot$, the gravitational force on the ions is larger than that due to the electric field, thereby leading to a slight decrease in the ion velocities. At 1 AU, the H^+ velocity is about 275 km/s, which is a somewhat low but still typical value for the low-speed solar wind [*Schwenn*, 1990; *Pilipp et al.*, 1987]. The average He^{++} velocity is about 40 km/s smaller. However, the contour plot of the He^{++} distribution, as shown in Fig. 5-4, indicates that the peak of the distribution is around 270 km/s, much closer to the H^+ velocity. (Note that at low values of the distribution function, the contours are not smooth, reflecting the statistical nature of the kinetic calculation.) The reason for such a discrepancy between the He^{++} average and peak velocities is the shape of its distribution, which exhibits a tail toward the sunward direction. The formation of this tail is due to global collisional effects. Basically, the mechanism leading to this tail formation is similar to that responsible for the anomalous electron fluxes in both the polar and solar winds (see Section 2.1), except that this He^{++} tail is in the opposite direction. Note that the major ion species in the solar wind is H^+, which generally has a higher velocity than the He^{++} ions because of a larger charge-to-mass ratio (in contrast to the polar wind case where the major ion species, O^+, has a smaller charge-to-mass ratio than H^+, the secondary ion species). Thus, the He^{++} ions collide mostly with the H^+. Such collisions tend to increase the velocity of the He^{++} ions (*c.f.* slowing-down of H^+ due to collisions with O^+ in the polar wind). However, as discussed in Section 2.1, this effect is also velocity-dependent: the larger the velocity difference between an He^{++} ion and the H^+ species, the smaller this collisional speeding-up is experienced by the He^{++}ion. Because the He^{++} generally has a smaller velocity than the H^+, the relative velocity between the H^+ and an individual He^{++} increases as the velocity of the He^{++} particle decreases. Thus, the smaller the velocity of an He^{++}, the

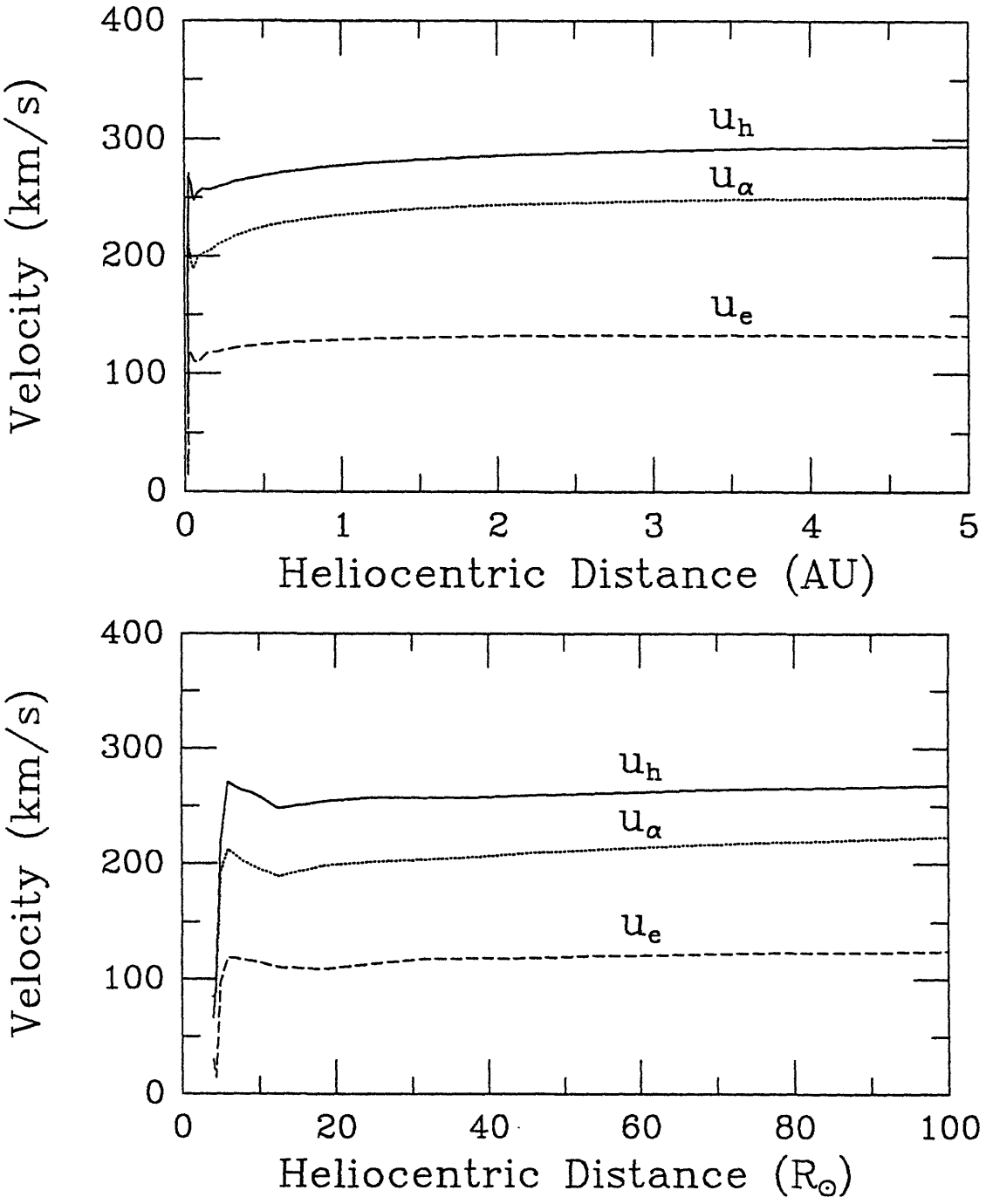

Figure 5-3: Velocity profiles of the H^+, He^{++}, and core electrons. Top panel: full simulation range; bottom panel: up to 100 $R_\odot$.

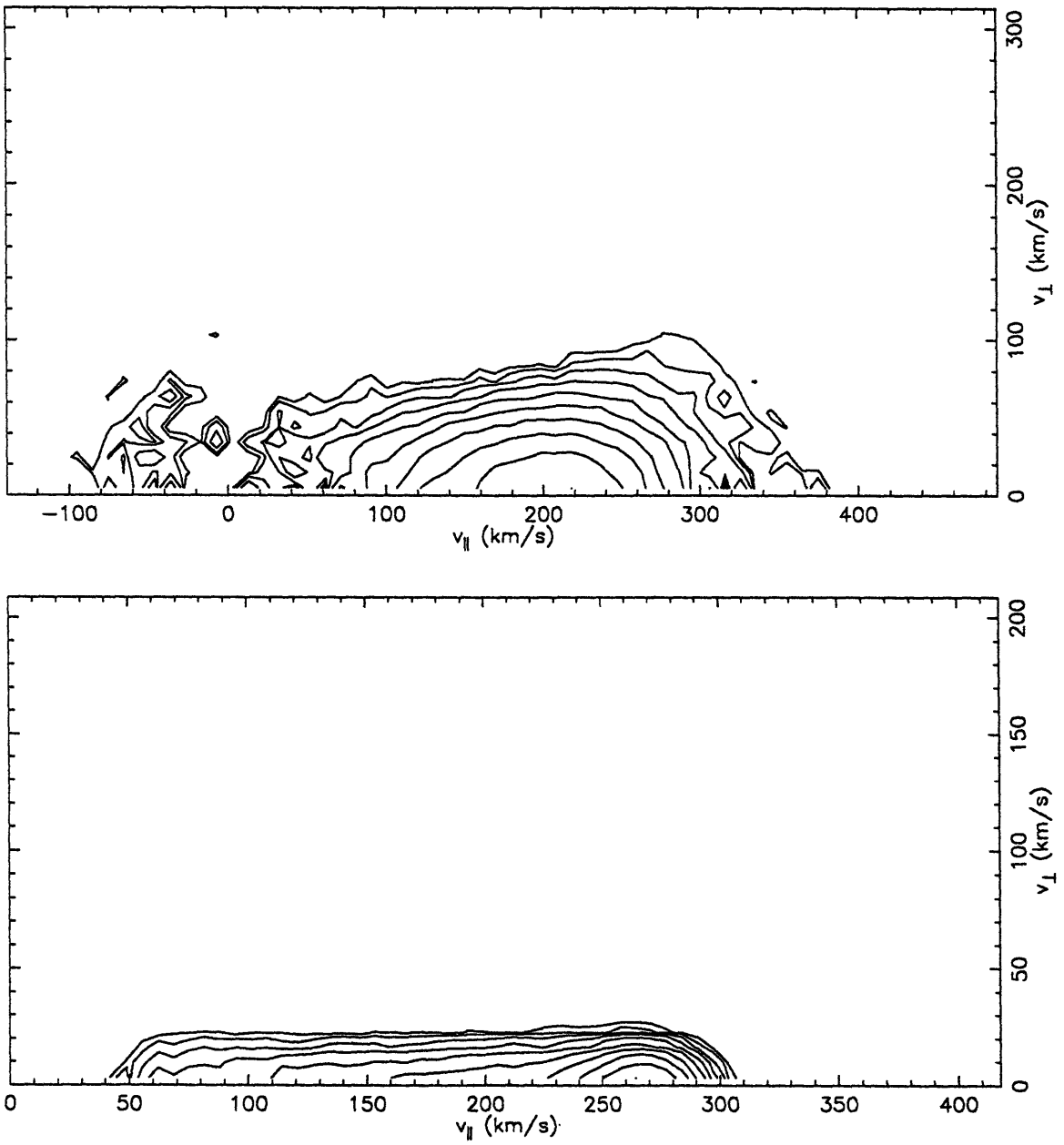

Figure 5-4: Contour plots for the He^{++} distribution at 10 $R_{\odot}$ (upper panel) and 1 AU (lower panel). The lines are in linear scale.

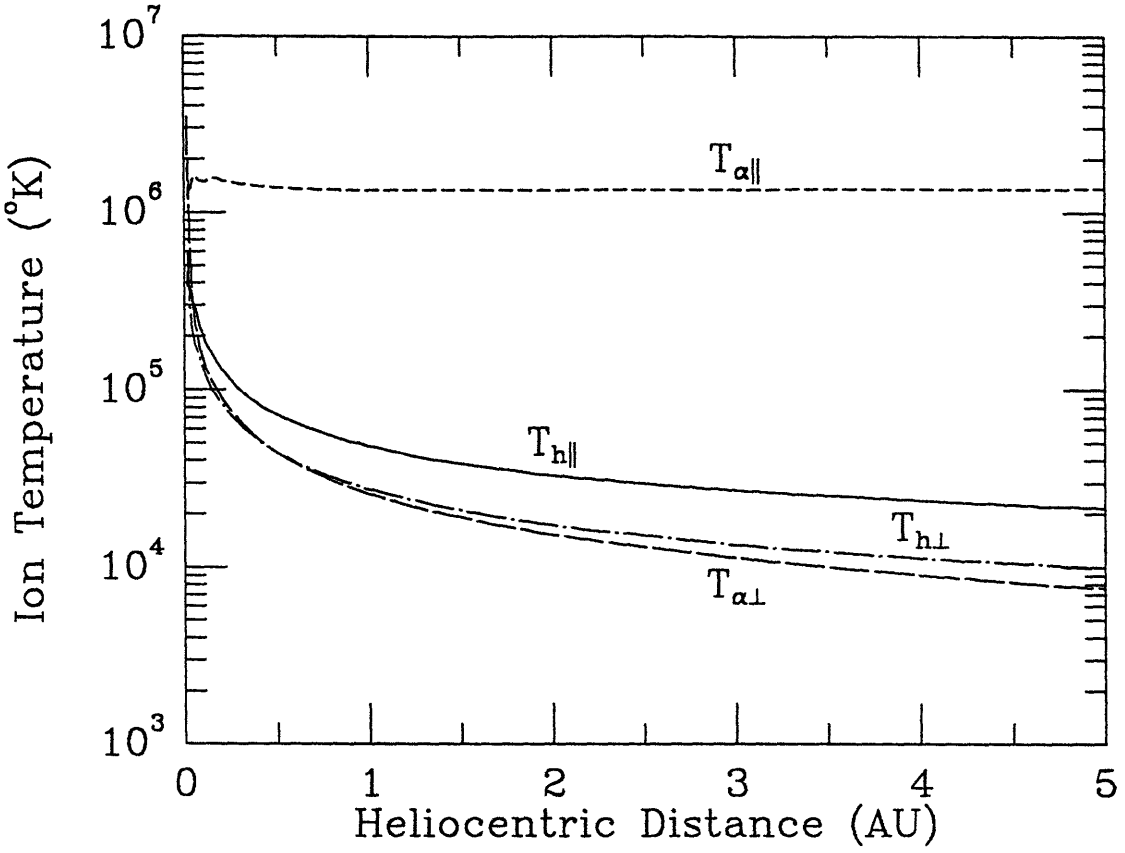

Figure 5-5: Profiles of the ion temperatures.

less collisional speeding-up it experiences. This velocity-dependence of the collisional effect leads to a larger velocity differential among the He^{++} ions, resulting in a tail in the sunward direction as the species travels downstream.

Note that the He^{++} distribution at 1 AU is very anisotropic. This anisotropy is partly due to the mirror force, and partly due to the relatively weak collisions among the He^{++} ions. The mirror force converts the particles' energy transverse to the magnetic field into the parallel direction as they travel outward, leading to the decrease in the He^{++} perpendicular temperature, as shown in Fig. 5-5. Although Coulomb collisions among the species tends to isotropize the distribution, He^{++} , however, does not have a density (and thus collisional rates) high enough for this collisional isotropization to be effective, as its parallel temperature remains rather constant throughout the flow. On the other hand, the H^+ ions, being the dominant ion species, have collisional rates high enough that the isotropization effect has a

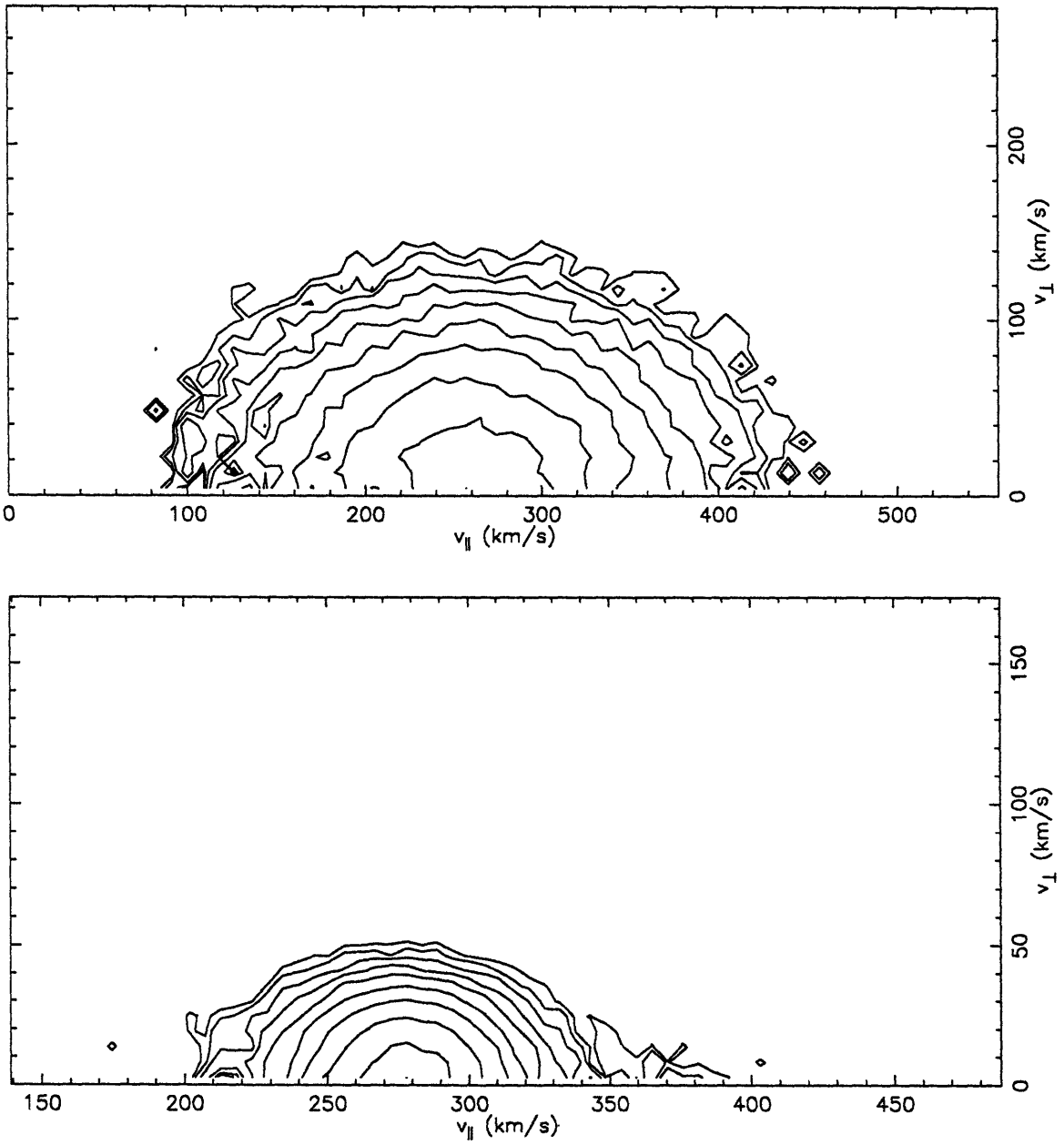

Figure 5-6: Contour plots for the H^+ distribution at 10 $R_\odot$ (upper panel) and 1 AU (lower panel). The lines are in linear scale.

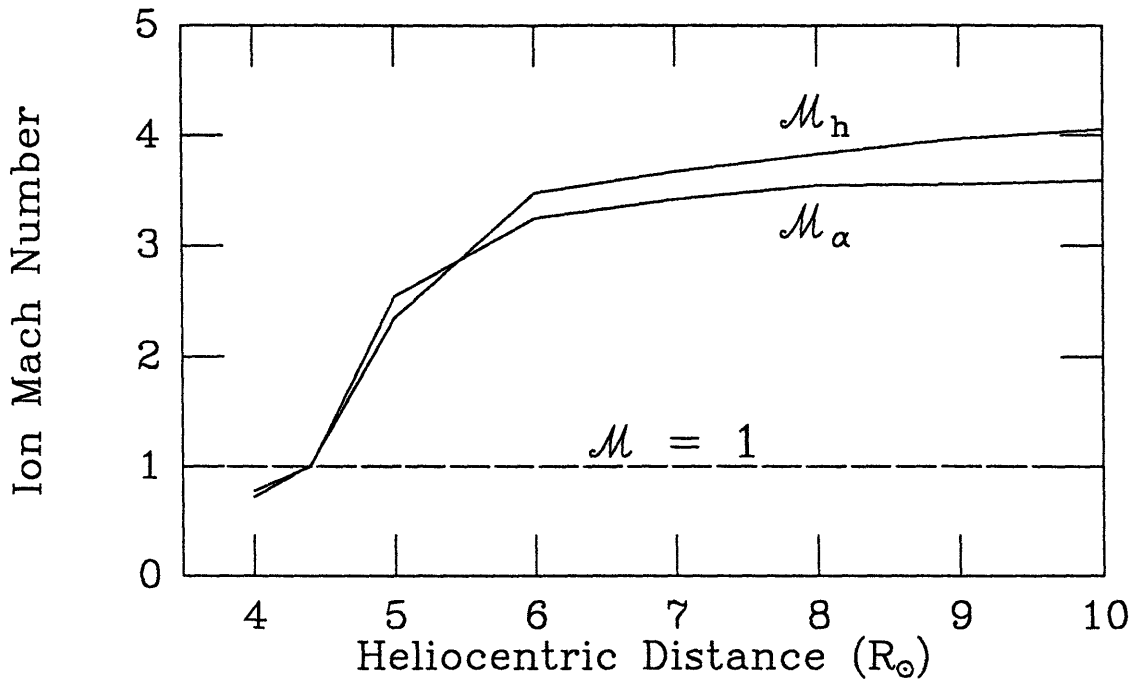

Figure 5-7: Profiles of the ion Mach numbers.

significant impact on its temperatures. The parallel to perpendicular temperature ratio for the H^+ is about 1.7 at 1 AU. Without such collisional effects, we would expect the H^+ anisotropy to be similar to that for the He^{++}. The H^+ distribution at 1 AU is shown in the bottom panel of Fig. 5-6. Notice that the core of the distribution is more isotropic than the temperature ratio indicates. In other words, the slightly anisotropic temperature ratio is largely due to the tail portion of the distribution, where the isotropization effect is relatively small because of the smaller collisional rates for the particles. The distribution is similar to those obtained by *Livi and Marsch* [1987] in their study of the Coulomb collisional effects on the solar wind ions.

The Mach numbers that correspond to the ion velocities and temperatures are shown in Fig. 5-7. Notice that our solution varies continuously from a subsonic regime to a supersonic regime, demonstrating the ability of our model to generate a continuous transonic solar wind solution. It is worth noting that most steady-state studies of the solar wind avoid the difficulties associated with the sonic points by solving the associated time-dependent problem [*Esser and Habbal*, 1995].

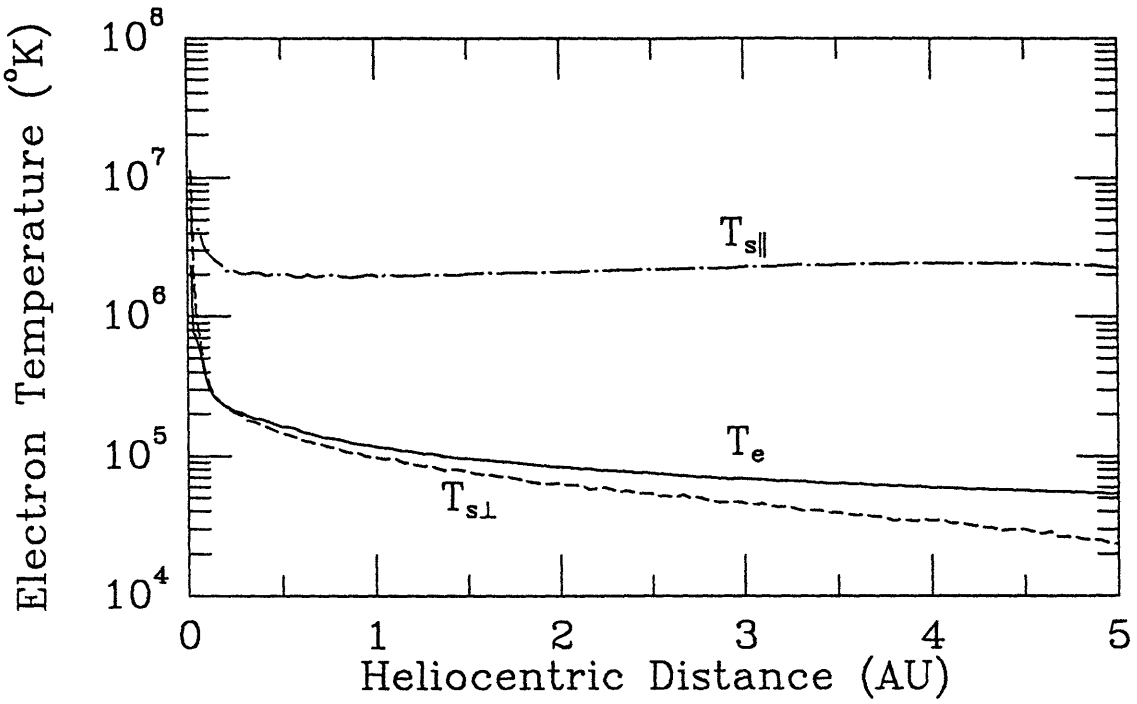

Figure 5-8: Profiles of the core and halo electron temperatures.

The solar wind electron temperatures are shown in Fig. 5-8. The temperature of the core electrons, T_e, is about 10^5 °K at 1 AU, a typical value for the low-speed solar wind [*Schwenn*, 1990]. The halo electron temperature in the field-aligned direction ($T_{s\|}$) is much larger than that of the core throughout our simulation range, consistent with the definition of the two electron components.

Figure 5-9 shows the heat flux carried by the total electron population, *i.e.* the core and the halo, with the core distribution approximated by a drifting Maxwellian in the fluid calculation, and the halo distribution determined from the kinetic calculation. The total heat flux is found to be outwardly directed (positive sign, by convention) for the whole electron distribution, consistent with the solar wind observations [*Pilipp et al.*, 1987] and the results obtained by *Scudder and Olbert* [1979].

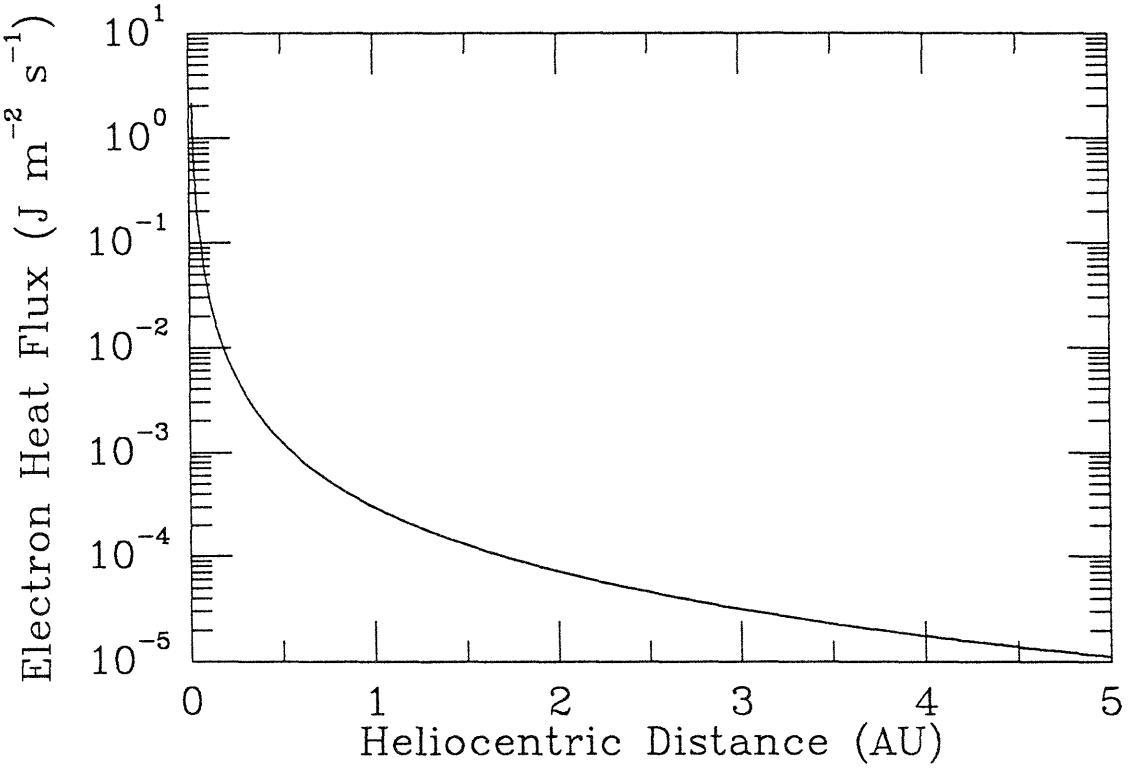

Figure 5-9: Profiles of the total electron heat flux.

5.3 Discussion

We have demonstrated the versatility of the self-consistent hybrid model with a study of the low-speed solar wind. A token of this versatility is the minimal amount of modification required to adopt the code to this new situation. The solution generated from the model reflects the importance of kinetic effects affecting the solar wind flow. In particular, Coulomb collisions play a significant role in the dynamics of all the particle species we consider. The most dramatic result that collisions has introduced is the isotropization of the H^+ distribution, which would have looked like the highly anisotropic He^{++} distribution, had collisions been absent.

We have discussed the speeding-up effect of the He^{++}-H^+ collisions on the He^{++} ions. By the same token, these collisions have a slowing-down effect on the H^+due to conservation of momentum. However, because of the density dominance by the H^+ ions, they have a larger mass density than the He^{++}. As a result, their velocity change due to this collisional effect is considerably smaller than that for the He^{++}. Nevertheless, this is also one of the factors that contribute to the rather small velocity difference between the two ion species in our solution.

Of course, the solution that we have shown is designed to correspond to typical low-speed solar wind conditions. In the high-speed solar wind, however, wave-particle interactions are believed to play an important role in the dynamics of the outflow. Our model, in its present form, has not taken into account the impact of waves on the particles. However, wave-particle interactions can be represented by a quasi-linear collisional operator that formally looks like the Fokker-Planck operator for Coulomb collisions, on which the model is based. Therefore, it is feasible to extend the model to the high-speed solar wind by incorporating the effects of wave-particle interactions on the collisional rates determined in the kinetic part of our calculation. This is a possible extension of the model that we will consider in the near future. It is worth noting here that the Monte-Carlo method that we have applied to Coulomb collision was initially developed precisely to take wave-particle interaction into account [*Retterer et al.*, 1983].

Chapter 6

Conclusion

The work in this thesis is ultimately motivated by the increasing experimental evidence that photoelectrons may affect the dynamics of the polar wind. For example, field-aligned electron distributions in the photoelectron energy range with appreciable outwardly directed heat flux have been observed in the high-altitude polar regions by the DE-1 satellite. Similar electron fluxes have also been observed in the low-altitude polar wind by the DE-2 satellite, along with incoming electron fluxes, which have been suggested to arise from reflection by the electric field above the altitude of the satellite ($\geq$ 500 km). By comparing the outgoing and incoming fluxes, *Winningham and Gurgiolo* [1982] estimated the electric potential difference to range from a few to tens of eV, depending on the solar zenith angle. The solar zenith angle is related to the photoionization rate, which itself is related to the local ionospheric photoelectron density. These observations thus imply a relationship between the local photoelectron density below the satellite and the electric potential drop above it.

In principle, the polar wind electric potential drop should also influence the ion dynamics. Indeed, the more recently observed day-night asymmetries in H^+ and O^+ outflow velocities [*Abe et al.*, 1993b] have provided us with indications of the impact of the electric field on the ions. Because the electric field can accelerate the polar wind ions, these asymmetries in ion outflow velocities between day and night (which clearly have different solar zenith angles) suggest that photoelectrons may affect the polar wind dynamics through their effect on the electric field.

To study the relation between photoelectrons and the electric field, one must first be able to explain the formation of the field-aligned anomalous electron fluxes associated with photoelectrons. ("Anomalous" is used in the sense that these fluxes cannot be explained by the concept of thermal conductivity and temperature gradient.) Such anomalous fluxes, in fact, can be explained by a mechanism relying on the earth's divergent magnetic field and the energy dependence of the Coulomb collisional cross-sections. The description of this mechanism requires a global kinetic approach. ("Global kinetic" refers to resolving the mesoscale evolution of the particle distribution function by taking into account the microscale interactions.)

We have used a global kinetic collisional test-particle approach based on this mechanism in our preliminary investigation of the relation among the polar wind photoelectrons, their heat flux, and the electric field. Results of the calculation indicate that photoelectrons not only may give rise to the observed suprathermal heat fluxes, but also dominate the thermal electrons in the total heat flux contribution. Our preliminary results also show that presence of the photoelectrons may enhance the electric field. Although these results have shown a relationship among the photoelectrons, the anomalous electron heat fluxes, and the electric field that is consistent with polar wind observations, a self-consistent approach that also describes the global kinetic collisional photoelectron physics is required for studying the overall impact of photoelectrons on the polar wind dynamics.

In this thesis, we have introduced a self-consistent hybrid model that provides a global kinetic collisional description for the polar wind photoelectrons. The model is hybrid in that it consists of a fluid part for the thermal electrons and a kinetic collisional part, and should be distinguished from other hybrid schemes where, for example, the electrons are treated as a massless neutralizing fluid. Specifically, in this model, photoelectrons (which are treated as test particles because of their low relative density), and all the ion species (H^+, O^+) are described by a global kinetic collisional approach, while thermal electron properties and the ambipolar electric field are determined by a fluid calculation. The model is based on an iterative scheme: A physically meaningful solution is obtained when it converges. This model signi-

fies the ground-breaking nature of this work in polar wind theory, primarily for two reasons. One, it is the first to incorporate successfully the global kinetic collisional photoelectron description into a self-consistent polar wind picture. Two, because of its kinetic treatment of the ions, it provides the first global steady-state polar wind calculation that generates a continuous solution which varies from a low-altitude collisional subsonic regime to a high-altitude collisionless supersonic regime. Results from the calculations represent an important step toward polar wind theory-observation closure as they are quantitatively consistent with experimental data in a variety of aspects. For example, the calculated potential drop is consistent with the experimentally deduced value. The resulting ion properties such as densities, outflow velocities and temperatures are also within experimental limits. Anisotropy between upwardly and downwardly going electrons, and an upwardly directed electron heat flux, both observed in the polar wind, also appear in our simulations.

The self-consistent model is also used to examine the impact of photoelectrons on the polar wind dynamics. Specifically, we perform a comparative study by varying the relative photoelectron density at the lower boundary (the ionosphere). Results of the study reveal the importance of kinetic effects and the intrinsic complexity of the polar wind dynamics. These results also demonstrate that a self-consistent description is indeed required for the comparative study. This is particularly true because some polar wind outflow properties are governed by *competing* effects, which are affected by these outflow properties themselves to different extents; only a self-consistent description can take all these inter-relations into account. Despite all these complex inter-relations, we find that an increase in the relative photoelectron density enhances the self-consistent ambipolar electric field in the polar wind. In fact, our results have shown that these two quantities, together with the electron temperature, are all related. A higher relative photoelectron density at the boundary corresponds to a larger intrinsic electron heat flux. That leads to a larger ambipolar electric field. A larger portion of photoelectrons also means that the thermal electrons are more effectively heated through the collisions between the two electron components, because a greater heat source is available for each thermal electron on average. Thus,

that leads to a higher thermal electron temperature, and a higher overall electron temperature. A higher temperature would lead to a larger pressure gradient. To balance that, a larger electric field is required.

The electric field enhancement associated with an increase in the relative photoelectron density often dictates the variation of other polar wind quantities, *e.g.*, enhancement of the escaping ion flux, increase in the ion outflow velocities. This electric field enhancement that arises from an increase in the relative photoelectron density, however, leads to a more complicated variation in the ion densities. Intuitively, one would expect the ion density at high altitudes to increase with the electric field, because the field pushes more ions to escape. In fact, this is not the only effect of the electric field on the ion densities. Acceleration of the *escaping* ions will deplete the density of the species due to particle conservation. Thus, the electric field itself, through its acceleration of the ions, can create competing effects on the ion densities. We find that in general, when the relative photoelectron density is sufficiently low, (and hence the electric field is also sufficiently low), an increase in this quantity, which causes the electric field also to increase, leads to an increase in the ion densities. But this variation holds only up to a certain limit. Beyond that, an increase in the relative photoelectron density (which still causes the electric field to increase) causes the density to respond in an opposite way as the depletion effect takes over.

Coulomb collisions also play an important role in the polar wind dynamics. For example, the H^+-O^+ collisions give rise to a slowing-down effect on the H^+ ions. This collisional effect competes against the acceleration by the electric field in governing the H^+ outflow velocity. The relative importance of this slowing-down effect is related to the O^+ density, due to the density dependence of the collisional rates. When the relative photoelectron density is sufficiently low such that an increase in the quantity will cause the ion densities to increase (see above), the slowing-down effect on H^+ may be enhanced to a greater extent than the acceleration effect due to the electric field.

We also investigate the effects of other ionospheric quantities, such as the O^+ temperature and density, and the H^+ temperature, on the polar wind dynamics through

a series of comparative studies. Our results indicate that these ionospheric quantities influence the polar wind mainly through their impact on the self-consistent electric field, which responds primarily to the ambipolar effect, whereby a larger electron flux (such as that associated with a larger portion of photoelectrons) leads to a larger self-consistent electric field. A smaller ion flux in the ionospheric conditions seems also to give rise to a larger self-consistent electric field. We have shown from our comparative studies that in general, the impact of the electric field on various polar wind outflow properties is very apparent.

Although the self-consistent hybrid model, which has been used in all these comparative studies, was developed for the classical polar wind, its treatment of kinetic physics is modular and quite general. Thus, if necessary, the model can be readily extended to include other kinetic effects in the polar wind, such as wave-particle interactions. In fact, the model is so versatile that it can be applied to other steady-state plasma outflows. We have illustrated its versatility with a study of the low-speed solar wind. This study has shown that similar mechanisms are operative in the solar wind.

To conclude, we have developed a self-consistent model that includes anisotropic kinetic effects of anomalous transport, such as those observed in the polar wind and due to photoelectrons. The self-consistency of the model lands additional credibility to our results in that they no longer rely on arbitrary choices of the electric field. Furthermore, self-consistency is required in order to investigate the complex interrelationship among the various physical mechanisms included in the model.

Appendix

Sixteen-Moment Equations

A.1 The Sixteen Moments and Approximation of the Distribution Function

The "generalized transport" approach describes a given particle species by a number of its macroscopic (velocity-averaged) physical quantities. Each of these physical quantities is related to a velocity moment. In the 16-moment model, these physical quantities are:

density (0th-order moment, 1 scalar value)

$$n = \int d\mathbf{v}\, f, \tag{A.1}$$

average drift velocity (1st-order moment, 3 scalar values)

$$\mathbf{u} = < \mathbf{v} >, \tag{A.2}$$

pressure tensor (2nd-order moment, 6 distinct scalar values)

$$\mathbf{P} = nm < \mathbf{cc} >, \tag{A.3}$$

and heat flux vectors for parallel and perpendicular energies per unit density (3rd-order moment, 3 scalar values each)

$$\mathbf{q}_{\|} = m < c_{\|}{}^2 \mathbf{c} >, \tag{A.4}$$

$$\mathbf{q}_{\perp} = \frac{1}{2} m < c_{\perp}{}^2 \mathbf{c} >, \tag{A.5}$$

where m is the mass of the species, $< >$ denote the average of the quantity inside the brackets, *i.e.*

$$< \mathbf{A} > = \frac{1}{n} \int d\mathbf{v} \, f \, \mathbf{A}, \tag{A.6}$$

f is the distribution function, and $\mathbf{c} \equiv \mathbf{v} - \mathbf{u}$. Each of these physical quantities is treated as a parameter in the model. Note that other physical quantities up to the third order of velocity moments can be expressed by combinations of these sixteen parameters. For example, the parallel and perpendicular temperatures, and the stress tensor are related to the pressure tensor by, respectively,

$$T_{\|} = \frac{1}{n} \mathbf{P} : \mathbf{e_3 e_3}, \tag{A.7}$$

$$T_{\perp} = \frac{1}{2n} \mathbf{P} : (\mathbf{e_1 e_1} + \mathbf{e_2 e_2}), \tag{A.8}$$

$$\tau = \mathbf{P} - nT_{\perp} \mathbf{I} - n(T_{\|} - T_{\perp}) \mathbf{e_3 e_3}, \tag{A.9}$$

where $\mathbf{I}$ is the unit dyadic, and $(\mathbf{e_1}, \mathbf{e_2}, \mathbf{e_3})$ is a set of orthogonal unit vectors with $\mathbf{e_3}$ in the direction parallel to the magnetic field.

The system of 16-moment equations uses assumption (1.7) for the distribution function, where the expression for Ψ consists of the independent variable $\mathbf{v}$, as well as parameters that represent various physical quantities. Specifically,

$$\begin{aligned} \Psi \;=\; & \frac{\beta_{\perp}}{2nm} \left[\beta_{\perp} (c_1{}^2 - c_2{}^2)(\tau : \mathbf{e_1 e_1}) + 2\beta_{\perp} (\tau : \mathbf{e_1 e_2}) c_1 c_2 + 2\beta_{\|} (\tau : \mathbf{c}_{\perp} \mathbf{c}_{\|}) \right] \\ & - \frac{\beta_{\perp}{}^2}{m} \left(1 - \frac{\beta_{\perp} c_{\perp}{}^2}{4} \right) \mathbf{q}_{\perp} \cdot \mathbf{c}_{\perp} - \frac{\beta_{\perp} \beta_{\|}}{m} \left(1 - \frac{\beta_{\perp} c_{\perp}{}^2}{2} \right) \mathbf{q}_{\perp} \cdot \mathbf{c}_{\|} \end{aligned}$$

$$-\frac{{\beta_{\|}}^2}{2m}\left(1-\frac{\beta_{\|}{c_{\|}}^2}{3}\right)\mathbf{q}_{\|}\cdot\mathbf{c}_{\|}-\frac{\beta_{\perp}\beta_{\|}}{2m}\left(1-\beta_{\|}{c_{\|}}^2\right)\mathbf{q}_{\|}\cdot\mathbf{c}_{\perp}\ , \tag{A.10}$$

where $\beta_{\|} = m/T_{\|}$ and $\beta_{\perp} = m/T_{\perp}$ [*Barakat and Schunk*, 1982]. Note that the parametric dependence of the distribution function defined in Eq. (1.7), (1.8) and (A.10) is consistent with the definitions of the physical quantities (Eq. (A.1 – A.5) and (A.7 – A.9)). In the polar wind application, due to the gyrotropic nature of the transport, the set of 16-moment equations reduces to six different parameters, whose transport properties are described by Eq. (1.17 – 1.22).

A.2 Collisional Terms

Moment-based expressions for the collisional terms in Eq. (1.17 – 1.22) were derived by *Burgers* [1969] for various microscopic interactions. In the case of Coulomb collisions, these terms (used by *Ganguli et al.* [1987]) are as follows, where the subscript a labels the species under consideration and the running subscript b labels the background particle species:

$$\frac{\delta u_a}{\delta t} = \sum_b \nu_{ab}\,(u_b - u_a)\,(1+\gamma_{ab})\ , \tag{A.11}$$

$$\begin{aligned}\frac{\delta T_{a\|}}{\delta t} &= \sum_b \frac{m_a\nu_{ab}}{(m_a+m_b)}\left\{\frac{6}{5}T_{b\|}-\left[2+\frac{4\,m_b}{5\,m_a}\right]T_{a\|}\right.\\ &\left.+\frac{4}{5}T_{b\perp}+\frac{4\,m_b}{5\,m_a}T_{a\perp}+\left[2\,T_b+\left(4+6\frac{m_b}{m_a}\right)T_a\right]\gamma_{ab}\right\}\ ,\end{aligned} \tag{A.12}$$

$$\frac{\delta T_{a\perp}}{\delta t} = \sum_b \frac{m_a\nu_{ab}}{(m_a+m_b)}\left[3\,(T_b-T_a)+m_b\,(u_b-u_a)^2(1+\gamma_{ab})\right]-\frac{1}{2}\frac{\delta T_{a\|}}{\delta t}\ , \tag{A.13}$$

$$\frac{\delta q_{a\|}}{\delta t} = -\nu_{ab}\,q_{a\|}\ , \tag{A.14}$$

$$\frac{\delta q_{a\perp}}{\delta t} = -\nu_{ab}\,q_{a\perp}\ , \tag{A.15}$$

where

$$\nu_{ab} = \frac{n_b\,(32\pi)^{1/2}{e_a}^2{e_b}^2\,(m_a+m_b)\,(\ln A)\,\exp(-{\chi_{ab}}^2)}{3\,{m_a}^2\,m_b\,{\alpha_{ab}}^3}\ , \tag{A.16}$$

is the Coulomb collisional frequency, $\ln A$ is the Coulomb logarithm, e_a and e_b are the algebraic electric charge for species a and b respective, and

$$T_j = \frac{1}{3} T_{j\|} + \frac{2}{3} T_{j\perp} \ , \quad j = a, b \ , \tag{A.17}$$

$$\alpha_{ab}{}^2 = \frac{2T_a}{m_a} + \frac{2T_b}{m_b} \ , \tag{A.18}$$

$$\chi_{ab}{}^2 = \frac{(u_b - u_a)^2}{\alpha_{ab}{}^2} \ , \tag{A.19}$$

$$\gamma_{ab} = \frac{2}{5} \chi_{ab}{}^2 + \frac{4}{35} \chi_{ab}{}^4 + \frac{8}{315} \chi_{ab}{}^6 \ . \tag{A.20}$$

Bibliography

Abe, T., B. A. Whalen, A. W. Yau, S. Watanabe, E. Sagawa, and K. I. Oyama, Altitude profile of the polar wind velocity and its relationship to ionospheric conditions, *Geophys. Res. Lett.*, **20**, 2825, 1993a.

Abe, T., B. A. Whalen, A. W. Yau, R. E. Horita, S. Watanabe, and E. Sagawa, EXOS D (Akebono) suprathermal mass spectrometer observations of the polar wind, *J. Geophys. Res.*, **98**, 11191, 1993b.

Abe, T., B. A. Whalen, A. W. Yau, E. Sagawa, and S. Watanabe, Akebono observations of thermal ion outflow and electron temperature in the polar wind region. to appear in *Physics of Space Plasma (1995), SPI Conf. Proc. and Reprint Series, No. 14*, T. Chang, ed., Scientific Publishers, Cambridge, MA, 1996.

Axford, W. I., The polar wind and the terrestrial helium budget, *J. Geophys. Res.*, **73**, 6855, 1968.

Banks, P. M., and T. E. Holzer, The polar wind, *J. Geophys. Res.*, **73**, 6846, 1968.

Barakat, A. R., and R. W. Schunk, Transport equations for multicomponent anisotropic space plasmas: a review, *Plasma Phys.*, **24**, 389, 1982.

Barakat, A. R., and R. W. Schunk, O^+ ions in the polar wind, *J. Geophys. Res.*, **88**, 7887, 1983.

Barakat, A. R., and R. W. Schunk, Effect of hot electrons on the polar wind, *J. Geophys. Res.*, **89**, 9771, 1984.

Bird, M. K., and P. Edenhofer, Remote sensing observations of the solar corona, in *Physics of the Inner Heliosphere: 1. Large-Scale Phenomena*, edited by

R. Schwenn, and E. Marsch, no. 20 in Physics and Chemistry in Space, chap. 2, p. 47. Springer-Verlag, Berlin Heidelberg, 1990.

Blelly, P. L., and R. W. Schunk, A comparative study of the time-dependent standard 8-, 13- and 16-moment transport formulations of the polar wind, *Ann. Geophys.*, **11**, 443, 1993.

Bondeson, A., and R. Iacono, Ideal stability of cylindrical plasma in the presence of mass flow, *Phy. Fluids B*, **1**, 1431, 1989.

Book, D. L., Plasma physics, in *A Physicist's Desk Reference*, edited by H. L. Anderson, chap. 18, p. 282. American Institute of Physics, New York, second edn., 1989.

Burgers, J. M., *Flow Equations for Composite Gases.* Academic Press, New York, 1969.

Chandler, M. O., Observations of downward moving O^+ in the polar topside ionosphere, *J. Geophys. Res.*, **100**, 5795, 1995.

Cladis, J. B., Parallel acceleration and transport of ions from polar ionosphere to plasma sheet, *Geophys. Res. Lett.*, **13**, 893, 1986.

Demars, H. G., and R. W. Schunk, Transport equations for multispecies plasmas based on individual bi-Maxwellian distributions, *J. Phys. D: Appl. Phys.*, **12**, 1051, 1979.

Demars, H. G., and R. W. Schunk, Solutions to bi-Maxwellian transport equations for the polar wind, *Planet. Space Sci.*, **37**, 85, 1989.

Esser, R., and S. R. Habbal, Coronal heating and plasma parameters at 1 AU, *Geophys. Res. Lett.*, **22**, 2661, 1995.

Ganguli, S. B., The polar wind, submitted to *Rev. Geophys.*, 1996.

Ganguli, S. B., J. H. G. Mitchell, and P. J. Palmadesso, Behavior of ionized plasma in the high latitude topside ionosphere: the polar wind, *Planet. Space Sci.*, **35**, 703, 1987.

Grad, H., On the kinetic theory of rarefied gases, *Comm. Pure and App. Math.*, **2**, 331, 1949.

Habbal, S. R., and R. Esser, On the derivation of empirical limits on the helium abundance in coronal holes below 1.5 $R_\odot$, *Astrophys. J.*, **421**, L59, 1994.

Ho, C. W., J. L. Horwitz, N. Singh, G. R. Wilson, and T. E. Moore, Effects of magnetospheric electrons on polar plasma outflow: a semikinetic model, *J. Geophys. Res.*, **97**, 8425, 1992.

Holzer, T. E., J. A. Fedder, and P. M. Banks, A comparison of kinetic and hydrodynamic models of an expanding ion-exosphere, *J. Geophys. Res.*, **76**, 2453, 1971.

Horwitz, J. L., C. W. Ho, H. D. Scarbro, G. R. Wilson, and T. E. Moore, Centrifugal acceleration of the polar wind, *J. Geophys. Res.*, **99**, 15051, 1994.

Ichimaru, S., *Plasma Physics: An Introduction to Statistical Physics of Charged Particles*, p. 15. Benjamin/Cummings, Menlo Park, CA, 1986.

Jasperse, J. R., The photoelectron distribution function in the terrestrial ionosphere, in *Physics of Space Plasmas*, edited by T. S. Chang, B. Coppi, and J. R. Jasperse, no. 4 in SPI Conference Proceedings and Reprint Series, p. 53, Cambridge, MA. Scientific Publishers, Inc., 1981.

Johnson, J. R., T. Chang, and G. B. Crew, A study of mode conversion in an oxygen-hydrogen plasma, *Phys. Plasmas*, **2**, 1274, 1995.

Johnstone, A. D., and J. D. Winningham, Satellite observations of suprathermal electron bursts, *J. Geophys. Res.*, **87**, 2321, 1982.

Khazanov, G. V., M. W. Liemohn, T. I. Gombosi, and A. F. Nagy, Non-steady-state transport of superthermal electrons in the plasmasphere, *Geophys. Res. Lett.*, **20**, 2821, 1993.

Lee, J. S., J. P. Doering, T. A. Potemra, and L. H. Brace, Measurements of the ambient photoelectron spectrum from Atmosphere Explorer: II. AE-E measurements from 300 to 1000 km during solar minimum conditions, *Planet. Space Sci.*,

28, 973, 1980.

Lemaire, J., Effect of escaping photoelectrons in a polar exospheric model, *Space Res.*, **12**, 1413, 1972.

Livi, S., and E. Marsch, Generation of solar wind proton tails and double beams by Coulomb collisions, *J. Geophys. Res.*, **92**, 7255, 1987.

Nicholson, D. R., *Introduction to Plasma Theory.* Wiley, New York, 1983.

Olbert, S., Role of thermal conduction in the acceleration of the solar wind, *NASA Conf. Publ.*, p. 149, 1982.

Parker, E. N., Dynamics of the interplanetary gas and magnetic fields, *Astrophys. J.*, **128**, 664, 1958.

Pilipp, W. G., H. Miggenrieder, M. D. Montgomery, K.-H. Mühlhäuser, H. Rosenbauer, and R. Schwenn, Characteristics of electron velocity distribution functions in the solar wind derived from the Helios plasma experiment, *J. Geophys. Res.*, **92**, 1075, 1987.

Raitt, W. J., R. W. Schunk, and P. M. Banks, A comparison of the temperature and density structure in high and low speed thermal proton flows, *Planet. Space Sci.*, **23**, 1103, 1975.

Raitt, W. J., R. W. Schunk, and P. M. Banks, The influence of convection electric fields on thermal proton outflow from the inosphere, *Planet. Space Sci.*, **25**, 291, 1977.

Retterer, J. M., T. Chang, and J. R. Jasperse, Ion acceleration in the suprauroral region: a Monte Carlo model, *Geophys. Res. Lett.*, **10**, 583, 1983.

Retterer, J. M., T. Chang, G. B. Crew, J. R. Jasperse, and J. D. Winningham, Monte Carlo modeling of ionospheric oxygen acceleration by cyclotron resonance with broad-band electromagnetic turbulence, *Phys. Rev. Lett.*, **59**, 148, 1987.

Schunk, R. W., Mathematical structure of transport equations for multispecies flows, *Res. Geophys. Space Phys.*, **15**, 429, 1977.

Schunk, R. W., and D. S. Watkins, Comparison of solutions to the thirteen-moment and standard transport equations for low speed thermal proton flows, *Planet. Space Sci.*, **27**, 433, 1979.

Schunk, R. W., and D. S. Watkins, Electron temperature anisotropy in the polar wind, *J. Geophys. Res.*, **86**, 91, 1981.

Schunk, R. W., and D. S. Watkins, Proton temperature anisotropy in the polar wind, *J. Geophys. Res.*, **87**, 171, 1982.

Schwenn, R., Large-scale struture of the interplanetary medium, in *Physics of the Inner Heliosphere: 1. Large-Scale Phenomena*, edited by R. Schwenn, and E. Marsch, no. 20 in Physics and Chemistry in Space, chap. 3, p. 145. Springer-Verlag, Berlin Heidelberg, 1990.

Scudder, J. D., and S. Olbert, A theory of local and global processes which affect solar wind electrons: 1. the origin of typical 1 AU velocity distribution functions — steady state theory, *J. Geophys. Res.*, **84**, 2755, 1979.

Spitzer, Jr., L., *Dynamical Evolution of Globular Clusters*, p. 77. Princeton University Press, Princeton, N.J., 1987.

Tam, S. W. Y., F. Yasseen, T. Chang, S. B. Ganguli, and J. M. Retterer, Anisotropic kinetic effects of photoelectrons on polar wind transport, in *Cross-Scale Coupling in Space Plasmas*, edited by J. Horwitz, N. Singh, and J. Burch, no. 93 in Geophysical Monograph, pp. 133–139. 1995a.

Tam, S. W. Y., F. Yasseen, T. Chang, and S. B. Ganguli, Self-consistent kinetic photoelectron effects on the polar wind, *Geophys. Res. Lett.*, **22**, 2107, 1995b.

Wilson, G. R., C. W. Ho, J. L. Horwitz, N. Singh, and T. E. Moore, A new kinetic model for time-dependent polar plasma outflow: initial results, *Geophys. Res. Lett.*, **17**, 263, 1990.

Winningham, J. D., and C. Gurgiolo, DE-2 photoelectron measurements consistent with a large scale parallel electric field over the polar cap, *Geophys. Res. Lett.*, **9**, 977, 1982.

Winningham, J. D., and W. J. Heikkila, Polar cap auroral electron fluxes observed with ISIS 1, *J. Geophys. Res.*, **79**, 949, 1974.

Yasseen, F., and J. M. Retterer, Critical points in the 16-moment approximation, *J. Geophys. Res.*, **96**, 1827, 1991.

Yasseen, F., J. M. Retterer, T. Chang, and J. D. Winningham, Monte-Carlo modeling of polar wind photoelectron distributions with anomalous heat flux, *Geophys. Res. Lett.*, **16**, 1023, 1989.

Yau, A. W., B. A. Whalen, T. Abe, T. Mukai, K. I. Oyama, and T. Chang, Akebono observations of electron temperature anisotropy in the polar wind, *J. Geophys. Res.*, **100**, 17451, 1995.